EXAMINATION OF PHOTOPHYSICAL CHARACTERISTICS OF PERYLENE DIIMIDE CHROMOPHORES AND THEIR POTENTIAL APPLICATION IN ELECTRO-OPTICAL TECHNOLOGIES

Adrian J. Riives

Submitted in Partial Fulfillment of the Requirements
for the Degree of

DOCTOR OF PHILOSOPHY

Approved by:
Dr. Peter H. Dinolfo, Chair
Dr. Jacob Shelley
Dr. Esther Wertz
Dr. Peter Bonitatibus

Department of Chemistry and Chemical Biology
Rensselaer Polytechnic Institute
Troy, New York

[May 2023]
Submitted April 2023

TABLE OF CONTENTS

LIST OF TABLES v
LIST OF FIGURES vi
ACKNOWLEDGEMENT xi
ABSTRACT xvi
1. INTRODUCTION 1

1.1 The Climate Crisis, Energy Security, and New Technologies 1
1.2 Electrochromic Devices 3
1.3 Perylene Diimides 4
1.3.1 Introduction to Perylene Diimides 4
1.3.2 Synthesis of Functionalized Perylene Diimides 6
1.3.3 Targeting Specific Functionality 7
1.3.4 Unexpected Discovery of Perylene Diimide Isomers 11
1.4 Prior Work on Perylene Diimides in the Dinolfo Group 16
1.4.1 Functionalized Perylene Diimides 16
1.4.2 Self-Assembled Monolayers on Indium Tin Oxide 20
1.4.3 Copper-Azide Alkyne Cycloaddition Click Chemistry 22
1.4.4 Layer-by-Layer Thin-Film Assembly 24
1.4.5 Reversible Two Electron Reduction of Perylene Diimide on Indium Tin Oxide Surface 25
1.4.6 Thesis Outline 27

2. SYNTHESIS, ISOLATION, AND CHARACTERIZATION OF THIO-PDI DERIVATIVES 29

2.1 Synthesis of 1,6-, 1,7-, and 1,6,7-Thio-PDI Derivatives 29
2.1.1 Chemical Synthesis of 1,6-, 1,7-, and 1,6,7-Thio-PDI Derivatives 29
2.2 Characterization Analysis of 1,6-, 1,7-, and 1,6,7-Thio PDI Derivatives 32
2.2.1 NMR Analysis 32
2.2.2 Mass Spectroscopy Analysis 34
2.3 Chapter Summary 38

3. PHOTOPHYSICAL AND ELECTROCHEMICAL ANALYSIS OF THIO-PDI DERIVATIVES 40

3.1 Experimental Setup for Studies of PDI Derivatives 41
3.1.1 Electronic Absorption and Emission Spectroscopy 41
3.1.2 Computational Details 41
3.1.3 Chemical Reductions 42
3.2 Absorption 42
3.3 Emission 45
3.4 Quantum Yield 45
3.5 Lifetime Measurements 46
3.6 Lippert-Mataga Approximations 51
3.7 Density Functional Theory 53
3.8 Electrochemical Measurements 57

3.9 Chemical Reductions and CIE 58
3.10 Chapter Summary 61

4. PERYLENE DIIMIDE MULTILAYER ASSEMBLIES IN ELECTROCHROMIC MATERIALS 62

4.1 General Preparation and Synthesis of Layers and Linkers for Multilayer Assembly 63
4.1.1 Selection of Layer and Linker in Multilayer Assembly 63
4.1.2 Methods 65
4.1.3 NMR Analysis 69
4.2 Self-Assembled Monolayer Preparation 71
4.3 Multilayer Assembly of Perylene Diimide Thin-Film 72
4.4 Electrochemical Analysis of the Perylene Thin-Film 75
4.5 Chemical Reduction and CIE 79
4.6 Spectroelectrochemical Analysis of the PhO-Ph-PDI Multilayers 81
4.7 Potential Step Experiments 86
4.8 Concluding Remarks 92

5. CONCLUSION 96
6. FUTURE STUDIES 100
REFERENCES 102

LIST OF TABLES

Table 1. Spectral parameters of 1,6-Thio-PDI, 1,7-Thio-PDI, and 1,6,7-Thio-PDI in toluene observed for all parameters such as lifetime (τ), quantum yield (Φ_F), absorbance and emission peaks, and the calculated Stokes shift in wavenumbers (cm^{-1}). The twist angle was calculated from DFT geometry optimized structures as the dihedral angle between the 6 and 7 (1 and 12) positions on the perylene core..... 45

Table 2. Dipole moment changes derived by the Lippert–Mataga analysis. 52

Table 3. Lowest-lying singlet excited states calculated for 1,6-Thio-PDI, 1,7–Thio–PDI and 1,6,7–Thio–PDI at the CAM–B3LYP/may-cc-pVTZ level, with PCM solvation for THF. Vertical excitation energies (E), oscillator strengths (f), and dominant monoexcitations with contributions (weights) greater than 10% are indicated. 56

Table 4. Electrochemical parameters for 1,6-, 1,7-, and 1,6,7-Thio-PDI derivatives..... 58

Table 5. Determination of conversion to singly and doubly reduced states by comparison of cyclic voltammetry oeaks in varying electrolytes and solvents..... 78

Table 6. Determination of conversion to singly and doubly reduced states by comparison of spectroelectrochemical peaks to chemical reduction (CR) peaks..... 86

LIST OF FIGURES

Figure 1. Formation of Perylene-3,4,9,10-tetracarboxylic diimide (PTCDI) and 3,4,9,10-Perylene-tetracarboxylic dianhydride (PTCDA), which were obtained industrially via the oxidation of acenaphthene to yield 1,8-napthalic anhydride. 1,8-napthalic anhydride was further reacted under basic conditions to yield naphthalene-1,8-dicarboxylic acid imide. The oxidative coupling of naphthalene-1,8-dicarboxylic acid imide yields Perylene-3,4,9,10-tetracarboxylic diimide (PTCDI) which can undergo hydrolysis to yield 3,4,9,10-Perylene-tetracarboxylic dianhydride (PTCDA). This figure was adapted from.[60] 6

Figure 2. Perylene Diimide (PDI) labeled for the imide, bay (1,6,7,12), and ortho (2,5,8,11) positions with particular focus on the bay and ortho positions which are highlighted in red..... 8

Figure 3. Highest occupied (HOMO) and lowest unoccupied molecular orbitals (LUMO) are shown on the bottom and top respectively) for a Perylene Diimide (PDI) with cyclohexyl imide functionality with no bay or ortho functionality. 9

Figure 4. Bromination of PTCDA to form four distinct Br-PTCDA isomers, 1,6-Br-PTCDA, 1,7-Br-PTCDA, 1,6,7-Br-PTCDA, and 1,6,7,12-Br-PTCDA adapted from. [72] 12

Figure 5. Synthesis of several 1,6- and 1,7-PDI regioisomers adapted from previously published literature. The functional group added to the bay and imide position for the 1,6- and 1,7-PDIs are abbreviated in the figure as: bay group-imide group-PDI. A. 1,7- and 1,6-adamantl-Y-PDI synthesized by Slater et al.[78] where Y denotes the imide group. B. 1,7- and 1,6-Ar-octyl-PDI by Dey et al.[80] where Ar denotes the bay group which is an assortment of aryl functional groups. C. 1,7- and 1,6-tertbutylphenoxy-octyl-PDI by Dubey at al.[73] D. 1,7- and 1,6-tert-butylphenoxy-octyl-PDI by Dubey at al.[73] E. 1,7- and 1,6-pyrrolidine-octyl-PDI synthesized by Dubey at al.[73]F. 1,7- and 1,6-piperdinyl-R-PDI by Fan et al.[74] where R denotes the imide group. G. 1,7- and 1,6-3-pentamine-X-PDI Handa et al.[77] where X denotes the bay group which is an assortment of alkynes. 15

Figure 6. Synthesis of Propargyl -PDIs in which a Propargyl group is added to the imide position, and bay functionality includes p-(t-butyl)phenol (PhO-PDI), dodecanethiol (Thio-PDI) and pyrrolidine (Pyrr-PDI) adapted from [48] 18

Figure 7.A. Thin-film molecular assembly made from PhO-PDI, Thio-PDI, and Pyrr-PDI fabricated on a glass substrate. B. Visualization of a molecular assembly of PhO-PDI linked to Thio-PDI which is additionally linked to Pyrr-PDI through CuAAC click chemistry C. UV-Vis absorption profile for the thin-films of PhO-PDI (red line), Pyrr-PDI (green line), and Thio-PDI (purple line) beneath the sum of each individual component film (black line). Figure was adapted from.[48] 19

Figure 8. Generic Self-Assembling Molecule (SAM). 21

Figure 9. General scheme for formation of phosphonic acid Self-Assembled Monolayer (SAM) on cleaned hydrolyzed Indium Tin Oxide (ITO) surface adapted from.[85] 22

Figure 10. General Copper(I) Azide-Alkyne Cycloaddtion (CuACC) reaction to form a 1,4-triazole..... 23

Figure 11. Layer-by-Layer Assembly of Prgyl-PDIs using Copper-Azide Alkybe Cycloaddition reactions (CuAAC) on a Self-Assembled Monolayer (SAM) covalently attached to a conductive ITO surface adapted from.[48] 25

Figure 12. Cyclic voltammetry scans of one through five bilayers of PhOPDI (top), Thiol-PDI (middle) and Pyrr-PDI (bottom) assembled on an ITO electrode. CVs were obtained at scan rate of 1 V s 1 with 0.1 M TBAP in anhydrous acetonitrile as the electrolyte. The arrow shows the initial scan direction, adapted from.[48] 26

Figure 13. Synthesis of 1,6,7-Thio-PDI, 1,7-Thio-PDI, and 1,6-Thio-PDI, starting from Br–PTCDA, followed by imidization with diisopropylaniline, and finally substitution with dodecanethiol. 32

Figure 14. ^{1}H NMR of 1,6-Thio-PDI, 1,7-Thio-PDI, and 1,6,7-Thio-PDI in $CDCl_3$ highlighting the bay proton splitting pattern is located from around 8.7-9.0 ppm, and the diisopropyl proton splitting pattern is located from around 7.3-7.6 ppm. (spectra were referenced to the residual solvent peak $CHCl_3$ at 7.26 ppm.). 33

Figure 15. HR (top) and LR (bottom) mass spectra of 1,6-Thio-PDI using Direct Infusion Electrospray Ionization (ESI) 35

Figure 16. HR (top) and LR (bottom) 1,7-Thio-PDI (right) using Direct Infusion Electrospray Ionization (ESI). 36

Figure 17. HR (top) and LR (bottom) mass spectra of 1,6,7-Thio-PDI using Direct Infusion Electrospray Ionization (ESI). 37

Figure 18. LR mass spectra using Direct Infusion Electrospray Ionization (ESI) Br-PDI showing a mixture of 1,6-Br-PDI (m/z = 867), 1,7-Br-PDI (m/z = 867), and 1,6,7-Br-PDI (m/z = 945). 38

Figure 19. Visual representation of the perceived 1,6-, 1,7-, and ,1,67-Thio-PDI in tetrahydrofuran. 43

Figure 20. Normalized absorption and emission spectra for 1,6-Thio-PDI (top), 1,7-Thio-PDI (middle), and 1,6,7-Thio-PDI (bottom) in a range of solvents. Each emission spectra (ex 525nm) is scaled relative to the intensity of the sample taken in toluene. 44

Figure 21. Quantum yield data for 1,6-Thio-PDI (Φ =0.54 ± 0.002), 1,7-Thio-PDI (Φ =0.85 ± 0.004), and 1,6,7-Thio-PDI (Φ =0.16 ± 0.001), along with the standards Rhodamine 101 (Φ =1.00), LD Perchlorate 690 (Φ =0.63), and Oxazine Perchlorate (Φ =0.63).[134,135] 46

Figure 22. Representative frequency-domain fluorescence lifetime measurements of 1,6-ThioPDI in Toluene (top, lifetime = 6.6 ns, $\chi 2$ = 0.9873) and DMF (bottom, lifetime = 6.6 ns, $\chi 2$ = 1.376). Standard deviation parameters of dPhase = 0.5 and dMod = 0.01 were used to generate fit. 48

Figure 23. Representative frequency-domain fluorescence lifetime measurements of 1,7-ThioPDI in Toluene (top, Lifetime= 8.3 ns, $\chi 2$ = 0.6561) and DMF (bottom, Lifetime = 4.4 ns, $\chi 2$ =0.9834). Used standard deviation parameters of dPhase = 0.5 and dMod = 0.01 to generate fit. 49

Figure 24. Representative frequency-domain fluorescence lifetime measurements of 1,6,7-ThioPDI in Toluene (Lifetime= 4.4 ns, $\chi 2 = 0.918$) and DMF (Lifetime = 2.0 ns, $\chi 2 = 1.107$). Used standard deviation parameters of dPhase = 0.5 and dMod = 0.01 to generate fit..... 50

Figure 25. Comparison of the Stokes shift ($\boldsymbol{va - vf}$) derived from the absorption and emission properties, versus the solvent orientation polarizability (Δf) for the three isomers. The dashed lines represent the linear regression according to the Lippert–Mataga approximation utilizing equation 1. Data for 1,6-Thio-PDI is shown in blue, 1,7–Thio–PDI in red, and 1,6,7–Thio–PDI in green..... 52

Figure 26. Optimized molecular structures and frontier molecular orbitals for the three isomers, 1,6-Thio-PDI (left), 1,7-Thio-PDI (center), and 1,6,7-Thio-PDI (right). The highest occupied (HOMO) and lowest unoccupied molecular orbitals (LUMO) are shown on the bottom and top respectively. 55

Figure 27. Comparison of the energetic levels of the frontier molecular orbitals of PDI, 1,6-Thio-PDI, 1,7–Thio–PDI, and 1,6,7–Thio–PDI calculated at the CAM–B3LYP/may-cc-pVTZ level, with PCM solvation for THF. 55

Figure 28. Predicted electronic absorption spectra of 1,6-Thio-PDI (top), 1,7-Thio-PDI (middle), and 1,6,7-Thio-PDI (bottom) from TDDFT calculations at the CAM–B3LYP/may–cc–pVTZ/PCM(THF) level of theory. The simulated absorption spectra were generated using a 2000 cm^{-1} bandwidth for all peaks. The solid vertical lines correspond to the oscillator strengths of the calculated singlet transitions. 56

Figure 29. Cyclic Voltammetry (CV) scans for 1,6-Thio-PDI (top), 1,7-Thio-PDI (middle), and 1,6,7-Thio-PDI (bottom) at varying scan rates (0.10 V/s, 0.25 V/s, and 0.50V/s) to show the first and second reductions. CVs were obtained in 0.1 M of $TBAPF_6$ in anhydrous tetrahydrofuran as the electrolyte..... 57

Figure 30. UV−Vis–NIR absorption spectra of 1,6-Thio-PDI (top), 1,7-Thio-PDI (middle) and 1,6,7-Thio-PDI (bottom) recorded in THF with 0.01 M 18-crown-6. The singly and doubly reduced states were generated by chemical reduction using Na(Hg). The spectra of neutral states are shown as solid purple line, the singly reduced states as dashed grey lines, and the doubly reduced states as a dashed–dotted blue line. Included with the spectra are images of the cuvettes corresponding to the sample spectra. 59

Figure 31. CIE 1931 xy chromaticity diagram with points calculated for the neutral, singly and doubly reduced forms of the Thio–PDIs..... 60

Figure 32. J-type aggregation of a propargyl imide functionalized phenoxy PDI (PhO-Prgyl-PDI) (left) and H-type aggregation of a phenylacetylene imide functionalized phenoxy PDI (PhO-Ph-PDI) (right). Multilayer assembly was grown on glass with an N_3Mest linker. Figure was adapted from.[153] 64

Figure 33. PhO-Ph-PDI synthesis for click chemistry with the Br-PTCDA starting material previously synthesized by Dr. Peter Palomaki.[81] 69

Figure 34. N_3Mest linker synthesis from 1,3,5-tris(bromomethyl)benzene. 69

Figure 35. ^{1}H NMR of PhO-Ph-PDI PDI in $CDCl_3$ highlighting the aromatic proton splitting pattern which is located from around 7.0-10.5 ppm (spectra were referenced to the residual solvent peak $CHCl_3$ at 7.26 ppm.) 70

Figure 36. Self-Assembled Monolayer (SAM) preparation for Layer-by-Layer assembly with 1.5 mM of 12-azidododecylphosphonic acid in THF. 72

Figure 37. Layer-by-layer (LbL) assembly through Copper-Azide Alkyne Cycloaddition (CuAAC) “click” reactions of PhO-Ph-PDI with mestylene linker to achieve multilayer assembly. 74

Figure 38. Visible absorption profiles obtained during the growth of five bilayers of PhO-Ph-PDI with N_3Mest linker. 74

Figure 39. Comparison of layer rxn vs. the intensity of the absorbance peak at the maximum at 523 nm. 75

Figure 40. Normalized Cyclic Voltammetry (CV) scans for five layers of PhO-Ph-PDI with mestylene linker assembled on an ITO electrode. CVs were normalized by dividing the resultant current by the scan rate . CVs were obtained at varying scan rates (0.025 V/s, 0.05 V/s, and 0.10 V/s) with 0.1 M of $TBAPF_6$ in anhydrous methylene chloride as the electrolyte.. 76

Figure 41. Normalized Cyclic Voltammetry (CV) scans for five layers of PhO-Ph-PDI with mestylene linker assembled on an ITO electrode. CVs were normalized by dividing the resultant current by the scan rate. CVs were obtained at varying scan rates (0.10 V/s, and 0.25 V/s) with 0.1 M of $TMeAPF_6$. and 0.1 M of $TBAPF_6$ in anhydrous acetonitrile as the electrolyte. 76

Figure 42. UV−Vis–NIR absorption spectra of PhO-Ph-PDI recorded in THF with 0.01 M 18-crown-6. The singly and doubly reduced state were generated by chemical reduction using Na(Hg). The spectra of neutral stat are shown as solid pink line, the singly reduced state as dashed turquoise lines, and the doubly reduced state as a dashed blue line. Included with the spectra are images of the cuvettes corresponding to the sample spectra. 80

Figure 43. CIE 1931 xy chromaticity diagram with points calculated for the neutral, singly, and doubly reduced forms of PhO-Ph-PDI. 81

Figure 44. UV-Vis absorption spectra of $TBAPF_6$ (0.1 M) in methylene chloride (top) and $TMeAPF_6$ (0.1 M) in acetonitrile referenced to ferrocene/ferrocenium using spectroelectrochemical methods at 273 K. 84

Figure 45. Potential Step Spectroelectrochemistry experiment -0.4 to -1.0 volts with $TBAPF_6$ referenced to the ferrocenium/ferrocene couple where the (top) square-wave applied potential, (middle) resultant change in current, and (bottom) is the resultant change in absorbance. 88

Figure 46. Potential Step Spectroelectrochemistry experiment -0.4 to -1.4 volts with $TBAPF_6$ referenced to the ferrocenium/ferrocene couple where the (top) square-wave applied potential, (middle) resultant change in current, and (bottom) is the resultant change in absorbance. 88

Figure 47. Potential Step Spectroelectrochemistry experiment -1.0 to -1.4 volts with $TBAPF_6$ referenced to the ferrocenium/ferrocene couple where the (top) square-wave applied potential, (middle) resultant change in current, and (bottom) is the resultant change in absorbance. 89

Figure 48. Potential Step Spectroelectrochemistry experiment -0.4 to -1.0 volts with $TMeAPF_6$ referenced to the ferrocenium/ferrocene couple where the (top) square-wave applied potential, (middle) resultant change in current, and (bottom) is the resultant change in absorbance. 89

Figure 49. Potential Step Spectroelectrochemistry experiment -0.4 to -1.4 volts with $TMeAPF_6$ referenced to the ferrocenium/ferrocene couple where the (top) square-wave applied potential, (middle) resultant change in current, and (bottom) is the resultant change in absorbance..... 90

Figure 50. Potential Step Spectroelectrochemistry experiment -1.0 to -1.4 volts with $TMeAPF_6$ referenced to the ferrocenium/ferrocene couple where the (top) square-wave applied potential, (middle) resultant change in current, and (bottom) is the resultant change in absorbance..... 90

ACKNOWLEDGEMENT

I would like to acknowledge my thesis advisor Dr. Peter Dinolfo for his mentorship, patience, and support throughout the completion of my Ph.D. at Rensselaer Polytechnic Institute (RPI). Dr. Dinolfo was always available for my questions, he aided me in trouble-shooting difficult chemical syntheses, provided me with the experience to learn a variety of instrumentation methods under his tutelage, improved my writing quality, and taught me how to become more confident and self-reliant as an academic researcher. Additionally, Dr. Dinolfo was always supportive of my unique background as an Indigenous/First Nations student and championed my leadership efforts within the American Indian Science and Engineering Society (AISES) and at RPI. Dr. Dinolfo also championed my professional dreams and gave me the freedom to explore my career in research through my participation in the Department of Energy Graduate MEISPP Program in May 2021.

In addition to Dr. Dinolfo, I would like to thank my fellow researchers within the Dinolfo group for their knowledge, professionalism, and steadfastness to conducting research during the COVID pandemic. I would like to acknowledge past group members who have influenced my life as a researcher. I would like to thank Zhaorui Huang for his preliminary synthesis and multilayer fabrication work which provided many of the chemical precursors for my chromophores which I synthesized for my research. I would like to thank Nate Anderson for his mentorship and time dedicated to helping me run fluorescence lifetime measurements. I would like to thank Guangyu Hu for teaching me the Dinolfo group's multilayer fabrication technique, a technique which is essential for completion of my thesis research. I would like to thank my fellow Ph.D. candidate Charlie McCabe. Charlie McCabe who survived the COVID 19 pandemic with me and is well known for his leadership, mentoring, hard work, ability to trouble shoot difficult problems, his

excellent sardonic humor, and really is well known as the beating heart and soul of the Dinolfo group. I would also like to thank all other group members in the Dinolfo group including past and current members David Honz, Chris Almquist, Naomi Robinson, Rebecca Ryan, Tyler Mucci, Jeremy Brinker, Huimin Guoh, Caius Jacott, Andrea Mitchell, Darian Topolski and many more. I really enjoyed going out with everyone to group outings and summer BBQs. I know I can be a little standoffish and aloof, so these group outings really helped me get out of "my shell," even if we all did get COVID together that one time. I lived, so I am going to say it was worth it.

In addition to my research group, I would also like to thank all the excellent professors in our department. Through teaching, I have had the chance to work alongside some excellent teachers. Dr. Liz Sprague was the first person to teach me how to work with undergraduate students and she instilled in me exceptionally high standards for organization, cleanliness, and preparedness when teaching. I also am thankful for Dr. Alexander Ma and Dr. Kathleen Morrissey, who were always incredibly warm, approachable, and hardworking colleagues which I knew I could count on. In addition to teaching, I would like to thank the professors in my department who either taught me or gave me kind advice during the emotional turmoil of my Ph.D. It is no secret that I am a terrible standardized test taker and thus bombed all my entrance exams in Fall 2017. My Ph.D. was not off to an auspicious start, and thus I redid about half of my undergraduate degree at RPI. By redoing these undergraduate courses, I had a chance to get to know some excellent professors like Dr. Jacob Shelley and Dr. Gerald Korenowski. I would like to thank my committee members for their time and input in my research, including Dr. Peter Dinolfo, Dr. Jacob Shelley, Dr. Peter Bonitatibus, Dr. Esther Wertz. It has not been an easy road to get here. I appreciate your patience with me while I have made mistake after mistake, hopefully learning something worthwhile after each mistake.

I would also like to thank my friends who helped alleviate stress during my degree as good friends are known to do. Thank you, Welby Huynh, Howie Nguyen, Chandula Walgama, Adrianne Gelbach, Sambit Ghosh, Michael Bramson, Montwaun Young, Cody Edson, Pooja Goswami, Kenning Lang, Jamie Keddy, and Arshia Singh. I would like to thank my fellow Indigenous Engineers and Scientists at the American Indian Science and Engineering Society (AISES) who provided me with a diverse and far-reaching academic family, as well as a sense of belonging in higher education which helped me overcome my internalized imposter syndrome. Thank you to the AISES Board of Directors, AISES Council of Elders, AISES CEO Sarah Echohawk, Lisa Paz, Monique Tulley-Bahe, Cody Kapotik, McKalee Steen, Hannah Balderas, Makayla Mathers, Steven Just, Brielle Thorson, Jacob Calderone, Amber Nashoba, Brook Thompson, Anna Jacobson-Eckert, Sarah Lowry, Angie Applewhite, and Amada Arroyo being my indigenous STEM family. We are not "crabs in a bucket;" to each other, we are a "barrel of monkeys," lifting each other out of our colonized past-together, and into a brighter future. We are the future of STEM. And that future looks bright!

I would like to thank my academic family at my alma matter, San Jose State University (SJSU). At SJSU I received excellent mentorship within the Research Initiative for Scientific Enhancement (RISE) Program, run by Dr. Karen Singmaster, where I met peers from underrepresented backgrounds like mine own. Being a part of RISE taught me that I belong in STEM and am capable to pursuing a Ph.D. Thank you Fauna Yarza, Elvia Silvia, Mizuki Johnson, and Roberto Tovar amongst others who emotionally supported me during some of the most difficult times in my life. I know that without the mentorship and friendships, which I received in RISE, I would not have believed myself capable of pursuing a Ph.D. I would also like to thank my undergraduate research advisor, who first recognized my potential in research and provided me

with the confidence to pursue it and much more, Dr. Gilles Muller. Dr. Muller was perhaps the first person to ever believe in my academic abilities and saw something in me that was worth mentoring when I had very little confidence in myself as a 21-year-old. Working with Dr. Muller in his research laboratory first kindled my love of research and made me believe I could achieve more in my professional aspirations than I had dared to dream before. My whole life I thought I was academically average, and due to this mentorship, and innate belief in me and my abilities, I became academically exceptional. I would not have received my doctorate without the mentorship I received from Dr. Muller.

Finally, I would like to thank my biological family. My immediate and extended family alike, I know is all rooting for me to succeed. My extended family includes my living grandparents Elizabeth Campbell and Ivar Riives who have educated me on my ancestry and believed in my ability to succeed in school since I was a child. My extended family also includes my many loving aunts and uncles back home in Canada, particularly my Uncle Paul, Auntie Diana, and Auntie Alice, with Auntie Alice also giving me a lifeline to my indigenous background which I am fairly ignorant of. My extended family also includes all my beautiful cousins, nieces, and nephews who I think of when I study. I never had the chance to grow up around you with a content in between us, but I hope that my hard work shows that I aspire to do the right thing in life. I hope it shows that I aspire to be a good person and a role model for my nieces and nephews.

For my immediate family, I would like to thank my brother Alexander Riives, my sister Louise Riives, my mom Patricia Campbell, my dad Rolland Riives, and my pet gerbils, Hermione, Prudence, and Germaine Chiseler. While Hermione and Prudence never lived long enough to see my thesis defense, I loved them dearly. Surprisingly, Germaine gerbil played an essential part in my thesis writing. During thesis writing, when my stress led to paralysis, I would often watch

Germaine sleep in front of my space heater which I had set up next to my desk. Watching this innocent critter sleep soundly gave me some much-needed life perspective, reminding me that life is short, not to take anything too seriously, and that I eventually need sleep too as I am a living being just as she is. During thesis writing, from January to March, I do not think in my life I have ever worked harder whilst fearing economic hardship and potential professional failure. While my parents paid to keep a roof over my head during those months, I devoted my heart and soul to my thesis, knowing that it required all my focus regardless of my dwindling paltry bank account. However, with the defense done and thesis content approved by Dr. Dinolfo and my thesis committee, it has all been worth it.

Having successfully defended my Ph.D., I never imagined as a child, that I would one day be here given my early difficulties in school due to dyslexia and ADHD. Being held back in second grade due to my neurodivergence led me to stand a head taller than all the other students in my first-grade class. This humiliating experience I think, has provided me with a healthy amount of stoic cynicism and humility early on in my life. Both of which, has served me well as an appropriate catalyst to later succeed in my education- if sometimes through sheer force of will and against many odds. Thank you, mom, and dad, for always stressing the importance of education, helping me overcome and live with my dyslexia, learn to love my “unique” brain, and financially supporting me throughout my lengthy, lengthy, lengthy, education process. I never would have believed in my wildest dreams as a child that I would be here today. I love you.

ABSTRACT

1,6-, 1,7-, and 1,6,7- derivatives of dodecylthio–N,N'– (2,4–diisopropylphenyl)-3,4,9,10-perylenetetracarboxylic diimide, and N,N'-Di(4-ethynylphenyl)-1,7-di(4-tert-butylphenoxy)-3,4:9,10-perylenebis-(dicarboximide) (**PhO-Ph-PDI**) were synthesized, isolated, and characterized. The three Thio-PDI derivatives, **1,6**–**Thio**–**PDI**, **1,7**–**Thio**–**PDI**, and **1,6,7**–**Thio**–**PDI**, displayed noticeable differences in their photophysical properties including their absorption and emission spectra, fluorescence quantum yield, fluorescence excited state lifetimes, and excited state dipole moments as calculated by the Lippert-Mataga analysis. Additionally, the Thio-PDI derivatives exhibited different colors at neutral and reduced state as determined by chemical reduction and CIE calculations. These studies determine that different PDI derivatives can provide unique photophysical contributions as building blocks within the molecular assemblies which comprise new technologies such as electrochromic (EC) devices. Comparatively, **PhO-Ph-PDI** was utilized as the primary building block within a molecular assembly for potential use in EC materials. A molecular assembly, or thin-film, of **PhO-Ph-PDI** was fabricated Copper Azide-Alkyne Cycloaddition reactions. The **PhO-Ph-PDI** thin-film was studied with $TBAPF_6$ and $TMeAPF_6$ in various solvents to study electrolyte size penetration within the **PhO-Ph-PDI** thin-film. Different reduced states were probed with cyclic voltammetry studies, spectroelectrochemical studies, and potential step spectroelectrochemical studies. These studies revealed that a combination of a smaller $TMeAPF_6$ electrolyte and a longer applied potential allowed for better cation penetration through the **PhO-Ph-PDI** thin-film. This better penetration of the thin-film led to higher conversion of reduced states which is an essential criteria of EC devices. While the **PhO-Ph-PDI** thin-film did not achieve full conversion to all reduced states with either electrolyte, analysis of the **PhO-Ph-PDI** thin-film provides better understanding of

the criteria required to improve molecular assemblies for EC devices. This includes selection of appropriate sized electrolyte and synthetic design of molecular assembly channel size by appropriate selection of chromophores utilized within the molecular assembly.

1. INTRODUCTION

1.1 The Climate Crisis, Energy Security, and New Technologies

Unchecked energy dependency on fossil fuels, or non-renewable energy sources, accelerates climate change, impending environmental disaster, and the depletion of finite sources of energy.[1] Additionally, global populations are projected to reach 10 billion by the year 2050,[2] with the demand for energy expected to increase by more than 300 % by 2100. Thus, as the global population increases, the ability to meet the energy demands of consumers globally, also referred to as energy security, requires all available energy sources, both renewable and non-renewable. Renewable energy sources include solar, wind, and geothermal sources amongst others. Non-renewable energy sources include oil, natural gas reserves, and coal reserves amongst others.[3] Despite the possibility of utilizing renewable energy sources for increased energy security in the future, current renewable energy technologies only make-up a small portion within the energy sector. In 2021, renewable energy only accounted for about 12.4 % of total U.S. primary energy consumption. [4] The remaining energy consumption in 2021 was met with non-renewable energy sources. Clearly, U.S. energy consumption, and global energy consumption as a whole, is still heavily reliant on non-renewable energy sources.[5] This reliance on non-renewable energy sources does not promote lasting energy security because non-renewable energy sources are finite. Thus, the reliance on non-renewable energy sources contributes not only to climate change and impending environmental disaster, but also contributes to future global energy insecurity.

The development of new technologies is essential to reduce contributions to climate change, ensure future global energy security, and improve the quality of life for the consumers which purchase these technologies. One direction for the improvement of renewable technologies

includes the development of electrochromic (EC) technologies which can reduce consumer energy consumption. EC technologies are made up of materials which can change or bleach color, when they undergo an electron-transfer process.[6] This change in color, particularly from a lighter to darker color, is useful in devices such as smart windows. When smart windows change from a light to dark color, this can influence the amount of solar radiation which penetrates through the glass and into the building. This increase or decrease of solar radiation can significantly reduce heating and cooling costs in buildings.[7]

A 2022 report by the International Energy Agency[8] found that the heating and cooling of buildings accounted for 30 % of global energy consumption. Thus, EC technologies like smart windows to reduce heating and cooling could dramatically decrease global energy consumption. Other EC technologies include smart displays can cycle between two different colored oxidized and reduced species.[9] EC technologies can also be used in visualized energy storage where the charging and discharging a of a device show distinct color differences to alert the consumer to the battery life. EC technologies can also be used in wearable electronics such as eyewear applications which can change from light to dark upon reduction or oxidation. Additionally, many EC technologies utilize a lower energy consumption relative to current displays available on the market such as organic light emitting diodes (OLED)s and light emitting diodes (LCD)s due to their ability to maintain an optical state without a continuous input of electrical power.[10] Overall, emerging EC technology can be made to utilize less power,[11] and can be paired with multiple substrates including glass,[12] plastic,[13] fibers,[14] and metals[15] which increases their range of versatility in a variety of applications. Thus, whether EC technologies are utilized to decrease energy consumption through controlling solar radiation in smart windows, or decrease energy consumption because they maintain an optical state without continuous electrical power as shown in displays and wearable electronics, EC technology can overall reduce energy consumption. This

decrease in energy consumption through the development of EC technologies can aid in providing future energy stability and reducing human contributions to climate change.

1.2 Electrochromic Devices

As previously discussed, electrochromic (EC) devices rely on a type of electrochemically driven redox process which changes the color, transmittance, and reflectivity within the device.[9] The device can undergo these redox processes as a result of the materials which make up the device. There are many types of materials which are incorporated into these devices. The most commonly cited materials are inorganic materials such as WO_3,[16] TiO_2,[17] NiO,[18] polymers such as polythiophene,[19–21] metal organic complexes,[22,23] and small organic molecules such as viologens[24] and small organic redox dyes.[25–27]

There are notable advantages and disadvantages when considering whether to use an inorganic, polymer, metal organic complex, or small organic molecule within a device. Some considerations for a device include the stability of the device, how intense the color is when in the reduced and oxidized species, and response speed when switching between reduced and oxidized states. Inorganic materials exhibit excellent photostability but lack intense coloration and exhibit a slow response speed when switching.[28] Comparatively, polymers are easy to fabricate through solution processing techniques but it is difficult to achieve spectral purity, which limits their intense coloration within devices. [29,30] Unlike inorganic materials and polymers, small organic redox dyes can exhibit intense coloration but their small size and small corresponding weight leads to stability issues in within devices.[31] However, small organic dyes can have their color fine-tuned through chemical functionalization[9] which allows for a greater range of intense colors within the devices if stability issues can be accounted for. This manuscript will focus on adding to the body

of knowledge on materials used within these emerging technologies. In the next portion of this manuscript we will discuss the EC material, or small organic dye molecule called a "perylene diimide," which we will utilize in our EC device in order to make contributions to this emerging and promising field.

1.3 Perylene Diimides

1.3.1 Introduction to Perylene Diimides

Perylene-3,4,9,10-tetracarboxylic diimide and their derivatives, also referred to as perylene diimides (PDIs), are a type of functionalized polycyclic aromatic hydrocarbon derived from 3,4,9,10-Perylenetetracarboxylic dianhydride (PTCDA). PDIs are robust organic chromophores which have garnered significant attention in both commercial and academic research.[32,33] PDIs have been utilized since the 1950s as high performance dyes and pigments due to their exceptional chemical, photo, and thermal stability,[33] as well as their high tinctorial strength that allows for hues ranging from red to purple.[34] PDIs possess excellent chemical properties, such as good electron mobility, tunable absorption spectra, excellent stability to photooxidation,[35] and high fluorescence quantum yields.[32] This range of chemical properties make PDIs attractive for a variety of applications. For example, PDIs have been applied towards fingerprint detection,[36] heparin detection,[37] photodynamic therapy,[38] and live cell staining.[27] Additionally, due to their excellent optical properties and relatively high electron affinity,[39,40] PDIs have been studied for use in photovoltaic applications,[41–43] light emitting diodes,[44,45] light-harvesting arrays,[46–48] fluorescent solar collectors,[49,50] organic field-effect transistors,[51,52] and dye sensitized solar cells.[53–55] Notably, one group citing a 17% efficiency in a single junction organic solar cell incorporating PDIs.[56]

Early derivatives of PTCDA, such as perylene tetracarboxylic acid dimethylimide, were used as vat dyes for textile fibers until 1950.[57] In 1950, Harmon Colors devised a new method to convert vat dyes to pigments through reacting PTCDA with primary aliphatic or aromatic amines in high boiling solvents. These PTCDA derivatives and PDIs pigments were utilized as high performance dyes and pigments for industrial processes.[58] They were attractive in these industrial processes due to their exceptional chemical, photo, and thermal stability,[33] as well as their aforementioned high tinctorial strength,[57] depending both on the chemical structure of the PDI and molecular packing within the solid state.[59] Despite their exceptional chemical, photo, and thermal stability, as well as hue range, PDIs were limited in their utility outside of dyes and pigments, until precise structural manipulation could be achieved.

While PDIs and PTCDAs have been used industrially for almost one hundred years, precise structural manipulation of the PDI moiety for other applications were only recently achieved. A common method to achieve the desired PDI derivative is to first synthesize its starting precursor PTCDA. PTCDA can be obtained in relatively high yield through the condensation reaction between PTCDA and an alkyl amine or analine.[33,34] A common synthesis adapted from[60] in Figure 1 shows the formation of both perylene-3,4,9,10-tetracarboxylic diimide (PTCDI) and PTCDA. Both PTCDI and PTCDA can be used as an excellent synthetic precursor to the desired functionality on the PDI. Further synthetic details on specific functionalization of PDIs will be discussed in the next portion of chapter.

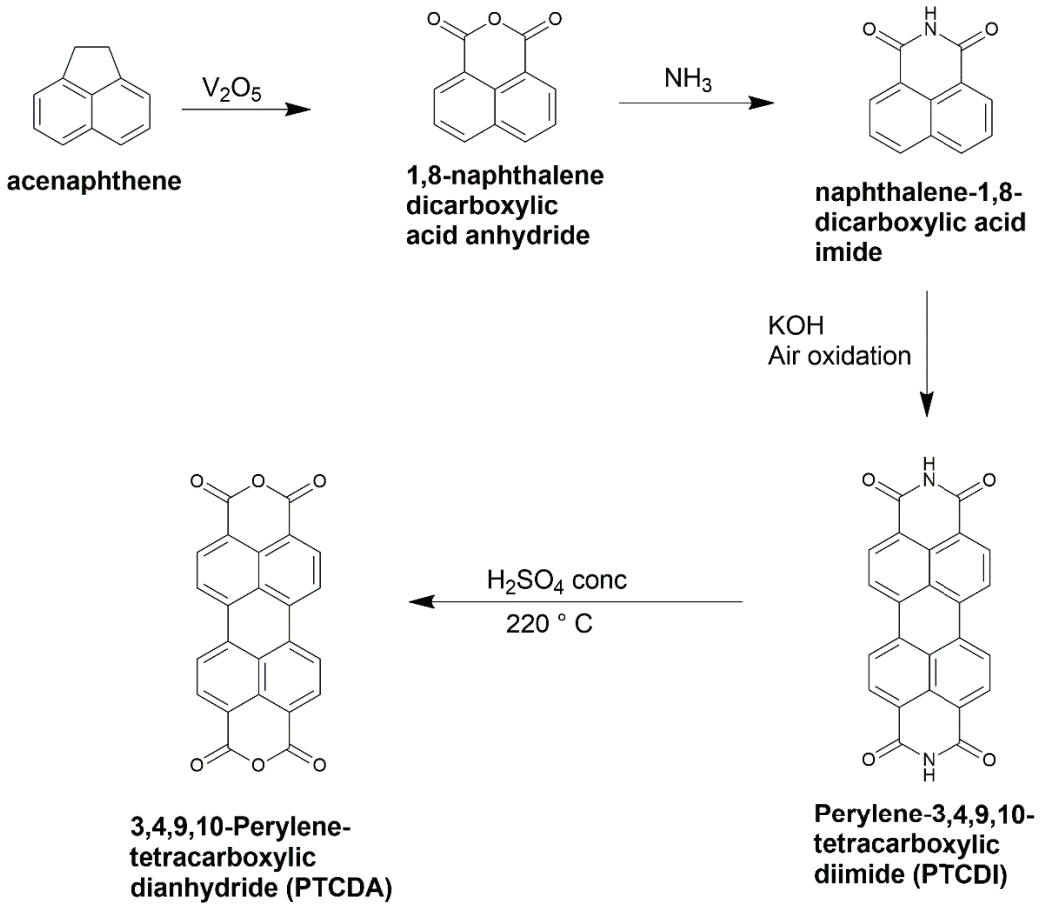

Figure 1. Formation of Perylene-3,4,9,10-tetracarboxylic diimide (PTCDI) and 3,4,9,10-Perylene-tetracarboxylic dianhydride (PTCDA), which were obtained industrially via the oxidation of acenaphthene to yield 1,8-napthalic anhydride. 1,8-napthalic anhydride was further reacted under basic conditions to yield naphthalene-1,8-dicarboxylic acid imide. The oxidative coupling of naphthalene-1,8-dicarboxylic acid imide yields Perylene-3,4,9,10-tetracarboxylic diimide (PTCDI) which can undergo hydrolysis to yield 3,4,9,10-Perylene-tetracarboxylic dianhydride (PTCDA). This figure was adapted from.[60]

1.3.2 Synthesis of Functionalized Perylene Diimides

Despite their discovery in 1913 and utility as unique dyes and pigments by Harmon Colors, PDIs have only recently achieved precise structural manipulation within the last thirty years. Due to their conjugated π system, PTCDA and most PDIs precursors are highly insoluble in typical organic solvents. This insolubility stems from π to π stacking of the aromatic rigid core in organic solvents. Thus, traditional organic synthetic methods which rely on solubility to synthesize and

isolate PDI precursors have not been successful. This inability to synthesize and isolate PDI precursors has stymied chemist's attempts to precisely manipulate the structure of PDI to achieve specific desired chemical and physical properties. Given the exceptional chemical, photo, and thermal stability of early PTCDA derivatives observed by Harmon Colors in the 1950s, chemists' inability to access these exceptional properties proved exceptionally frustrating given the potential of these PDI dyes and pigments. Thankfully, overcoming PTCDA and PDI precursors solubility issues stems from distorting the conjugated π system so that π-π stacking is minimized. The conjugated π system can be distorted through addition of bulky substituents which block π to π stacking. However, the type of functional group, which is added to PDI precursors, the order of functional groups to add, and the location on the conjugated π system are all considerations when synthesizing PDIs. In this section of this manuscript, we will discuss the synthesis of the most relevant types PDIs and how various synthetic techniques are used to improve and overcome PDI precursor solubility issues to achieve specifically tailored PDIs for a variety of utilities across disciplines.

1.3.3 Targeting Specific Functionality

The excellent chemical properties of PDIs and their vast potential utility is largely due to their readily derivatizable structure. The PDI moiety contains a rigid π conjugated core comprised of two naphthalene half units, providing three distinct regions for chemical modification, the bay (1,6,7,12), imide, and ortho (2,5,8,11) positions[32,33,39] as shown in Figure 2. There are a variety of synthetic methods to add functionality to each position.

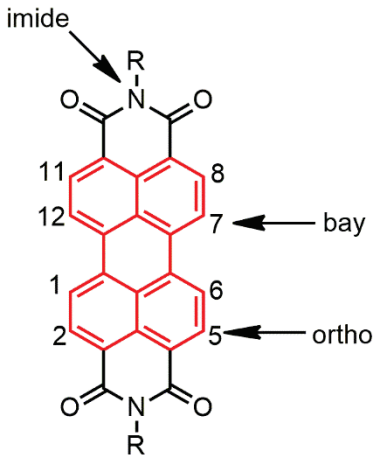

PDI

Figure 2. Perylene Diimide (PDI) labeled for the imide, bay (1,6,7,12), and ortho (2,5,8,11) positions with particular focus on the bay and ortho positions which are highlighted in red.

The bay (1,6,7,12) position is perhaps the most important position within the PDI moiety. The bay position is responsible for tuning the electrical and optical properties within the PDI due to the significant HOMO and LUMO coefficients at these positions as shown in Figure 3.[39,60] The addition of π donating functional groups stabilizes the HOMO, whereas π accepting groups stabilize the LUMO.[32] For both the HOMO and LUMO, adding functionality to the bay position generally follows multiple synthetic reactions in which bulky electron donating or electron withdrawing groups and other supramolecular structures can be added to the electron dense PDI π conjugated system.[39]

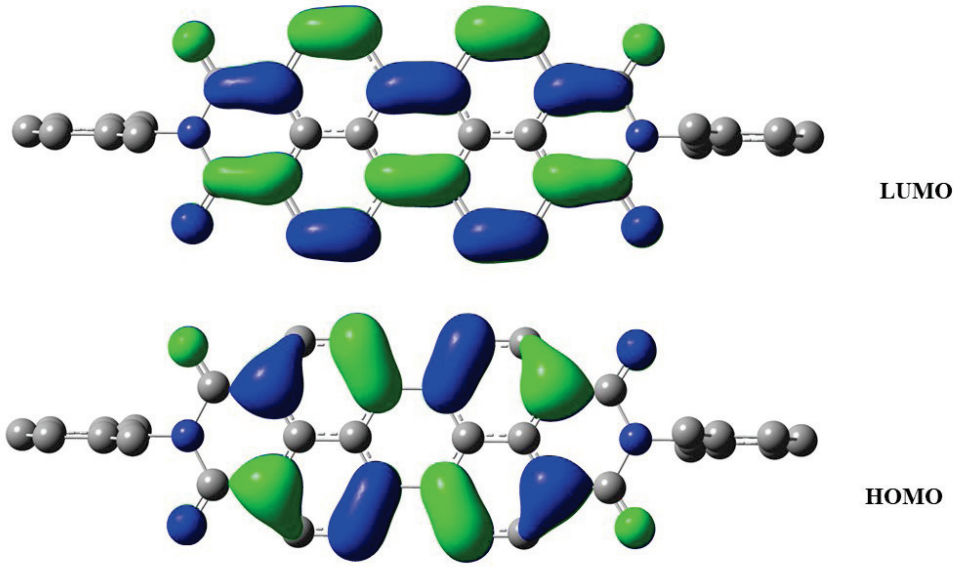

Figure 3. Highest occupied (HOMO) and lowest unoccupied molecular orbitals (LUMO) are shown on the bottom and top respectively) for a Perylene Diimide (PDI) with cyclohexyl imide functionality with no bay or ortho functionality.

The functionalization of the bay position often starts with halogenation reaction of PTCDA or PTCDI derivatives to achieve a halogenated product. This halogenated product can then undergo a further substitution reaction[61] as the halide is far more reactive than the starting PTCDA or PTCDI. The first halogenation of a PTCDI derivative was by BASF[62] in 1989 in which a chlorinated N,N'-di-butylperylimide was used to form a tetrachloro- perylene diimide derivative. This tetrachloro- perylene diimide derivative can then undergo further nucleophilic displacement to add phenoxy functionality to the 1,6,7,12- position in relatively low yields. In addition to low yields, this chlorination reaction is not regiospecific and forms tri- and pentachloro-perylene diimide derivatives which cannot be easily separated.[63]

In 1997, BASF improved their selection of halogens from chlorine to bromine through bromination of PTCDA[64] to yield 1,7-dibromoperylene-3,4,9,10-tetracarboxylic dianhydride (1,7-Br–PTCDA). Compared to chlorination, bromination overall had a much greater success rate at

product formation.[65] Additionally, Osswald et al.[66] determined that the larger the size of the halogen added to the bay position, the greater a propeller-type distortion occurs which increases the dihedral angle between the 1,12 and 6,7 positions. This increased dihedral angle distorts the planar structure of the PDI core and has the additional benefit of increasing PDI solubility within organic solvents which may aid in purification. Additionally, the 1,7-Br-PTCDA provides an excellent starting compound for further nucleophilic or metal catalyzed cross-coupling reactions. Following this disclosure, researchers utilized the bromination procedure to functionalize the bay positions with numerous functional groups, including phenoxy, pyrrolidinyl, alkyl, aryl, and aryloxy groups, among others.[32,33,39]

The imide position is not responsible for tuning the electrical and optical properties within the PDI because nodes in the HOMO and LUMO orbitals are centered at the imide nitrogen.[67] Instead, chemical modifications at the imide region are used to increase the solubility of PDIs in organic solvents.[39] This increased solubility is important because PDIs and their precursors are notoriously insoluble in most organic solvents due to their tendency to aggregate via face-to-face π-π stacking. [32,33,39,68] The π-π stacking is reduced because adding functionality at the imide position twists the PDI out of the plane in which the π to π stacking occurs. Some of the most common imide substitution inlcudes bulky aryl groups, 2,6-diisopropylphenyl i.e., as well as linear and branched alkyl chains refered to as "swallow tails."[69]

Functionalization at the ortho (2,5,8,11) positions are not well cited in literature as compared to the bay and imide position. Functionalization to the ortho position does not increase solubility of the PDI in organic solvents like functionalization of the imide position.[32] The ortho position in specific tuning of the electrical and optical properties within the is comparatively less certain. However, the ortho position has been used to facilitate further specific functionalization around the PDI moiety. One publication cites directed ortho-metallation, followed by a halogen or

boron quench as an effective method to reduce the inherent reactivity within the PDI. This reduction in reactivity can aid in formation of specific regioisomers.[39] The use of the ortho position for more specificity is also cited in other literature. The reaction of ortho-unfunctionalized PDIs with organophosphorous regent,[70] and the reaction of n-heterocyclic carbene[71] can be utilized to substitute halogen atoms on aromatic scaffolds. Yet, at this point, there is not a wide variety of publications on ortho substitution.

1.3.4 Unexpected Discovery of Perylene Diimide Isomers

In 2004 Würthner et al. discovered[72] that the BASF bromination of PTCDA was not regioselective for 1,7-dibromo–PTCDA (1,7-Br-PTCDA), but also lead to the formation of 1,6-dibromo–PTCDA (1,6-Br-PTCDA) as well as the 1,6,7-tribromo-PTCDA (1,6,7-Br-PTCDA). The 1,6-Br-PTCDA, 1,7-PTCDA, and the 1,6,7-PTCDA occurred in a 76:20:4: ratio. Since 2004, a select number of publications described the isolation and comparison between the photo– and electrochemical properties of 1,6– and 1,7–PDI regioisomers with different substituents. These substituents include phenoxy,[73] pyrrolidinyl,[72,73] piperidinyl,[74] aryl,[75] fluorenyl,[76] alkynyl,[77] alkyl,[77] and thioether.[78]

There are many potential synthetic avenues to achieve 1,6- and 1,7-PDI regioisomers with the desired bay or imide functionality. Many synthetic avenues start with bromination of PTCDA to form an isomeric mixture of Br-PTCDA[72] (1,6-Br-PTCDA, 1,7-Br-PTCDA, 1,6,7-Br-PTCDA, and 1,6,7,12-Br-PTCDA) as shown in Figure 4. As previously mentioned, bromine provides an excellent starting compound for further nucleophilic or metal catalyzed cross-coupling reactions.[65] Figure 5. shows several different bay and imide functionalized 1,6- and 1,7-PDIs. Comparatively, 1,6,7-PDI and 1,6,7,12-PDIs are rarely cited in literature relative to 1,6- and 1,7-PDI. This is

because the 1,6,7-PDI and 1,6,7,12-PDI occur in much lower yeilds in the intial bromination reaction[72] with yeilds further decreasing with each additional synthetic step and purification processes. The purificaiton processes for PDI isomers will be discussed further in this chapter, but it is important to note that Figure 5. only compares 1,6- and 1,7-PDIs, and not 1,6,7- or 1,6,7,12-PDIs.

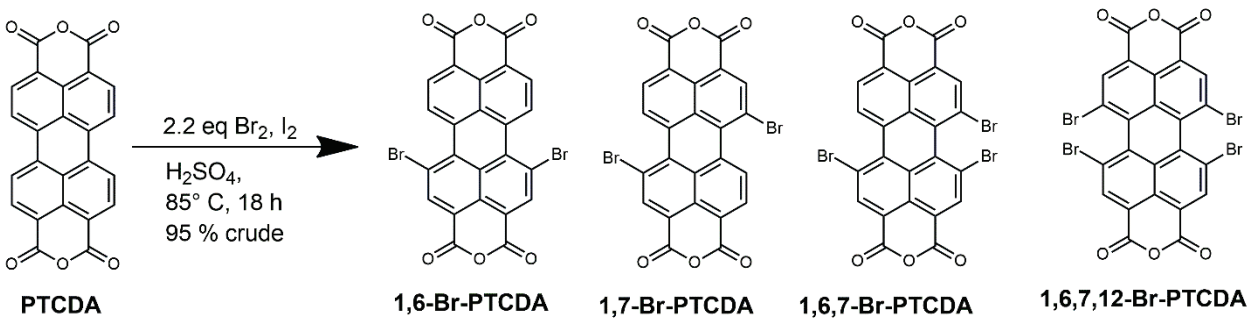

Figure 4. Bromination of PTCDA to form four distinct Br-PTCDA isomers, 1,6-Br-PTCDA, 1,7-Br-PTCDA, 1,6,7-Br-PTCDA, and 1,6,7,12-Br-PTCDA adapted from. [72]

Following the bromination products, 1,6- and 1,7-Br-PTCDA are not separated at this stage in the synthesis reaction due to the insolubility of Br-PTCDA in organic solvents. As previously mentioned, PDIs and their precursors (Br-PTCDA) are notoriously insoluble in most organic solvents due to their tendency to aggregate via face-to-face π-π stacking. [32,33,39,68] The π-π stacking is reduced because adding functionality at the imide position twists the PDI out of the plane in which the π to π stacking occurs. Thus, most separation of PDI precursors occurs after the addition of an imide substituent, and potentially a bay substituent. Regardless, the more functionality added (bay, imide, or even ortho) to distort the PDI out of plane, the more facile it is to separate out isomers either with column chromatography or recrystallization methods.[78]

Depending on the desired imide, or bay functionality on the PDI, it may be more facile to add either an imide group first, or a bay group first to Br-PTCDA. In Figure 5 there are several different types of imide and bay functionalities for the regisisomers of 1,6- and 1,7-PDI. In the

first reaction scheme A, 1,6- and 1,7-PDI is functionalized with adamantyl bay substituents and varying butyl, ethylhexyl, and 2,4-dibutoxybenzyl imide substituents by Slater et al.[78] In their paper Slater et al. do not discuss imide functionalization of Br-PTCDA, but instead focus on bay functionalization. To introduce the bay substituent, Slater et al. applied a modified palladium coupling synthesis from Kosugi et al.[79] to introduce the adamantylthio unit into the perylene core. In the second reaction scheme B, 1,6- and 1,7-PDI is functionalized with various aryl bay substituents and a long chain octyl imide substituents by Dey et al.[80] In their paper, Dey et al first add n-octylamine to the imide position following a simple reflux in propionic acid as outlined by a 2011 paper by Dubey et al.[73] In their paper, Dubey et al. were able to produce the octyl-Br-PDI product in good yields, and isolate the 1,6- and 1,7- isomers through column chromatography to yield 1,6-, 1,7-, and even 1,6,7-Br-octyl-PDI products. As previously mentioned, adding imide functionality increases solubility of the PDI and allows for potential separation of isomers, but successful isolation of brominated isomers is not observed very frequently in literature. Many syntheses involving 1,6- and 1,7-PDI isomers involve separation as a final step after all functionalization. Thus, separation of these 1,6-, 1,7-, and 1,6,7-Br-octyl-PDI products is somewhat remarkable. After the 1,6-, 1,7-, and 1,6,7-Br-octyl-PDI were isolated, Dey et al. added various aryl functionality to the bay position through a series of Suzuki coupling reactions. In the third and fourth reaction schemes C and D, 1,6- and 1,7-PDI isomers are functionalized with a 4-tert-butylphenoxy bay substituent in C and a 2,4-tert-butylphenoxy substituent in D, synthesized by Dubey et al. [73] Both 1,6- and 1,7-PDI in C and D have the same long chain octyl imide substituents mentioned in B. After adding imide functionality, both the 4-tert-butylphenoxy 2,4-tert-butylphenoxy substituent are added by nucelophilic substituetion reactions with the bromine atoms. In the fifth reaction scheme E, 1,6- and 1,7-PDI is functionalized with pyrrolidine aryl bay substituents and the same long chain octyl imide substituents mentioned in B, by Dubey et al.[73]

Similar to C and D, pyrrolidine is added with a nucelophilic substitution reaction. The sixth reaction scheme F, the 1,6- and 1,7-PDI is functionalized with a piperdinyl bay substituent and a varying cyclohexyl, butyl, and branched alkyl imide substituents by Fan et al.[74] Neither the imide functionalization or bay functionalization is discussed in great detail, other than perhaps a replacement reaction of the bromine atoms on 1,6- and 1,7-Br-R-PDI with piperdinyl substituents. Finally, the seventh reaction scheme G, the 1,6- and 1,7-PDI is functionalized with a bulky triphenyl propyne and non-bulky hexyl bay substituent and a varying cyclohexyl, butyl, and branched pentane imide substituents by Handa et al.[77] In their paper, Handa et al. first reacted 3-aminopentane, to add 3-pentane to imide position. Bay functionality was added with standard Sonogashira coupling conditions.

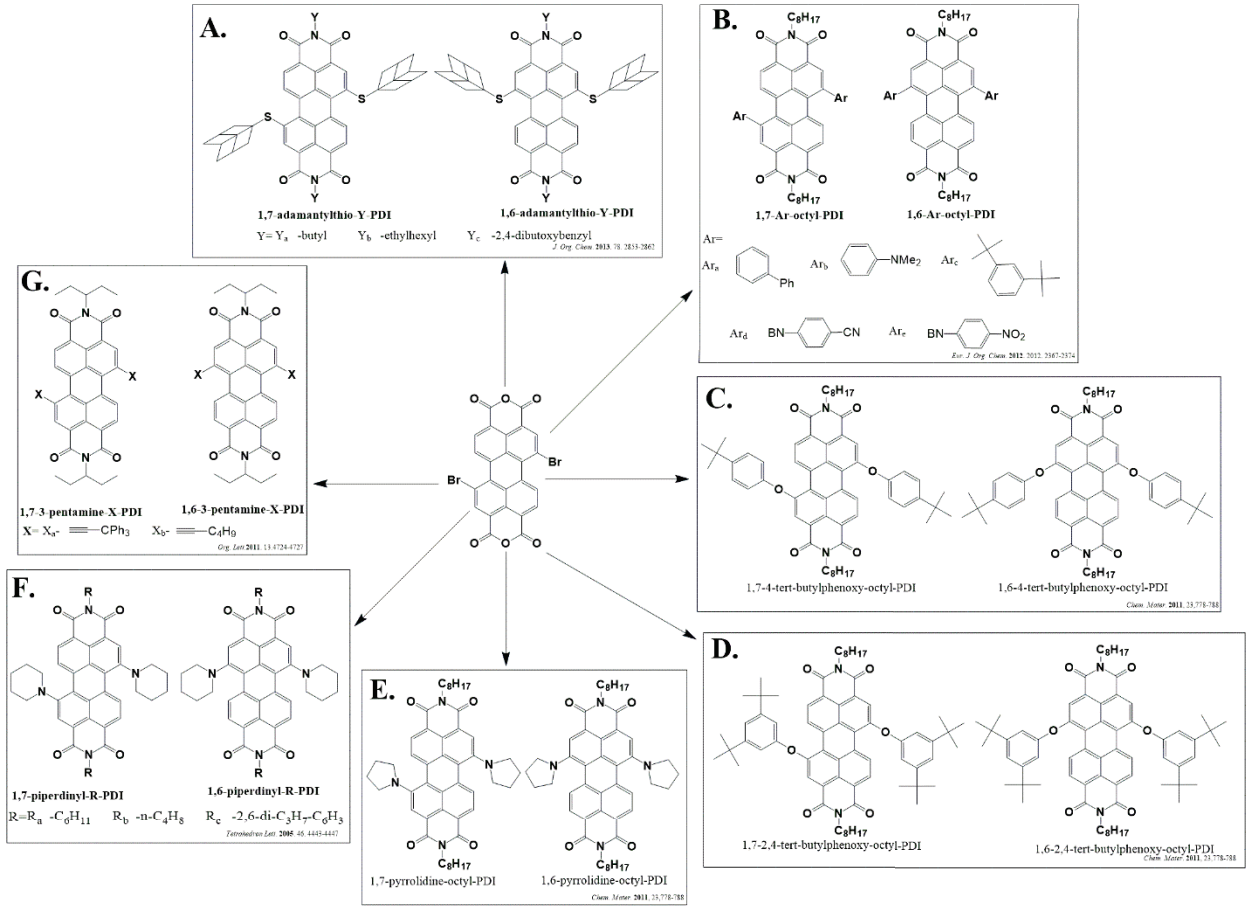

Figure 5. Synthesis of several 1,6- and 1,7-PDI regioisomers adapted from previously published literature. The functional group added to the bay and imide position for the 1,6- and 1,7-PDIs are abbreviated in the figure as: bay group-imide group-PDI. A. 1,7- and 1,6-adamantl-Y-PDI synthesized by Slater et al.[78] where Y denotes the imide group. B. 1,7- and 1,6-Ar-octyl-PDI by Dey et al.[80] where Ar denotes the bay group which is an assortment of aryl functional groups. C. 1,7- and 1,6-tertbutylphenoxy-octyl-PDI by Dubey at al.[73] D. 1,7- and 1,6-tert-butylphenoxy-octyl-PDI by Dubey at al.[73] E. 1,7- and 1,6-pyrrolidine-octyl-PDI synthesized by Dubey at al.[73]F. 1,7- and 1,6-piperdinyl-R-PDI by Fan et al.[74] where R denotes the imide group. G. 1,7- and 1,6-3-pentamine-X-PDI Handa et al.[77] where X denotes the bay group which is an assortment of alkynes.

In summation, PDIs are an exceptionally versatile and exciting small organic molecule to utilize in a variety of applications. While PDIs have been used in industry for the better part of a century due to their exceptional chemical, photo, thermal stability,[33] and high tinctorial strength that allows for hues ranging from red to purple,[34] their tendency to π-π stack limited their utility until recently. [32,33,39,68] The disclosure of the 1997 BASF patent[64] has allowed for a synthetic renaissance of various bay, imide, and ortho functionalized PDIs. Of these functional groups, the bay position is perhaps the most important, as any functionality added at the bay position directly

interactions with the HOMO and LUMO coefficients at these positions.[39,60] Due to the HOMO and LUMO coefficients at bay position, functionalization fine tunes the photophysical properties of the PDI. PDIs are an attractive material for EC technologies due to their high tinctorial strength[34] and due to the ability to fine tune the photophysical properties through bay functionalization. Additionally, the discovery of regiosiomers by Würthner et al.[72] in 2004 allows for even more variety when utilizing PDIs in variety of applications. In this next secion of the manuscript, we will examine past work done with PDIs within the Dinolfo group and how these PDIs can be fabricated into a molecular assembly, or thin film, which has utility in a variety of applications including dye-sensitized cells (DSSCs) and EC technologies.

1.4 Prior Work on Perylene Diimides in the Dinolfo Group

1.4.1 Functionalized Perylene Diimides

Past work with perylene diimides (PDIs) in the Dinolfo group[48] has specialized in using PDIs to create panchromatic assemblies for light-harvesting arrays (LHAs) for use in dye-sensitized cells (DSSCs) and artificial photosynthesis. To fabricate these panchromatic assemblies, the unique photophysical properties of three bay functionalized PDIs: p-(t-butyl)phenol (PhO-PDI), dodecanethiol (Thio-PDI) and pyrrolidine (Pyrr-PDI) are considered. These PDIs can be easily synthesized, as shown in Figure 6, and are similar to what is already cited in literature as shown in Figure 5. Additionally, they also demonstrate utility in LHAs due to their absorbance spectra spanning the visible portion of the electromagnetic spectra. The combined absorbance spectra of PhO-, Pyrr-, and Thio-PDI is shown in Figure 6. These PDIs are also attractive to use in LHAs as the synthesis of these PDIs is facile and fabricating these PDIs into an LHA is relatively easy as well. The propargyl group which is added to the PDI

derivatives in Figure 6 is not added for stability or to increase the solubility of the PDI in organic solvents, but instead links together multiple PDIs in tandem to fabricate molecular assemblies through a process called copper azide-alkyne cycloaddition,[81] or CuACC, click chemistry. CuAAC click chemistry was used to fabricate these molecular assemblies made of PhO-, Pyrr-, and Thio-PDI was completed previously in the Dinolfo group[48] as shown in Figure 7. The use of PhO-, Pyrr-, and Thio-PDI as building blocks within a molecular assembly has a variety of benefits. As previously discussed, PDIs possess high tinctorial strength[34] which correspond to the intense color observed within the molecular assembly. As PhO-PDI is red, Pyrr-PDI is green, and Thio-PDI is purple, the corresponding molecular assembly comprised of PhO-PDI is red, Pyrr-PDI is green, and Thio-PDI is purple.

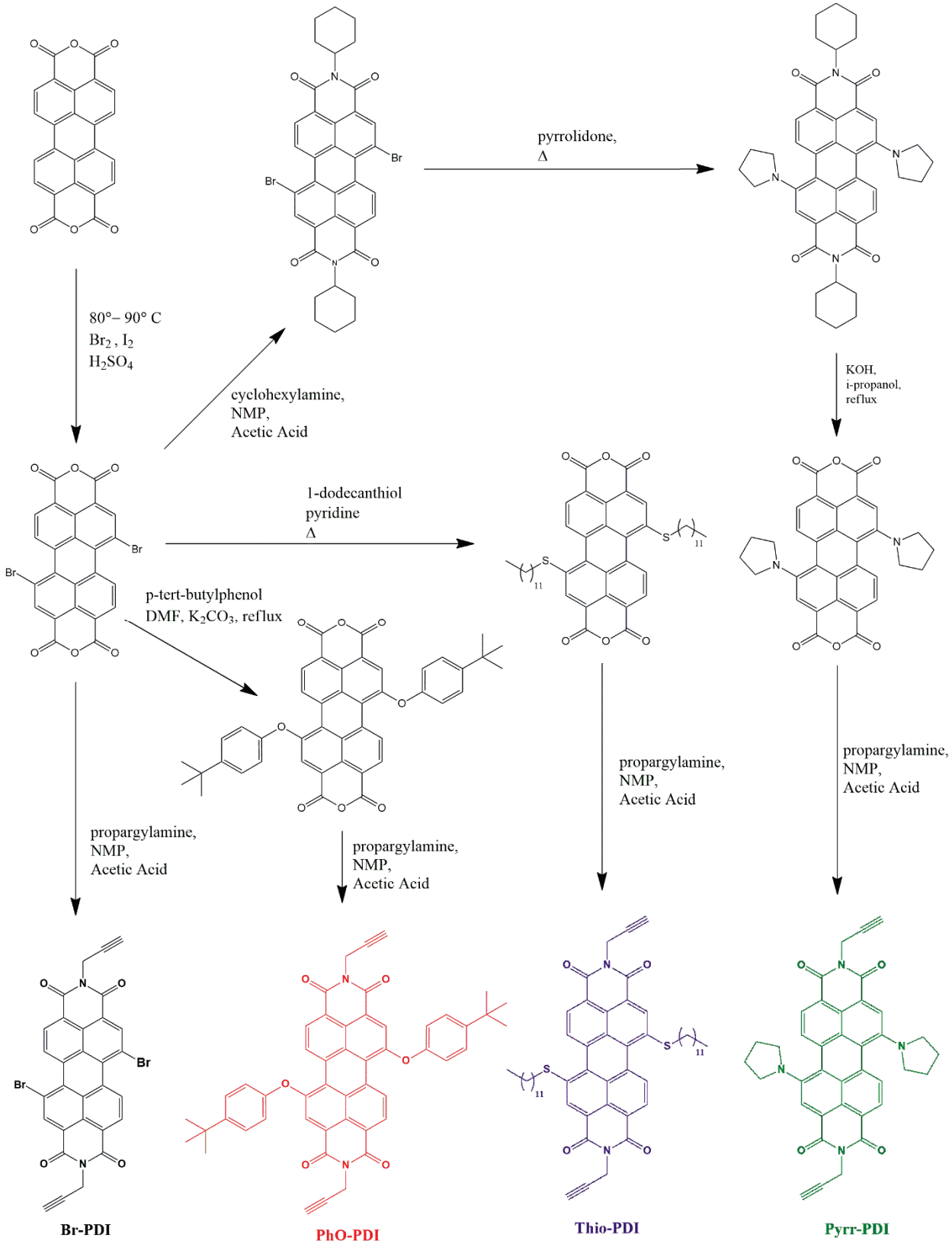

Figure 6. Synthesis of Propargyl -PDIs in which a Propargyl group is added to the imide position, and bay functionality includes p-(t-butyl)phenol (PhO-PDI), dodecanethiol (Thio-PDI) and pyrrolidine (Pyrr-PDI) adapted from. [48]

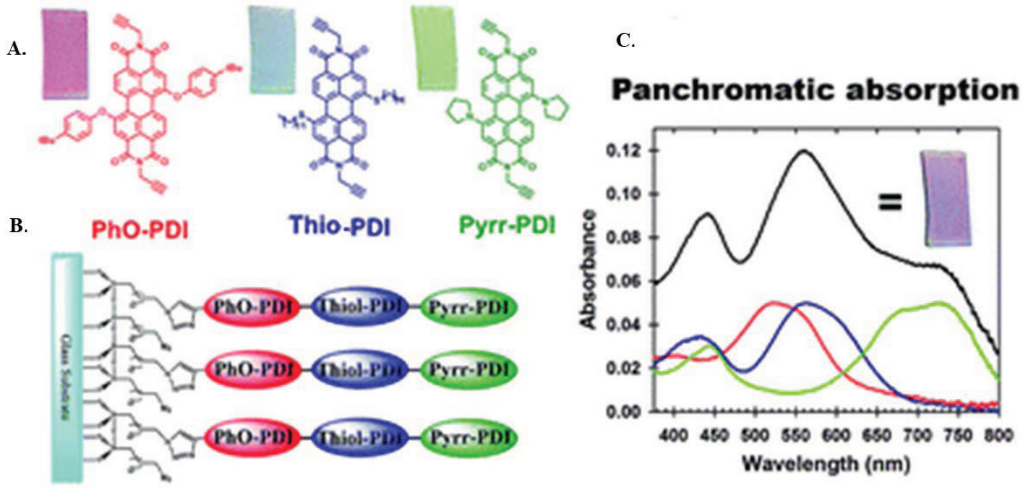

Figure 7.A. Thin-film molecular assembly made from PhO-PDI, Thio-PDI, and Pyrr-PDI fabricated on a glass substrate. B. Visualization of a molecular assembly of PhO-PDI linked to Thio-PDI which is additionally linked to Pyrr-PDI through CuAAC click chemistry C. UV-Vis absorption profile for the thin-films of PhO-PDI (red line), Pyrr-PDI (green line), and Thio-PDI (purple line) beneath the sum of each individual component film (black line). Figure was adapted from.[48]

In addition to the high tinctorial strength of the PDI within the molecular assembly, other intrinsic properties of the PDI building blocks are also expressed within the molecular assembly. The intense color associated with each of the PDIs corresponds to a specific absorption spectra within the molecular assembly. These specific absorption spectra can be modified through combining different PDIs with the molecular assembly. For example, by linking together a PhO-PDI to a Thio-PDI to a Pyrr-PDI within a molecular assembly, the individual absorption profile of PDI can be combined into a panchromatic absorption profile which is a sum of its individual PDI components. Figure 7A shows a photograph of each PDI fabricated on glass. The PhO-PDI molecular assembly is red, the Thio-PDI is purple, and the Pyrr-PDI is green. Figure 7B shows a visualization of the three PDIs linked in tandem through CuAAC click chemistry. Figure 7C shows the panchromatic absorption profile of the PDIs linked in tandem in Figure 7B. Thus, from past work within the Dinolfo group,[48] the intrinsic properties of PDIs such as their high

tinctorial properties and corresponding absorption profile can be expressed within a molecular assembly through CuAAC click chemistry. The next portion of this manuscript will discuss how molecular assemblies can be fabricated through CuAAC click chemistry onto a self-assembled monolayer (SAM).

1.4.2 Self-Assembled Monolayers on Indium Tin Oxide

To assemble multilayers into a surface, the surface must be modified chemically through the use of a self-assembled monolayer (SAM). SAMs are molecular layers that assemble on a surface through adsorption.[82] There are three general parts to a SAM, the head group, the alkyl chain, and the terminal end group,[83] as shown in Figure 8. The head group is responsible for anchoring the molecule to the surface. The alkyl chain provides stability for the SAM via Van der Waals interactions and significantly influences the ordering of the SAM.[84] The tail provides a location for further chemical reaction to attach other molecules to the SAM. Overall, SAM quality, or molecular surface coverage, is dependent on the solvent conditions and a variety of other factors.[85] There are several different SAM preparations available in literature. The most common preparations include thiol, siloxane, and phosphonic acid. Thiol is often fabricated on gold through formation of the gold-sulfur bond. Siloxane SAMs, trihalo- and trialkoxysilanes are often fabricated on glass and silicon[86] amongst other surfaces, through covalent adsorption processes onto the surface. Siloxane SAMs are highly dependent on water content, solvent, how degraded the solution is, the temperature, and deposition time. The mechanism for formation of siloxane SAMs is not yet well understood. Relative to thiol and siloxane, phosphonic acid generated SAMs creates a more robust monolayer than chemisorbed carboxylic acid. The annealing of the phosphonic acid maximizes the number of P-O bonds to the metal oxide lattice.[87,88] Adsorption

kinetics and conditions for phosphonic acid have been investigated with organophosphonic acids on a variety of different oxide surfaces. The surface hydroxyl groups on the conductive oxide surface promote adsorption of the organophosphonate with adhesion of the phosphonate group based on acid-base interactions.

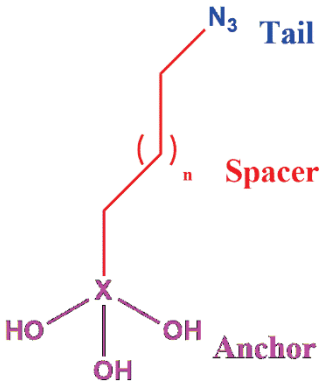

Figure 8. Generic Self-Assembling Molecule (SAM).

Previous work done by the Dinolfo group used siloxane SAMs,[48,81,89,90] but gradually it was determined that molecular surface coverages were inconsistent and not well reproducible between batches of siloxane SAMs. Additionally, siloxane SAM preparation required an anhydrous, air-free environment in which the exchange between the hydroxyl groups on the surface and the siloxane required constant heating and a multiple step reaction.[86] Comparatively, the phosphonic acid SAMs are a one-step reaction which is done under air at room temperature in only 24 hours.[85] Most importantly, the phosphonic acid SAMs provide consistent surface coverage at a fraction of the effort required to fabricate siloxane SAMs. Thus, phosphonic acid SAMs were selected for multilayer assembly of the PDI multilayer LHA.

Phosphonic acid SAMs can be fabricated on a variety of surfaces including glass, metal, metal-oxides, and semiconductors. Due to the versatility of surfaces which SAMs can be grown on, SAMs have potential applications in electronics and biological devices. Of these surfaces, Indium Tin Oxide (ITO) has perhaps the greatest utility in a variety of applications. ITO is a

transparent conductive material which is widely used in optoelectronic devices as within plasmas, touch displays, liquid crystal displays, fluorescence microscopy, and in solar applications like organic light emitting diodes (OLEDs).[91–93] Given the utility of ITOs in photovoltaic applications, its use as a transparent conductor, and relative facile nature of fabricating a SAM, we chose to grow our phosphonic acid SAMs on ITO for further fabrication multilayer assembly, or LHAs which is shown in Figure 9.

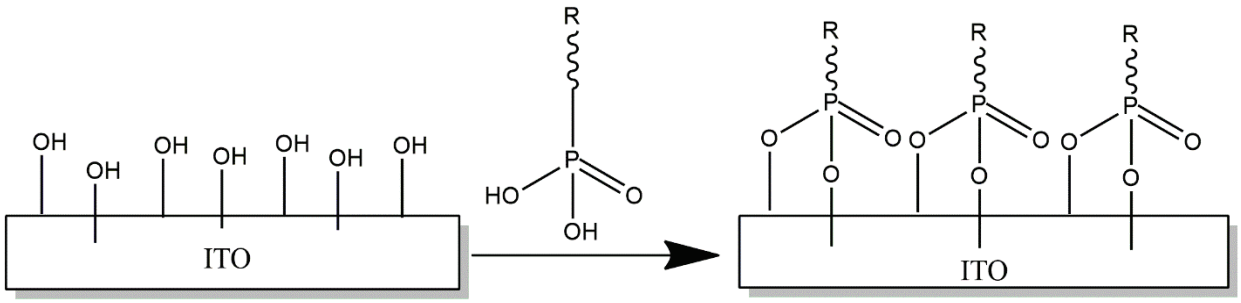

Figure 9. General scheme for formation of phosphonic acid Self-Assembled Monolayer (SAM) on cleaned hydrolyzed Indium Tin Oxide (ITO) surface adapted from.[85]

1.4.3 Copper-Azide Alkyne Cycloaddition Click Chemistry

Copper-Azide Alkyne Cycloaddition (CuAAC) click reaction is a specific subset of the 1,3-Dipolar cycloaddition reaction, or Huisgen 1,3-dipolar reaction, in which an alkyne and azide react to form a five-membered heterocycle.[94] The 1,3-dipolar cycloaddition reaction is a very kinetically stable reaction but exceedingly slow often requiring increased temperature and long reaction times to form the desired triazole.[95–97] Comparatively, the CuACC click reaction, occurs when a terminal alkyne and aliphatic azide react in the presence of a Cu (I) catalyst, to form a 1,4-disubstituted[1,2,3]-triazole. The CuACC click reaction combines the kinetic stability of alkynes and azides in the 1,3-dipolar cycloaddition reaction with a Cu (I) catalyst to increase the reaction rate 7 orders of magnitude.[98] Thus, compared to the 1,3-dipolar cycloaddition reaction occurring

in hours or even days, the CuACC click reaction occurs in mere minute, increasing the reaction ate by several orders of magnitude. The CuACC click reaction is shown in Figure 10.

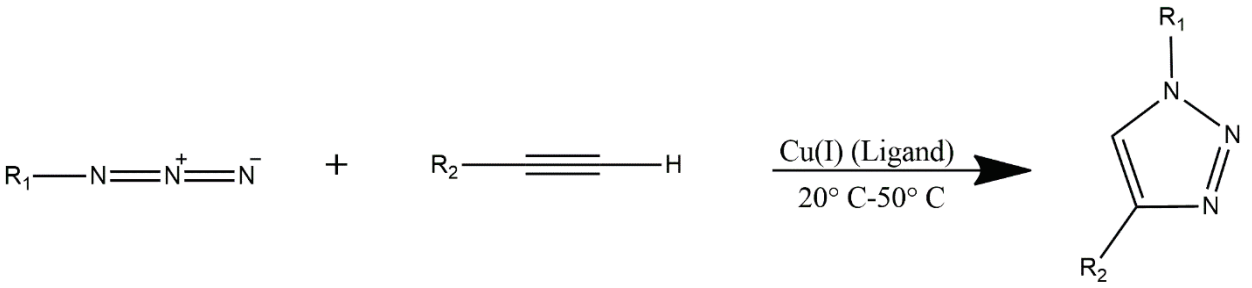

Figure 10. General Copper(I) Azide-Alkyne Cycloaddtion (CuACC) reaction to form a 1,4-triazole.

The extreme increase in the reaction rate of the 1,3-dipolar cycloaddition reaction with the Cu (I) catalyst was first observed by Tornøe and Meldal,[99] and Sharpless laboratories,[100] independently. It was observed that the Cu(I) catalyst improved both the regioselectivity, and most notably, rate of the 1,3-dipolar cycloaddition reaction. The CuACC click reaction forms 1,4-disubstituted[1,2,3]-triazole high yields which is stable due to its chemical inertness to most processes such as oxidation, reduction, and hydrolysis.[101]

The use of CuAAC click reactions to form triazoles are cited in a variety of publications. Some key publications in this field are included in the following. A 2003 publication by Kolb and Sharpless et al.[102] cites the use of Cu (I) catalyst, in the presence of a terminal acetylene and azide, to form a 1,2,3-triazole. A 2007 communication by Binder et al.[103] utilizes the CuAAC click reaction to grow polymeric substrates with control over ligand density within the polymer. A 2007 review by Lutz et al.[104] discusses the role of CuAAC click reactions to prepare triazole-containing dentrimers, protein conjugation with synthetic polymers,[105] and the construction of highly functional nanomaterials, or SAMs, with application in molecular electronics, catalysts, or biosensors.[106–110] Whether the utility of the CuACC click reaction is used in polymerization[111,112] formation of dendrimers[113,114] and gels,[103] biochemical studies and drug discovery,[102,115] in vivo

tagging,[116,117] biomolecular ligation,[118,119] and materials science, particularly the development of self-assembled monolayers (SAMs), [104,120]clearly the CuAAC click reaction's ability to form stable triazoles in mere minutes has utility across disciplines.

1.4.4 Layer-by-Layer Thin-Film Assembly

Applying the CuAAC click reaction, multilayers of propargyl functionalized PDIs, (PhO-PDI, Pyrr-PDI, and Thio-PDI) were attached to a conductive ITO surface through a preprepared SAM as previously achieved in the Dinolfo group.[48] All Prgyl-PDIs yielded ordered, reproducible, and uniform films providing a proof of concept. The multilayer assembly is formed through clicking a first layer of chromophore with alkyne functionality to an azide functionalized SAM through CuAAC reactions as shown in Figure 10. In Figure 10, a triazole is formed between the SAM and chromophore. This triazole formation between the chromophore and SAM is shown in Step 2 of Figure 11. Next, a linker with azide functionality is added to undergo the same CuAAC click reaction in which the alkyne of the chromophore already attached the SAM and the azide of the linker form a triazole. This is shown in Step 3 of Figure 11. Layers of additional chromophores are added between linkers in an alternating fashion shown through repeating Steps 2 and 3 in Figure 11. This repeat of clicking layers, linkers, and then layers again will be referred to as a layer-by-layer (LbL) multilayer fabrication assembly. By using the CuAAC click reaction in the LbL assembly, the desired number of layers of chromophores can be achieved. These multiple layers of chromophores are what will be referred to as multilayer assembly.

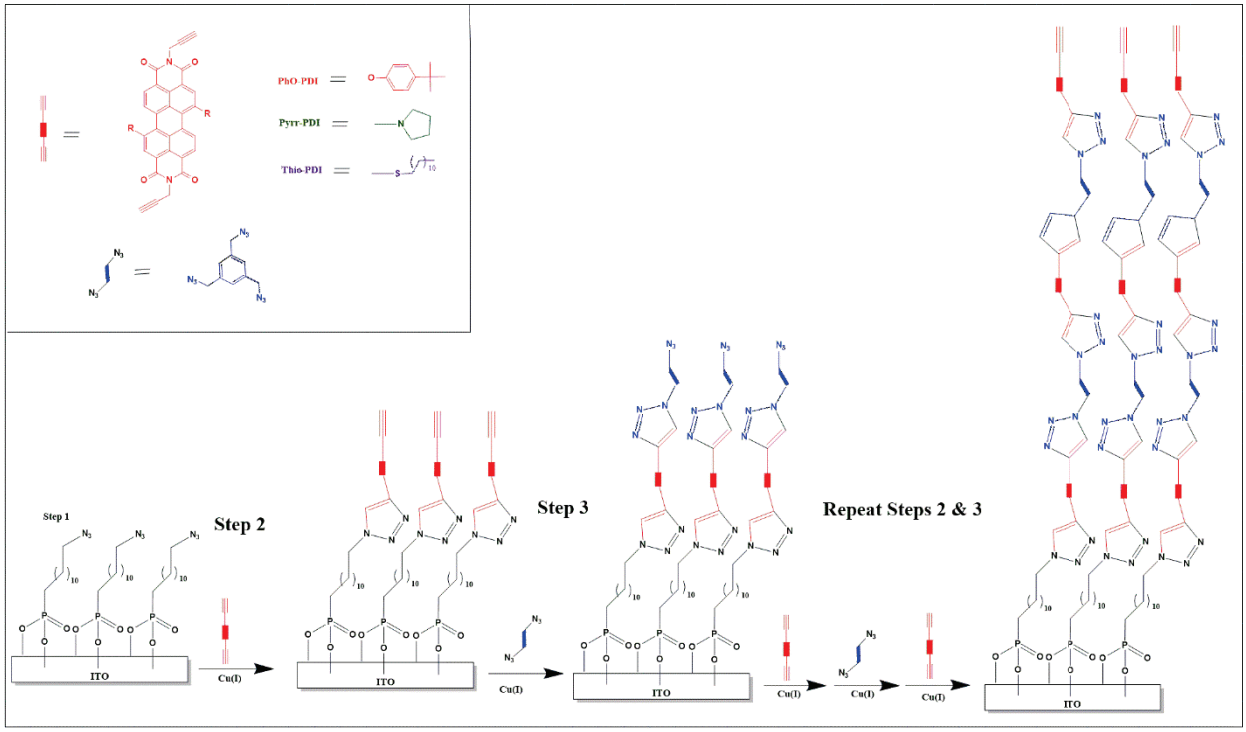

Figure 11. Layer-by-Layer assembly of Prgyl-PDIs using Copper-Azide Alkybe Cycloaddition reactions (CuAAC) on a Self-Assembled Monolayer (SAM) covalently attached to a conductive ITO surface adapted from.[48]

1.4.5 Reversible Two Electron Reduction of Perylene Diimide on Indium Tin Oxide Surface

The multilayer assembly to form thin-films of Prgyl PDIs (PhO-PDI, Thio-PDI, and Pyrr-PDI) can be grown and studied on conductive ITO. One method to study PDI thin-films involves whether PDI thin films can undergo reversible oxidation and reduction reactions. Cyclic voltammetry scans were preformed to observe two reversible one electron reduction peaks as shown Figure 12. Figure 12 show CVs at 1 V/s for 1, 2, 3, 4 and 5 bilayers in which the charge increases linearly per layer.[121]

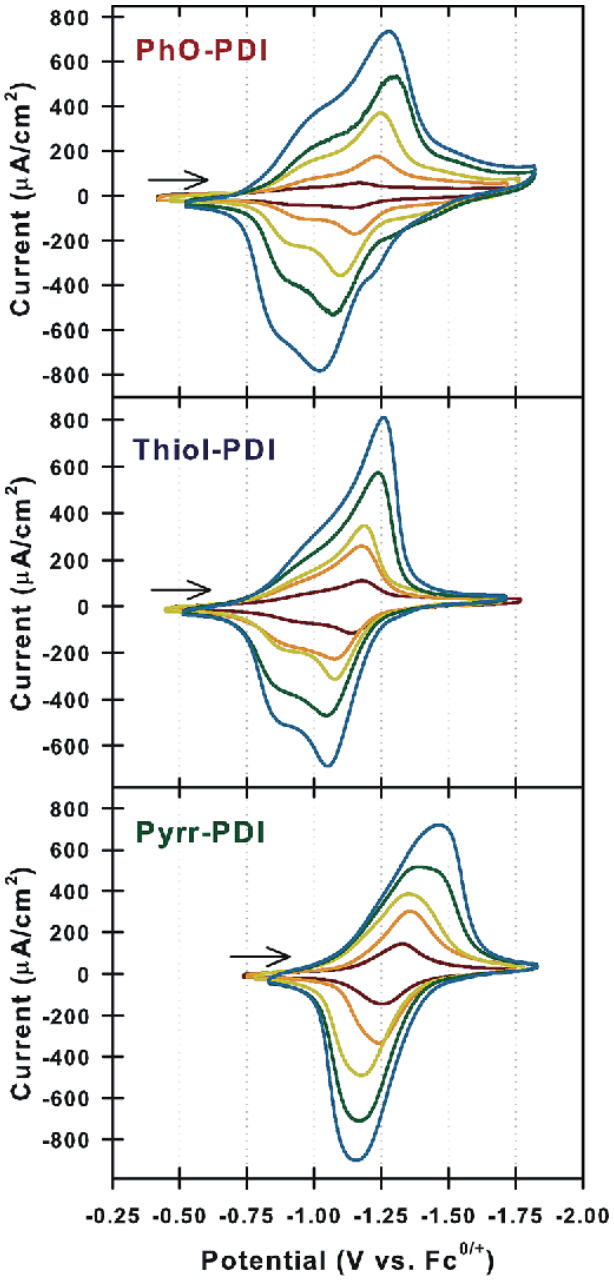

Figure 12. Cyclic voltammetry scans of one through five bilayers of PhOPDI (top), Thiol-PDI (middle) and Pyrr-PDI (bottom) assembled on an ITO electrode. CVs were obtained at scan rate of 1 V /s 1 with 0.1 M TBAP in anhydrous acetonitrile as the electrolyte. The arrow shows the initial scan direction, adapted from.[48]

1.4.6 Thesis Outline

Chapter 1 explored the need for new renewable energy technology to combat climate change and provide energy security for future populations. The new renewable energy technology proposed is the use of an arylene dye called perylene diimide which can be used in a variety of technologies including EC devices. Perylene diimides (PDIs) possess exceptional photophysical and photochemical properties[32] due to their unique structure and distinct locations for functionalization, the bay (1,6,7,12), ortho (2,5,8,11) and imide positions.[32,33,39] Past work in PDIs have functionalized three specific subtypes of propargyl PDIs with bay functionalizations of p-(t-butyl)phenol (PhO-PDI), dodecanethiol (Thio-PDI) and pyrrolidine (Pyrr-PDI). The PhO-PDI, Thio-PDI, and Pyrr-PDI can be grown in a bottom-up assembly method in conductive ITO surfaces through layer-by-layer (LbL) assembly using CuAAC click reactions to yield ordered, reproducible, and uniform films.[48] These films were tested to examine the reduction potentials, and all thin-films of Prgyl-PDIs (PhO-PDI, Thio-PDI, and Pyrr-PDI) can undergo two-electron reduction through cyclic voltammetry measurements. This thesis will further explore PDIs for utility as panchromatic assemblies of molecular multilayer thin-films.

Chapter 2 and 3 will explore the fundamental photophysical differences between derivatives of N,N'-dipropylphenyl-di(dodecylthio)perylene diimide. Taking inspiration from a select number of publications which described the isolation and comparison between the photo– and electrochemical properties of 1,6– and 1,7–PDI regioisomers with different substituents including phenoxy,[73] pyrrolidinyl,[72,73] piperidinyl,[74] aryl,[75] fluorenyl,[76] alkynyl,[77] alkyl,[77] and thioether.[78] We feel that we can add to this much larger body of knowledge with our derivatives of N,N'-dipropylphenyl-di(dodecylthio)perylene diimide, here to referred to as **1,6-**, **1,7-**, and **1,6,7-Thio-PDI**. Chapter 2 will focus on characterization of these Thio derivatives (**1,6-**, **1,7-**, and **1,6,7-Thio-PDI**) which have not been reported in literature. Chapter 3 will explore how different

derivatives of Thio-PDI exhibit different photophysical properties, for example, noticeably different electronic absorption and emission spectra. While these Thio-PDI derivative studies are not immediately useful for examination of PDIs within an EC device, understanding the varying photophysical properties between three derivatives provides more variability in selection of PDI chromophores utilized in emerging technologies such as dye sensitized cells (DSSCs) or organic photovoltaics (OPVs) and adds to a larger body of work on PDI derivatives and PDI regioisomers.

Chapter 4 will explore the utility of a phenoxy PDI (**PhO-Ph-PDI**) as an EC device through fabrication of five layers of **PhO-Ph-PDI** on a conductive ITO surface through layer-by-layer (LbL) assembly using CuAAC click reactions. This **PhO-Ph-PDI** will be studied as a type of panchromatic material for use in EC devices through a series of experiments. **PhO-Ph-PDI** was chemically reduced in THF using NaHg amalgam to provide a reference of neutral, singly reduced, and doubly reduced spectra which could be compared to the **PhO-Ph-PDI** thin film materials which is studied as an EC device. The chemical reduction of **PhO-Ph-PDI** will be compared to a series of **PhO-Ph-PDI** thin film experiments involving cyclic voltmammetry, spectroelectrochemical, and potential step spectroelectrochemical experiments. These experiments will examine the utility of **PhO-Ph-PDI** within an EC device, which should undergo a rapid and stable color change upon the reduction and oxidation of the **PhO-Ph-PDI** thin-film. Analysis of the **PhO-Ph-PDI** thin-film EC device provides another avenue for emerging research into EC devices which have been referenced to decrease energy consumption,[7,10,11] and potentially provide greater future energy stability.

2. SYNTHESIS, ISOLATION, AND CHARCTERIZATION OF THIO-PDI DERIVATIVES

2.1 Synthesis of 1,6-, 1,7-, and 1,6,7-Thio-PDI Derivatives

As previously mentioned, a select number of publications have described the isolation and comparison between the photo– and electrochemical properties of 1,6– and 1,7–PDI regioisomers with different substituents. These substituents include phenoxy,[122] pyrrolidinyl,[123] piperidinyl,[124] aryl,[80] fluorenyl,[76] alkynyl,[125] alkyl, [125] and thioether.[78] To add to this body of work we have synthesized two regioimers, **1,6-** and **1,7-Thio-PDI**, and one derivative, **1,6,7-Thio-PDI**.[126] For ease of understanding, all three Thio-PDIs will be refered to from here on in as, **1,6-**, **1,7-**, and **1,6,7-Thio-PDI** derivatives as shown in Figure 13.

2.1.1 Chemical Synthesis of 1,6-, 1,7-, and 1,6,7-Thio-PDI Derivatives

The **1,6-**, **1,7-**, and **1,6,7-Thio-PDI** derivatives were functionalized with a 1,6-diisopropylphenyl group and the bay position was functionalized with a dodecylthiol group. The added imide functionality of a 2,6-diisopropylphenyl was utlized to increase steric bulk on the PDI core which decreased π-π stacking by twisting the PDI core out of the plane.[39,60] The dodecylthiol functionality was utilized at the bay position as the addition of sulfur at this position is far less cited in literature relative to other atoms such as oxygen[48,122] and nitrogen.[123] Recall that functionalization of the bay position tunes the photophysics of the PDI due to the significant HOMO and LUMO coefficients at these positions.[127]

Portions of this chapter previously appeared from Riives, A. J.; Huang, Z.; Anderson, N. T.; Dinolfo, P. H. 1,7-, 1,6, and 1,6,7- Derivatives of Dodecylthio Perylene Diimides: Synthesis, Characterization, and Comparison of Electrochemical and Optical Properties. *J. Photochem. Photobiol. A Chem.* **2023**, *437*, 114441. https://doi.org/10.1016/J.JPHOTOCHEM.2022.114441.

General Methods and Materials. ^{1}H-NMR spectra were obtained on a Varian 500 MHz spectrometer and referenced to the solvent peak. LR and HR-ESI MS were obtained on a Thermo Electron Finnigan TSQ Quantum Ultra. Solvents, ACS grade or better, were purchased from Sigma Aldrich or Fischer Scientific and used as received unless specified otherwise. Brominated perylene-3,4,9,10-tetracarboxylic dianhydride (**Br-PTCDA**) was synthesized in a method similar what has previously been reported in literature[64,127] and was available from previous projects.[48]

Imidization of Br-PTCDA. A suspension of **Br-PTCDA** (2.0 g, ~3.64 mmol) was mixed with 2,6-diisopropylanaline (2.2 mL, 11.28 mmol) in propionic acid (40 mL) and refluxed at 140˚C under nitrogen for 10 h. The reaction progress was monitored by thin layer chromatography ($CHCl_3$ with 1% CH_3OH), and following completion of the reaction, the solvent was evaporated. The crude product was purified by silica–gel column chromatography using chloroform. At this point, thin layer chromatography showed spots that corresponded to **1,6–Br–PDI**, **1,7-Br-PDI**, and **1,6,7-Br-PDI**, but the derivatives were not resolved at this step. ^{1}H NMR in $CDCl_3$ was consistent with previous reports,[127] and revealed **1,6-Br-PDI**, **1,7-Br-PDI**, and **1,6,7-Br-PDI** isomers formed in a ratio of approximately 1:5:1. **1,6-Br-PDI** and **1,7-Br-PDI** LR-ESI m/z calculated for $C_{48}H_{41}Br_2N_2O_4$ $[MH]^+$ 867.14, found $[MH]^+$ 867.15; **1,6,7-Br-PDI** LR-ESI m/z calculated for $C_{48}H_{40}Br_3N_2O_4$ $[MH]^+$ 945.05, found $[MH]^+$ 947.06.

1,6-Thio–PDI, 1,7-Thio–PDI, and 1,6,7-Thio–PDI. A mixture of **Br–PDI** derivatives (577.0 mg, 0.664 mmol), dodecylthiol (0.746 mL, 3.11 mmol), NaOH (100 mg) where was added to 30 mL of pyridine and reflexed under nitrogen for 4 hours. The reaction mixture was poured into 200 ml of 10 % (v) HCl and was extracted with DCM and the organic layers dried with $NaSO_4$. Isomeric products were separated via flash silica–gel column chromatography involving a 1:1 mixture of

DCM and hexanes, and finally preparatory thin layer chromatography involving a 4:1 mixture of DCM and hexanes.

1,6-didodecylthio–N,N'–(2,4–diisopropylphenyl)-perylene diimide (1,6-Thiol-PDI): ^{1}H NMR (500mHz, $CDCl_3$): δ = 8.91 (d, *J* = 8.0 Hz, 2H), 8.86 (d, *J* = 8.0 Hz, 2H), 8.77 (s, 2H), 7.51 (m, 2H), 7.37 (d, *J* = 7.9 Hz, 4H), 3.25 (t, J =7.3, 2H), 2.78 (m, 4H), 2.68 (t, J = 7.5, 2H), 1.68 (m, 4H), 1.10-1.45 (m, 66 H). LR-ESI MS *m/z* calculated for $[MH]^+$ 1111.64, found $[MH]^+$ 1111.64. HR-ESI MS *m/z* calculated for $[MH]^+$ 1111.6434, found $[MH]^+$ 1111.6415 (1.7094 ppm).

1,7-didodecylthio–N,N'–(2,4–diisopropylphenyl)-perylenediimide (1,7-Thiol-PDI): ^{1}H NMR (500 mHz, $CDCl_3$): 8.94 (d, *J* = 8.0 Hz, 2H), 8.86 (s, 2H) 8.75 (d, *J* = 8.0 Hz, 2H), 7.51 (t, *J* = 7.6 Hz, 2H), 7.37 (d, *J* = 7.8 Hz, 4H), 3.26 (t, J = 7.4, 4H), 2.79 (m, 4H), 1.70 (m, 4H), 1.10-1.07 (m, 66 H). LR-ESI MS *m/z* calculated for $[MH]^+$ 1111.64, found $[MH]^+$ 1111.64. HR-ESI MS *m/z* calculated for $[MH]^+$ 1111.6434, found $[MH]^+$ 1111.6431 (1.5505 ppm).

1,6,7-tridodecylthio–N,N'–(2,4–diisopropylphenyl)-perylenediimide (1,6,7-Thiol-PDI): ^{1}H NMR (500 mHz, $CDCl_3$): 8.93 (d, *J* = 8.3 Hz, 1H), 8.85 (s, 1H). 8.77 (m, 3H), 7.51 (t, 2H, *J* = 8.0), 7.37 (d, *J* = 7.7 Hz, 4H), 3.36 (m, 1H), 3.07 (m, 5H), 2.795 (septet, 4H), 1.78-0.96 (m, 84 H), 0.86 (t, *J* = 7.0, 9H). LR-ESI MS *m/z* calculated for $[MH]^+$ 1311.80, found $[MH]^+$ 1311.80. HR-ESI MS *m/z* calculated for $[MH]^+$ 1311.8035, found $[MH]^+$ 1311.8013 (1.6439 ppm).

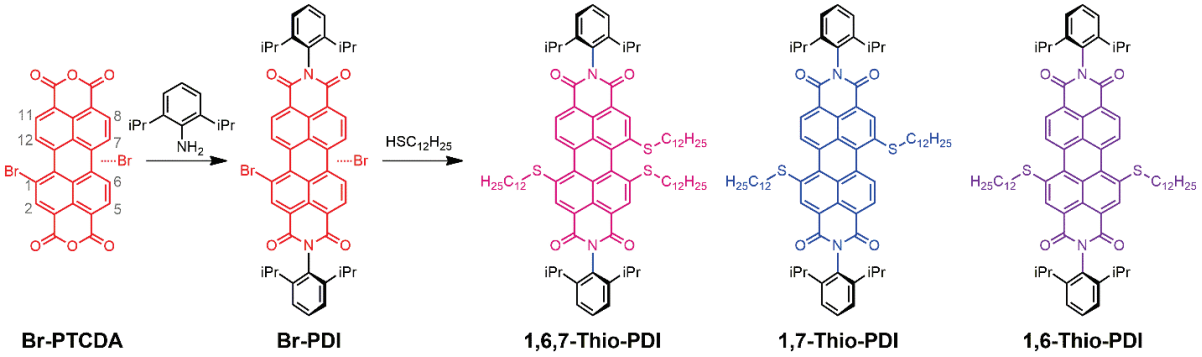

Figure 13. Synthesis of 1,6,7-Thio-PDI, 1,7-Thio-PDI, and 1,6-Thio-PDI, starting from Br–PTCDA, followed by imidization with diisopropylaniline, and finally substitution with dodecanethiol.

2.2 Characterization Analysis of 1,6-, 1,7-, and 1,6,7-Thio PDI Derivatives

2.2.1 NMR Analysis

The purity of the three Thio-PDI derivatives was confirmed by ^{1}H NMR spectra as shown in Figure 14. ^{1}H NMR is particularly useful in the analysis of different PDI isomers by comparing the signals within the 8.7 – 9.0 ppm range that corresponds to the perylene bay protons, and 7.2-7.6 ppm range for the diisopropylanaline additions at the imide positions. **1,7-Thio-PDI** is identifiable from the other isomers through a doublet-singlet-doublet (d–s–d) splitting pattern observed from 8.75 to 8.95 ppm. The two doublets correspond to the 5–H and 6–H positions and the singlet is assigned to 2–H next to the thio substitutions. The spectrum also shows well resolved peaks for the diisopropylaniline consistent with the C_2 symmetric structure. This d–s–d pattern for the perylene bay protons has been previously reported for a variety of 1,7-PDI isomers.[72,123,125] However, this is not the case for all varieties of PDI bay substituents as the addition of bulkier groups can shift the peaks, leading to a distortion in the expected d-s-d splitting pattern.[73,124,128,129]

The **1,6-Thio-PDI** shows a d–d–s pattern for the bay protons and a splitting of diisopropylanaline peaks due to the asymmetry of the molecule. The signals for the 7(12)–H and 8(11)–H protons at 8.9 ppm display the roofing effect as the coupling constant between two peaks (8 Hz) approaches the magnitude of the difference in chemical shifts (15 Hz). **1,6,7-Thio-PDI** shows two doublet peaks for the 11–H and 12–H and singlets for the remaining bay protons, consistent with the expected structure. The diisopropylaniline peaks also slightly broader, as comparted with the **1,7-Thio-PDI**, due to the asymmetry of the isomer. Compared to common 1,7-substituted PDIs, splitting patterns of 1,6-PDI and 1,6,7-PDI are not as often reported in literature, as these isomers are not as readily isolated due to their aforementioned likelihood to occur in much lower yields relative to the 1,7-PDI derivative.[72]

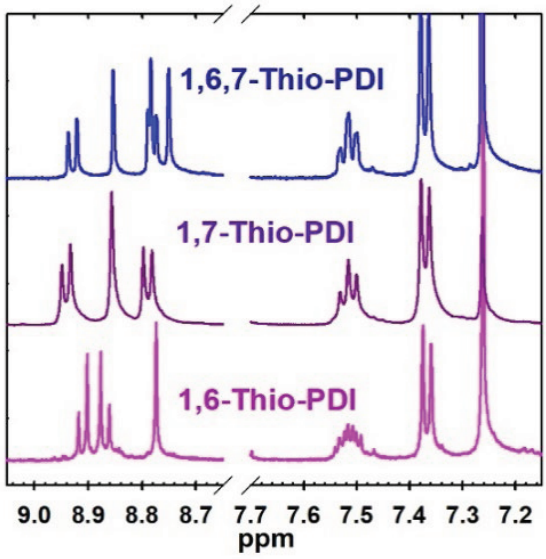

Figure 14. ^{1}H NMR of 1,6-Thio-PDI, 1,7-Thio-PDI, and 1,6,7-Thio-PDI in $CDCl_3$ highlighting the bay proton splitting pattern is located from around 8.7-9.0 ppm, and the diisopropyl proton splitting pattern is located from around 7.3-7.6 ppm. (spectra were referenced to the residual solvent peak $CHCl_3$ at 7.26 ppm.).

2.2.2 Mass Spectroscopy Analysis

Mass Spectroscopy Direct Infusion Electrospray Ionization (ESI) was utilized for further characterization of the **1,6-**, **1,7**, and **1,6,7-Thio-PDI** derivatives as shown in Figure 15, Figure 16, and Figure 17 respectively. The **1,6-Thio-PDI** produced a a *m/z* calculated for $[MH]^+$ 1111.64. HR-ESI MS *m/z* calculated for $[MH]^+$ 1111.6434, found $[MH]^+$ 1111.6415 (1.7094 ppm), **1,7-Thio-PDI** produced a *m/z* calculated for $[MH]^+$ 1111.64, found $[MH]^+$ 1111.64. HR-ESI MS *m/z* calculated for $[MH]^+$ 1111.6434, found $[MH]^+$ 1111.6431 (1.5505 ppm), and **1,6,7-Thio-PDI** calculated for $[MH]^+$ 1311.80, found $[MH]^+$ 1311.80. HR-ESI MS *m/z* calculated for $[MH]^+$ 1311.8035, found $[MH]^+$ 1311.8013 (1.6439 ppm). For the **1,6-Thio-PDI**, **1,7-Thio-PDI**, **1,6,7-Thio-PDI**, there is good agreement between the calculated values for the $[MH]^+$ and the found $[MH],^+$ pointing to successful synthesis of all Thio PDI derivatives.

Comparatively, mass spectroscopy ESI was also carried out on the **Br-PDI** sample which was reacted with deodecylthiol, and isolated to yeild the **1,6-Thio-PDI**, **1,7-Thio-PDI**, **1,6,7-Thio-PDI** derivatives. The **Br-PDI** contained a non-isolated mixture of **1,6–Br–PDI**, **1,7-Br-PDI**, and **1,6,7-Br-PDI**. The **1,6-Br-PDI** and **1,7-Br-PDI** LR-ESI m/z calculated for $C_{48}H_{41}Br_2N_2O_4$ $[MH]^+$ 867.14, found $[MH]^+$ 867.15, and the **1,6,7-Br-PDI** LR-ESI m/z calculated for $C_{48}H_{40}Br_3N_2O_4$ $[MH]^+$ 945.05, found $[MH]^+$ 947.06 as shown in Figure 18.

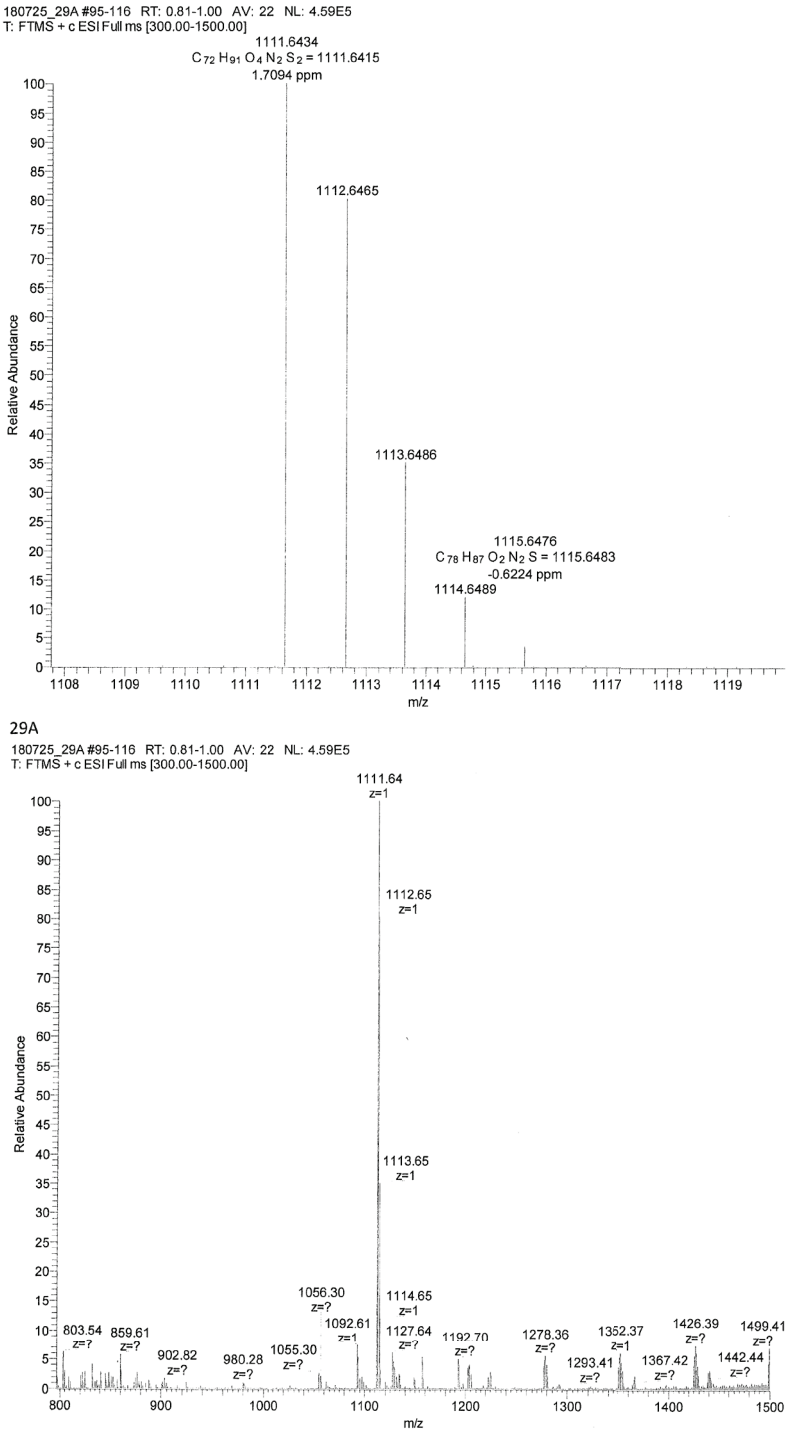

Figure 15. HR (top) and LR (bottom) mass spectra of 1,6-Thio-PDI using Direct Infusion Electrospray Ionization (ESI).

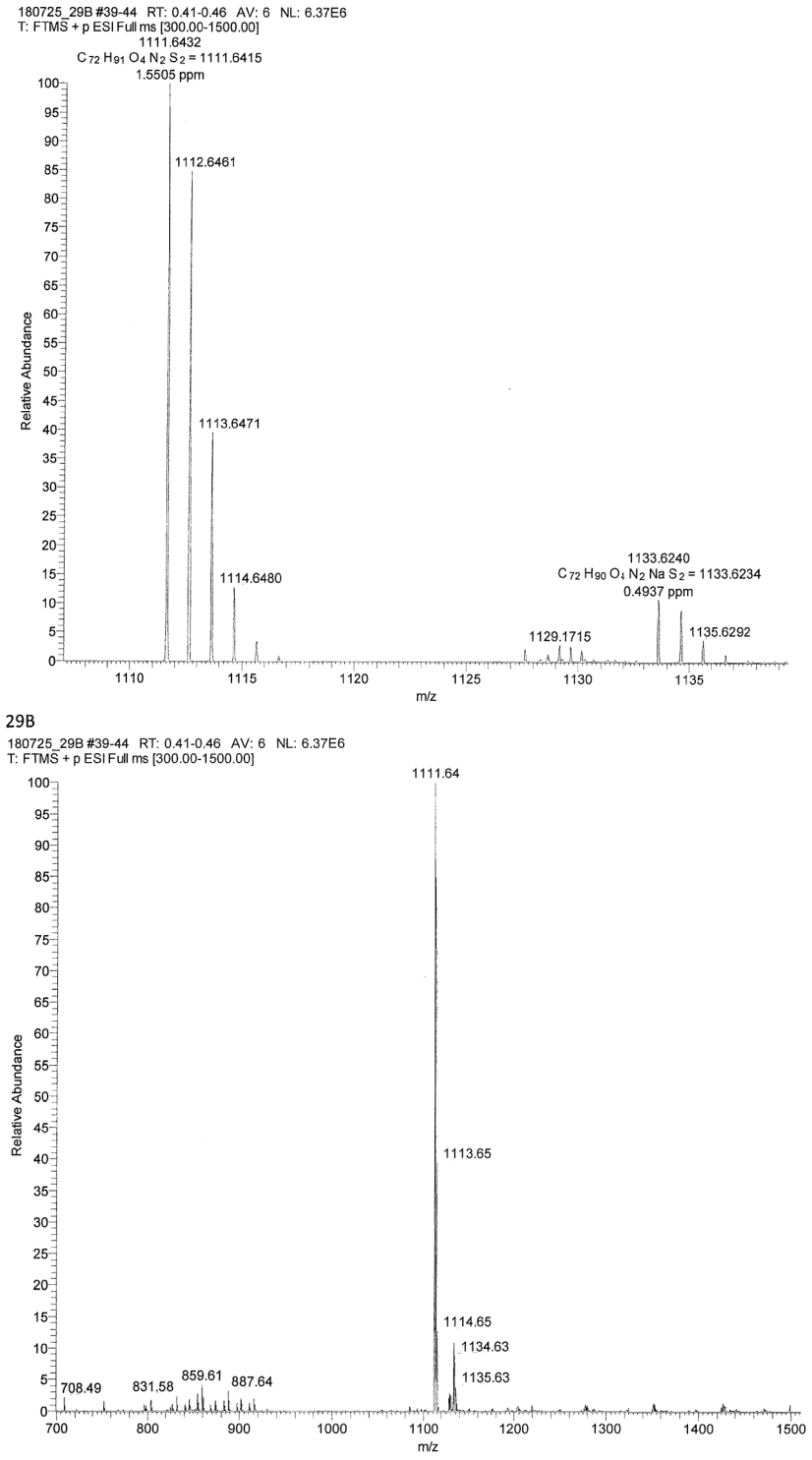

Figure 16. HR (top) and LR (bottom) 1,7-Thio-PDI (right) using Direct Infusion Electrospray Ionization (ESI).

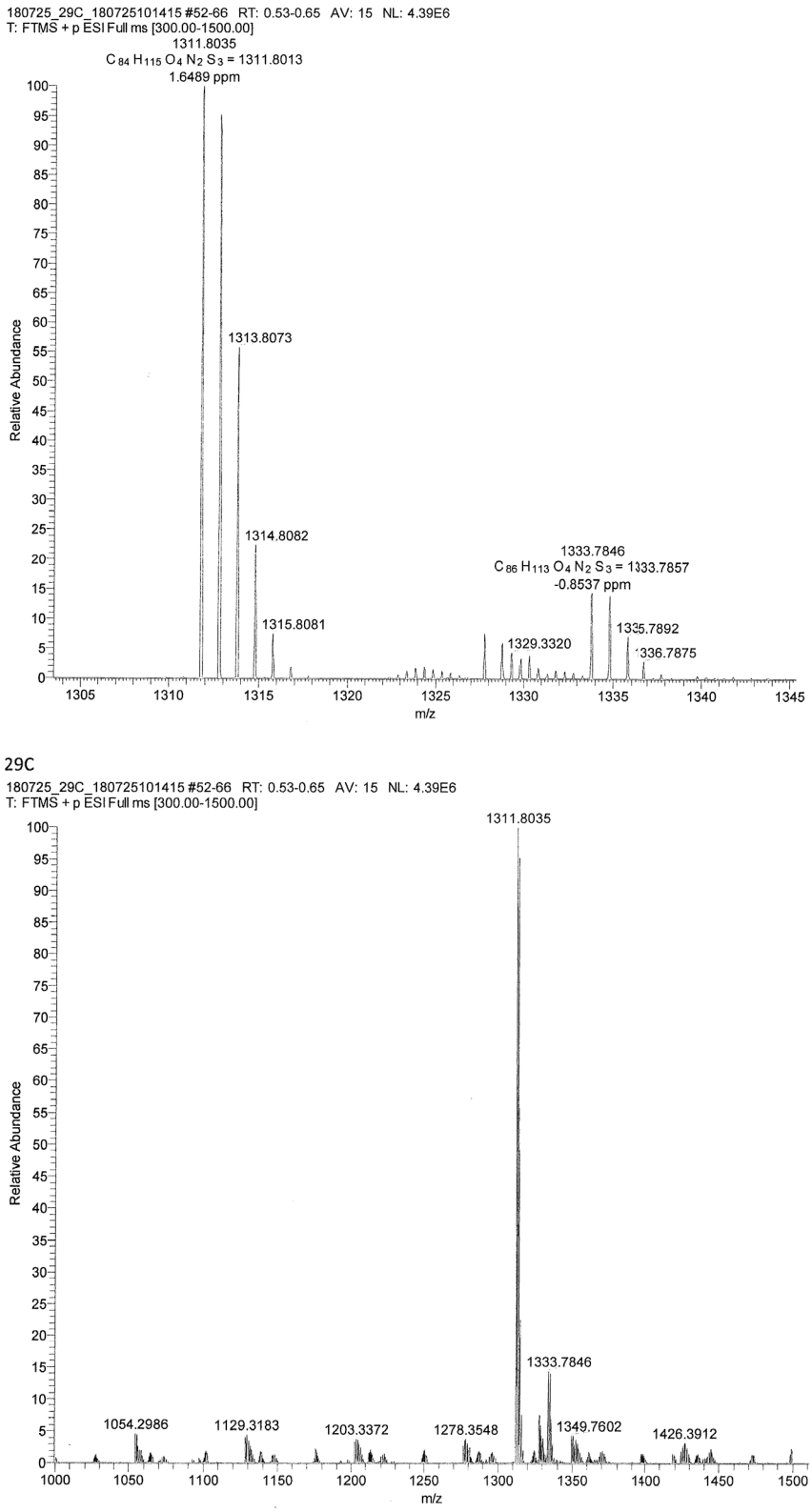

Figure 17. HR (top) and LR (bottom) mass spectra of 1,6,7-Thio-PDI using Direct Infusion Electrospray Ionization (ESI).

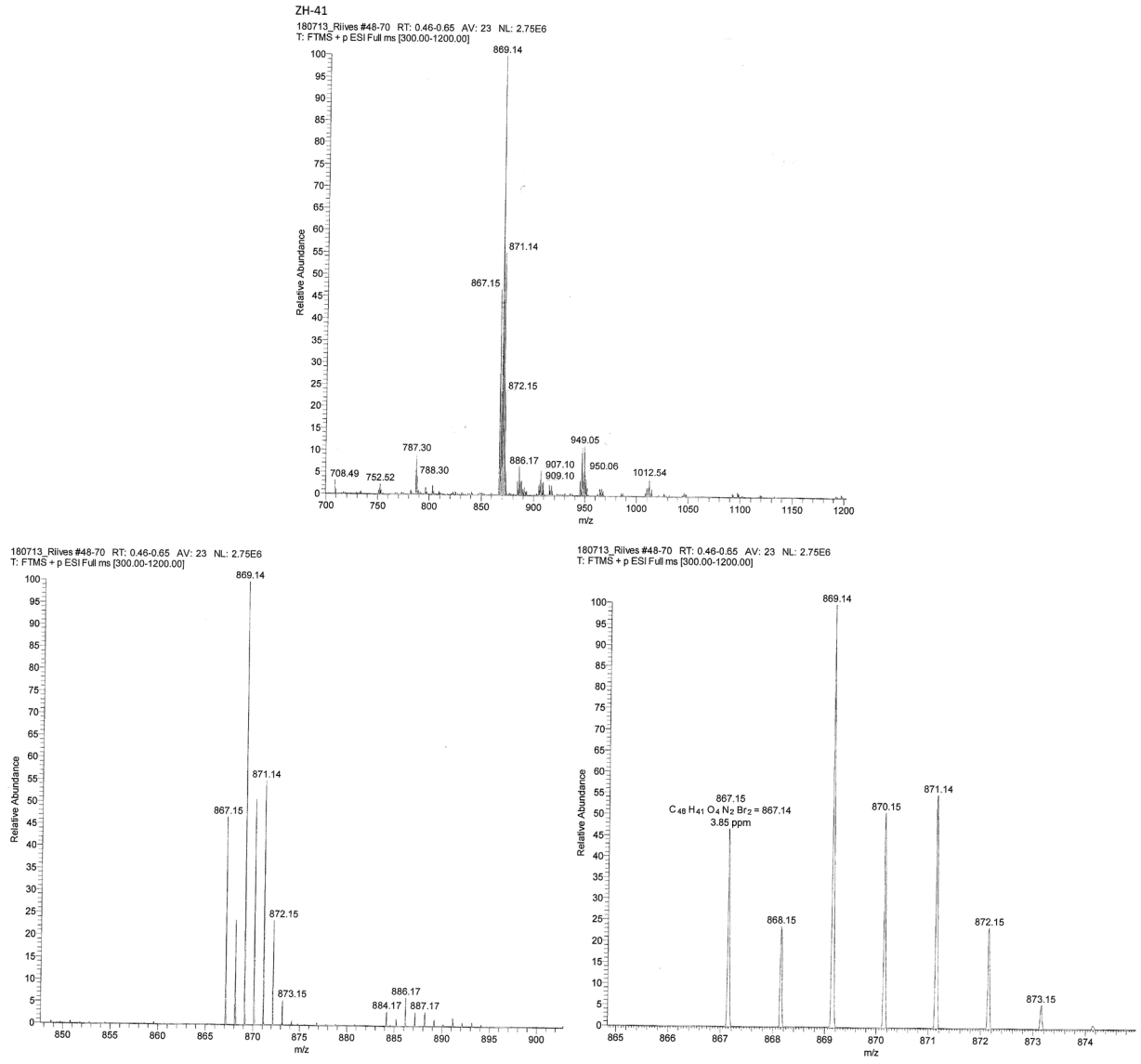

Figure 18. LR mass spectra using Direct Infusion Electrospray Ionization (ESI) Br-PDI showing a mixture of 1,6-Br-PDI (m/z = 867), 1,7-Br-PDI (m/z = 867), and 1,6,7-Br-PDI (m/z = 945).

2.3 Chapter Summary

In summary, two regioimers, **1,6-** and **1,7-Thio-PDI**, and one derivative, **1,6,7-Thio-PDI** were successfully synthesized by imidization of Br-PTCDA and subsequent substitution of bromine at the bay position with dodecylthiol. The imide functionality of a 2,6-diisopropylphenyl was utlized to increase solubility of the PDI in organic solvents on the PDI core,[39,69] and the bay

functionality of dodecylthiol was utilized as the addition of sulfur at this position is far less cited in literature relative to other atoms such as oxygen[48,122] and nitrogen. The **1,6-**, **1,7-**, and **1,6,7-Thio-PDI** derivatives were characterized by ^{1}H-NMR and low-resolution mass spectrometry. The ^{1}H-NMR showed distinctly different splitting patterns for the bay protons between **1,6-**, **1,7-**, and **1,6,7-Thio-PDI** derivatives. The **1,7-Thio-PDI** exhibited a d–s–d pattern for the perylene bay protons has been previously reported for a variety of 1,7-PDI isomers.[30,35,37] The ^{1}H-NMR bay proton splitting patterns for **1,6-** and **1,6,7-Thio-PDIs** are not as cited in literature, but are distinctly different between the derivatives. In addition to ^{1}H-NMR, low-resolution mass spectrometry was used to determine purity for the **1,6-**, **1,7-**, and **1,6,7-Thio-PDI** derivatives. Additionally, low-resolution mass spectrometry was used to determine the ratios of the **1,6–Br–PDI**, **1,7-Br-PDI** precursors relative to the **1,6,7-Br-PDI**. It was determined that the ratios were resolved as approximately 1:5:1 for **1,6–Br–PDI**, **1,7-Br-PDI** and **1,6,7-Br-PDI**[129] with the **1,7-Br-PDI** being the preferred product. Given the successful synthesis, isolation, and characterization of **1,6-**, **1,7-**, and **1,6,7-Thio-PDI**, photophysical and electrochemical analysis can commence.

3. PHOTOPHYSICAL AND ELECTROCHEMICAL ANALYSIS OF THIO-PDI DERIVATIVES

There are a small select number of publications in which 1,6- and 1,7-Thio-PDI regioisomers have been successfully isolated and characterized. These publications include 1,6- and 1,7- bay functionalized substituents with phenoxy,[73] pyrrolidinyl,[72,73] piperidinyl,[74] aryl,[75] fluorenyl,[76] alkynyl,[77] alkyl,[77] and thioether.[78] Of these publications, only a few have studied whether different PDI regioisomers have differing photophysical and electrochemical properties. PDI regioisomers with slightly differing electrochemical and spectroscopic properties may offer more specificity in designing systems for optoelectronic applications, light-harvesting systems, novel materials, photosynthetic devices and more.[73,75]Thus it is important to utilize only regioisomerically pure materials within these applications. In this chapter we will study whether 1,6-, 1,7-, and 1,6,7-Thio-PDI derivatives exhibit different photophysical electrochemical properties and compare any differences to what is available in literature for 1,6- and 1,7- PDI regioisomers.

Portions of this chapter previously appeared from Riives, A. J.; Huang, Z.; Anderson, N. T.; Dinolfo, P. H. 1,7-, 1,6, and 1,6,7- Derivatives of Dodecylthio Perylene Diimides: Synthesis, Characterization, and Comparison of Electrochemical and Optical Properties. *J. Photochem. Photobiol. A Chem.* **2023**, *437*, 114441. https://doi.org/10.1016/J.JPHOTOCHEM.2022.114441.

3.1 Experimental Setup for Studies of PDI Derivatives

3.1.1 Electronic Absorption and Emission Spectroscopy

Electronic absorption and Emission Spectroscopy. UV–Vis electronic absorption spectra were taken on a Perkin-Elmer Lambda 950 UV–vis spectrometer or an Agilent 8453A spectrometer running Olisworks software. Samples were background subtracted using a quartz cuvette. Steady–state fluorescence spectra were taken on Horiba Fluorolog-3 Model FL3-21. Solution fluorescence spectra were obtained at a right-angle detection. Fluorescence lifetimes were measured by phase modulated frequency-domain lifetime using a Horiba FluoroLog-Tau3 spectrometer. To remove stray light and fluorescence from other sources, a 600 nm long pass filter was used on the detector side. All solutions were purged with nitrogen gas to remove oxygen prior to steady-state and lifetime fluorescence measurements. A selection of phase-modulated data and fits are included in the Supporting Information.

3.1.2 Computational Details

Computational Details. Geometry optimizations for the Thio–PDI derivatives were carried out using density functional theory (DFT) as implemented in Gaussian09, revision D.01[130] at the Computational Center for Nanotechnology Innovations at Rensselaer Polytechnic Institute. The CAM–B3LYP functional[131] was used with the cc–pVTZ basis set for geometry optimizations in the gas phase, followed by optimizations that included the effect of solvation by THF using the self–consistent reaction field (SCRF) of polarizable continuum model (PCM)[132] approach. The resulting structures were confirmed as minima using frequency calculations at the same level of theory. Single point energy and TDDFT calculations were performed on the solvent-phase optimized structure at the CAM–B3LYP/may–cc–pVTZ/PCM(THF) level of theory.

3.1.3 Chemical Reductions

Chemical Reductions. Chemical reductions studies were carried out manner similar to a previous method,[133] using a quartz cuvette with the 1 cm optical path length. Samples were prepared in a N_2 purged glovebox in anhydrous THF. Chemical reduction was achieved by using small additions of Na(10%)–Hg with a slight excess of 18-crown-6 added to aid in the solubility of Na+ ions under air-free conditions. Clean conversion between the different redox states was confirmed by the appearance of isosbestic points.

3.2 Absorption

Figure 19 shows relative variation in perceived color of the three PDIs derivatives. These dramatic color ranges underscore how the number of bay substituents and symmetry can lead to variations in perceived color ranging from a dark magenta for **1,6,7-Thio-PDI**, to a violet purple for **1,7-Thio-PDI**, to purple for **1,6-Thio-PDI**. The normalized absorption and emission spectra of **1,6-Thio–PDI**, **1,7-Thio–PDI**, and **1,6,7-Thio-PDI,** recorded in range of solvents with varying polarity, is depicted in Figure 20. Both the docecylthio bay and diisopropylphenyl imide substituents aid in excellent solubility in the solvents used here and no evidence of aggregation was observed in the solvents employed here.

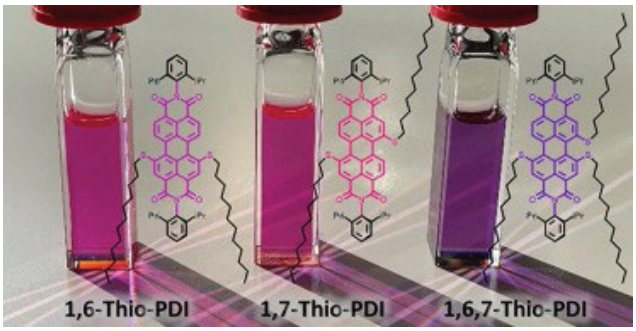

Figure 19. Visual representation of the perceived 1,6-, 1,7-, and 1,6,7-Thio-PDI in tetrahydrofuran.

The absorption spectra for each Thio-PDI derivative is dominated by intense, broad absorptions in the 500–600 nm range that are characteristic π-π^* transitions. Similar absorption profiles have been observed for other bis–thio substituted PDIs.[78] In toluene, the peak absorption for the S_0-S_1 transition for **1,6-Thio-PDI** occurs at 562 nm, 574 nm for **1,7-Thio-PDI**, and 584 nm for **1,6,7-Thio-PDI**. The absorption profile for **1,7-Thio-PDI** is the narrowest amongst the three derivatives and had a second prominent band at 425 nm. This second band is absent in **1,6-Thio-PDI** and **1,6,7-Thio-PDI**, or likely redshifted relative to **1,7-Thio-PDI** and overlapping S_0-S_1 transition as predicted by TD–DFT calculations (vide infra). The approximate 35 to 60 nm bathochromic shift of these PDIs as compared to unsubstituted versions suggests the thio groups are slightly more π-donating than phenoxy groups, but less than pyrrolidino.[60] Additionally, the broad nature of the absorption bands and lack of clear vibronic structure is consistent with a higher degree of twisting of the perylene core due to the larger sulfur groups.[78] DFT modeling of the isomers showed a noticeably larger twist angle of the perylene core for **1,6,7-Thio-PDI**, versus the other two (Table 1).

Previous reports comparing the absorption spectra of 1,6- and 1,7-PDI regioisomers have shown that depending on the electron donating or accepting ability of bay functionalization groups, absorption features vary between isomers. Dubey et al. isolated the 1,6- and 1,7- regioisomers of both phenoxy and pyrrolidino disubstituted PDIs.[73] In both cases, the 1,7– isomers showed a

narrower S_0-S_1 transition in the visible range and a second prominent band towards the UV. Similar to **1,6–Thio–PDI**, their 1,6– isomers lacked the distinct higher energy transition but showed broader visible bands. Similar trends were also observed for 1,6- and 1,7-fluorenyl disubstituted PDIs in a variety of solvents.[76]

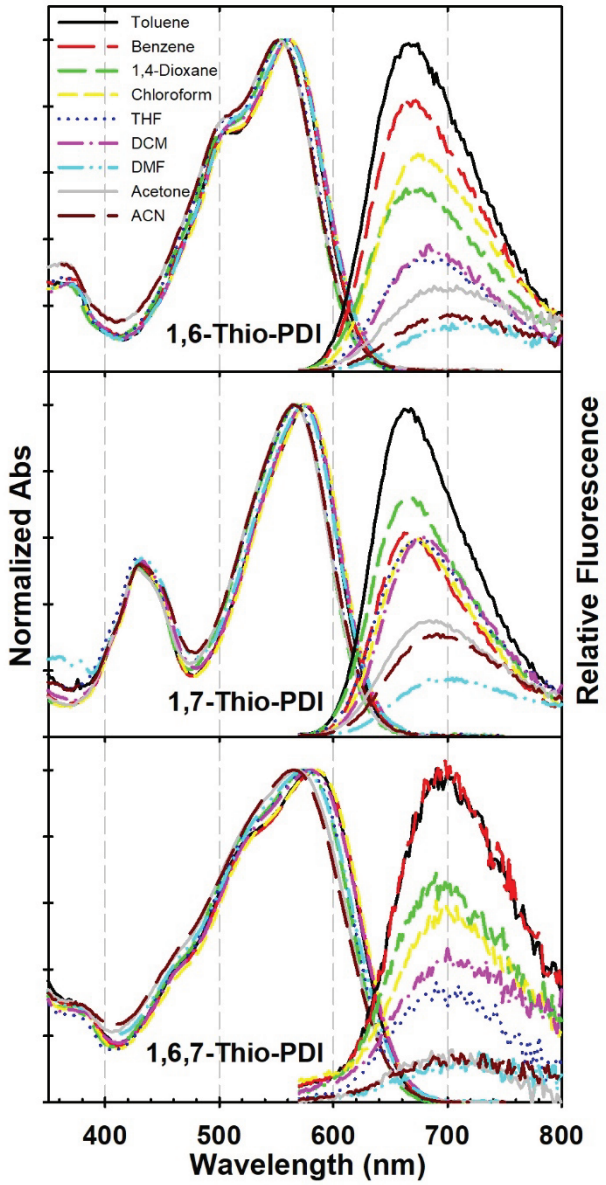

Figure 20. Normalized absorption and emission spectra for 1,6-Thio-PDI (top), 1,7-Thio-PDI (middle), and 1,6,7-Thio-PDI (bottom) in a range of solvents. Each emission spectra (ex 525nm) is scaled relative to the intensity of the sample taken in toluene.

3.3 Emission

The normalized fluorescence emission spectra of **1,6-Thio-PDI**, **1,7-Thio-PDI**, and **1,6,7-Thio-PDI** were recorded in solvents of varying polarity and are included in Figure 20. and the relevant parameters are summarized in Table 1. Each emission spectra are scaled relative to the intensity of the sample taken in toluene, which showed the highest intensity among all the solvents. The emission spectra for each derivative shows a broad, relatively featureless band, with peak maxima at 668 nm for **1,6-Thio-PDI**, 664 nm for **1,7-Thio-PDI**, and 696 nm for **1,6,7-Thio-PDI** in toluene. The Stokes shift also increases from 2,360 cm^{-1} for **1,7-Thio-PDI** to 2,780 cm^{-1} for **1,6,7-Thio-PDI**.

Table 1. Spectral parameters of 1,6-Thio-PDI, 1,7-Thio-PDI, and 1,6,7-Thio-PDI in toluene observed for all parameters such as lifetime (τ), quantum yield (Φ_F), absorbance and emission peaks, and the calculated Stokes shift in wavenumbers (cm^{-1}). The twist angle was calculated from DFT geometry optimized structures as the dihedral angle between the 6 and 7 (1 and 12) positions on the perylene core.

absorption and emission parameters for Thio-PDI Derivatives.							
Derivative	λ_{Abs} (nm, Tol)	λ_{Em} (nm, Tol)	Stokes (cm^{-1}, Tol)	Φ_F (Tol)	τ_F (Tol, ns)	τ_F (DMF, ns)	Twist angle (°)
1,6-Thio–PDI	562	668	2820	0.54 ± 0.01	6.3 ± 0.34	2.1 ± 0.12	22.5
1,7-Thio–PDI	574	664	2360	0.85 ± 0.02	8.1 ± 0.09	4.1 ± 0.34	22.1
1,6,7-Thio–PDI	582	696	2780	0.16 ± 0.01	4.4 ± 0.01	2.0 ± 0.11	23.2, 33.5

3.4 Quantum Yield

The fluorescence quantum yield, determined in toluene, was highest for **1,7-Thio-PDI** (Φ_F = 0.85), and decreased to 0.54 for **1,6-Thio-PDI** and 0.16 for **1,6,7-Thio-PDI**. These values are intermediate between those typically observed for phenoxy and amine substituted PDIs.[73] There are only a few reports comparing the quantum yield between 1,6– and 1,7–PDI regioisomers. Dubey et. al found a very small decrease in the quantum yield from a 1,7– to 1,6–regiosomers of a phenoxy PDI (0.97 to 0.96 in toluene), but a much larger difference for pyrrolidine substituents

(0.4 for 17, 0.7 for 16). [73] Dey et. al. found that the quantum yield for 1,7–diaryl–PDIs were generally larger than the 1,6– isomers.[80] The linear fits for the integrated fluorescence intensity vs. absorbance at excitation wavelength quantum yield are shown in Figure 21.

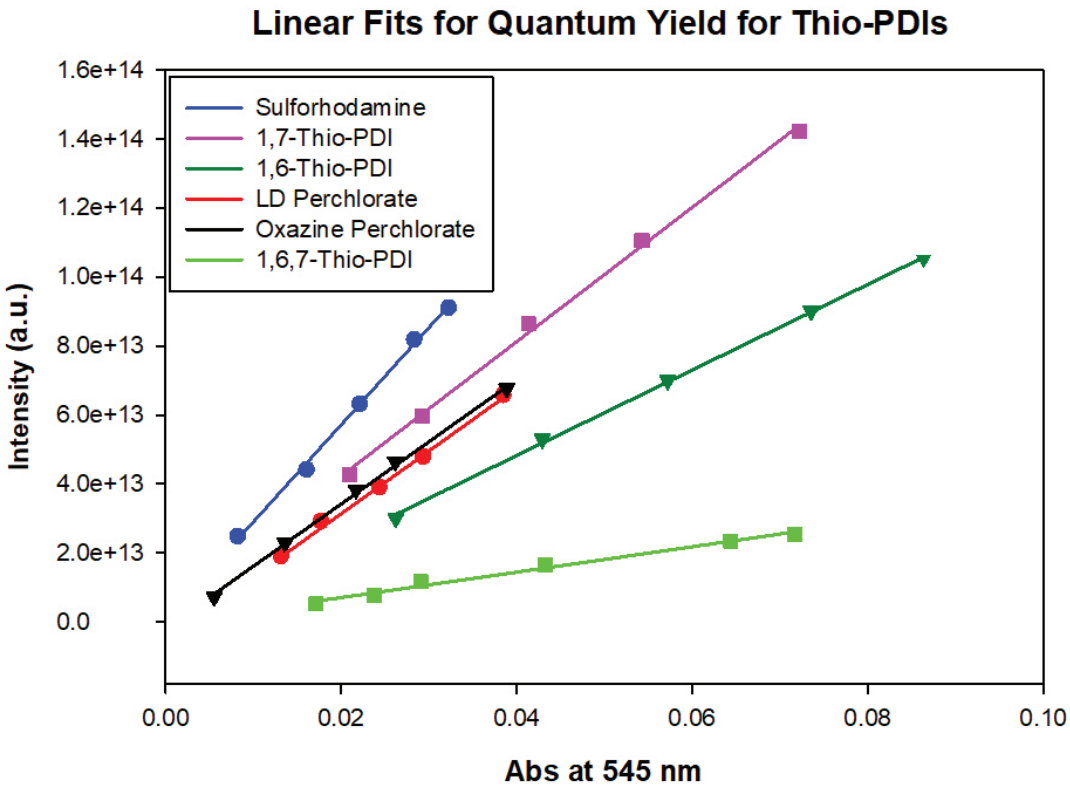

Figure 21. Quantum yield data for 1,6-Thio-PDI (Φ =0.54 ± 0.002), 1,7-Thio-PDI (Φ =0.85 ± 0.004), and 1,6,7-Thio-PDI (Φ =0.16 ± 0.001), along with the standards Rhodamine 101 (Φ =1.00), LD Perchlorate 690 (Φ =0.63), and Oxazine Perchlorate (Φ =0.63).[134,135]

3.5 Lifetime Measurements

The excited state lifetimes for the **1,6-**, **1,7-** and **1,6,7-Thio-PDI** were measured in toluene which gave the highest absorption intensity, and DMF which gave the lowest absorption intensity as shown in Figure 20, Figure 22, Figure 23, and Figure 24. For the **1,6-**, **1,7-**, and **1,6,7-Thio-PDIs**, the longest-lived excited state was observed in toluene, which gave excited state lifetimes of 6.3 ns ± 0.34, 8.1 ns ± 0.09, and 4.4 ns ± 0.01. The excited state lifetimes in DMF were far less

than those recorded in toluene. The excited state lifetimes for **1,6-**, **1,7-**, and **1,6,7-Thio-PDIs** in DMF were 2.1 ns ± 0.12, 4.1 ns ± 0.34, and 2.0 ns ± 0.11. Given the varying dielectric solvent parameters between toluene and DMF, namely the dipole moment, and the rate of relaxation from the ground to the excited states, the longer-lived excited states for toluene as compared to DMF correspond to what is expected. Interestingly, the difference between the excited state lifetimes between the **1,6-**, **1,7-**, and **1,6,7-Thio-PDI** derivatives requires additional spectroscopic techniques to probe the excited state dynamics between these derivatives.

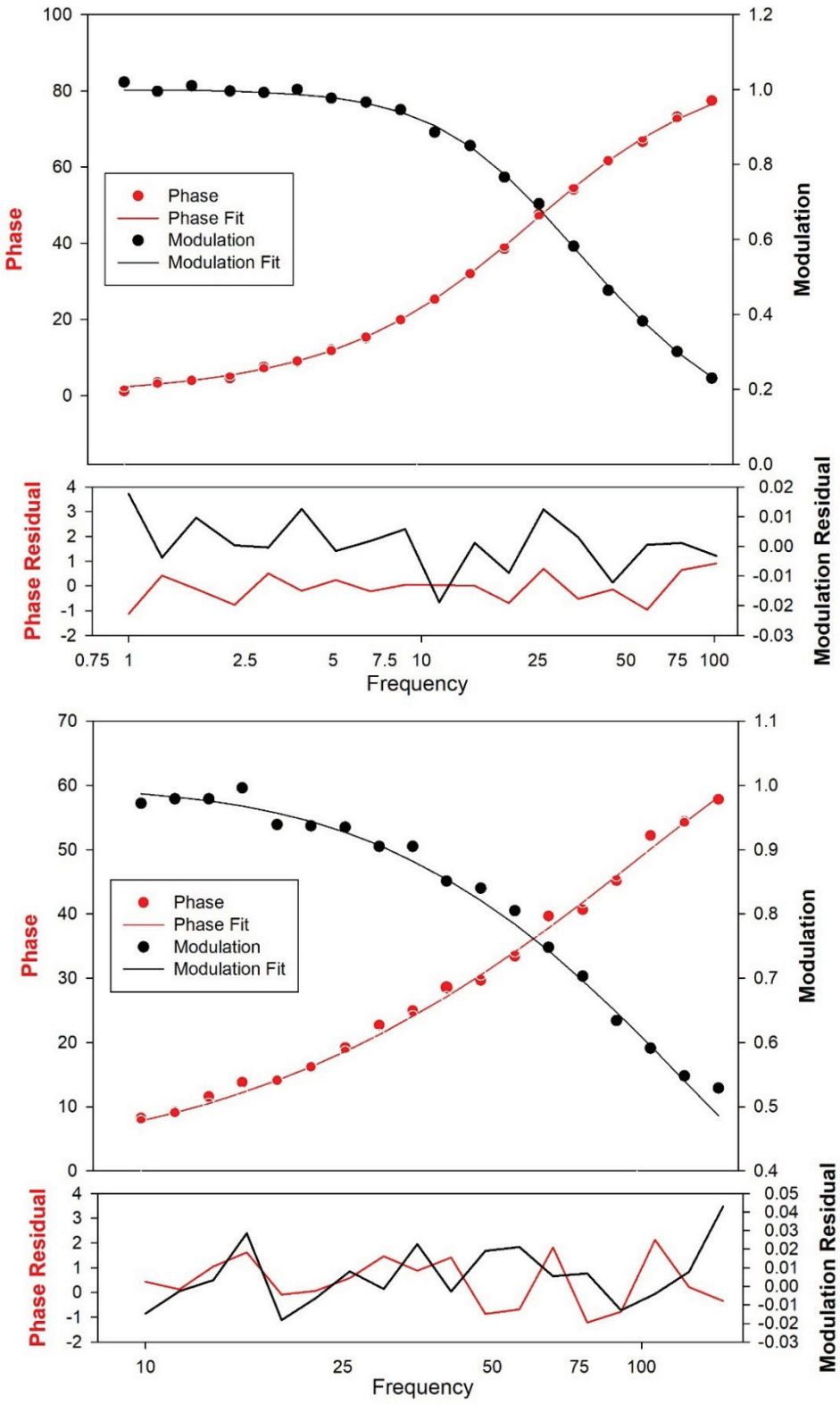

Figure 22. Representative frequency-domain fluorescence lifetime measurements of 1,6-ThioPDI in Toluene (top, lifetime = 6.6 ns, $\chi 2 = 0.9873$) and DMF (bottom, lifetime = 6.6 ns, $\chi 2 = 1.376$). Standard deviation parameters of dPhase = 0.5 and dMod = 0.01 were used to generate fit.

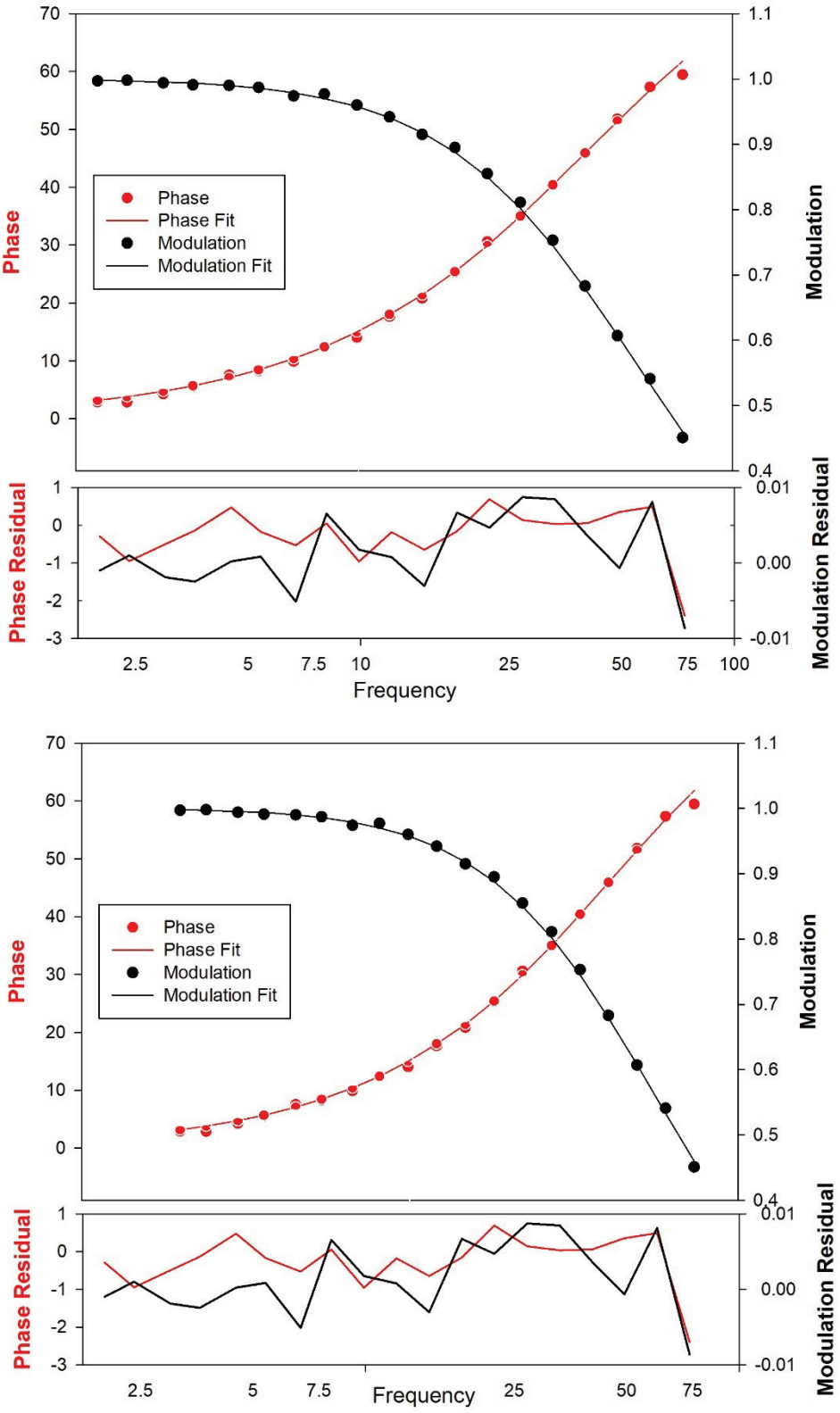

Figure 23. Representative frequency-domain fluorescence lifetime measurements of 1,7-ThioPDI in Toluene (top, Lifetime= 8.3 ns, $\chi 2$ = 0.6561) and DMF (bottom, Lifetime = 4.4 ns, $\chi 2$ =0.9834). Used standard deviation parameters of dPhase = 0.5 and dMod = 0.01 to generate fit.

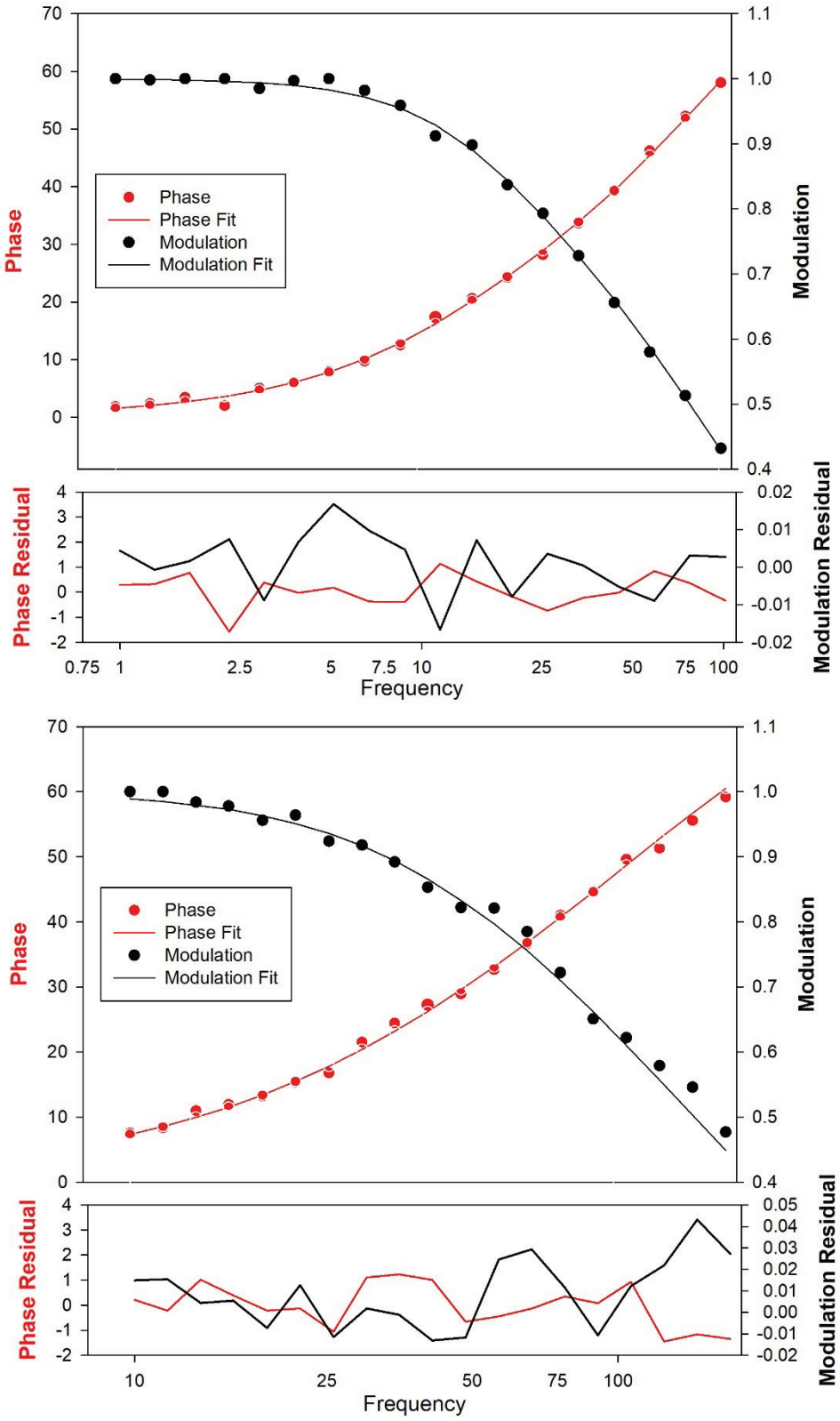

Figure 24. Representative frequency-domain fluorescence lifetime measurements of 1,6,7-ThioPDI in Toluene (Lifetime= 4.4 ns, $\chi 2$ = 0.918) and DMF (Lifetime = 2.0 ns, $\chi 2$ = 1.107). Used standard deviation parameters of dPhase = 0.5 and dMod = 0.01 to generate fit.

3.6 Lippert-Mataga Approximations

In order to gain further insight into the excited state properties of the different derivatives, the solvochromatic dependence of the absorption and emission spectra were analyzed by the Lippert-Mataga approximation to estimate the difference in dipole moment ($\Delta\mu$) between the ground (μ_g) and excited state (μ_e) via equation 1.[136] In the Lippert-Mataga approximation, the Stokes shift ($\overline{\boldsymbol{\upsilon}}_{\boldsymbol{a}} - \overline{\boldsymbol{\upsilon}}_{\boldsymbol{f}}$) of a fluorophore is proportional to the solvent orientation polarizability (Δf) which is determined from the solvent refractive index (n) and dielectric constant (ε). In equation 1, h and c have their usual meanings as Plank's constant and the speed of light, and a_o is the radius of the cavity in which the fluorophore resides.

$$\overline{\boldsymbol{\upsilon}}_{\boldsymbol{a}} - \overline{\boldsymbol{\upsilon}}_{\boldsymbol{f}} = \frac{2}{hca_o{}^3}\left(\frac{\epsilon-1}{2\epsilon+1} - \frac{n^2-1}{2n^2+1}\right)\left(\boldsymbol{\mu}_{\boldsymbol{e}} - \boldsymbol{\mu}_{\boldsymbol{g}}\right)^2 = \frac{2\Delta f}{hca_o{}^3}\boldsymbol{\Delta\mu}^2 \quad (1)$$

The Stokes shift for each of the isomers as a function of the solvent orientation polarizability (Δf) is shown in Figure 25. along with the linear regressions. The positive slope obtained for each of the derivative indicates that there is a larger excited state dipole moment than ground state dipole moment. [136] The resulting change in dipole moments for the three derivatives calculated from equation 1, and using a molecular radius estimated from DFT models (vide infra), are shown in Table 2. The slope of the solvent dependence for **1,6–Thio–PDI** is the largest relative to the other derivatives, predicting an 8.3 Debye the change in dipole moment. In comparison, the **1,7-Thio-PDI** and **1,6,7-Thio-PDI** exhibit similar, but smaller dipole moment changes of 7.2 and 7.1 Debye respectively. To the best of our knowledge, this is the first example comparing the change in dipole moment change of a tri-substituted PDI (**1,6,7-Thio-PDI**).

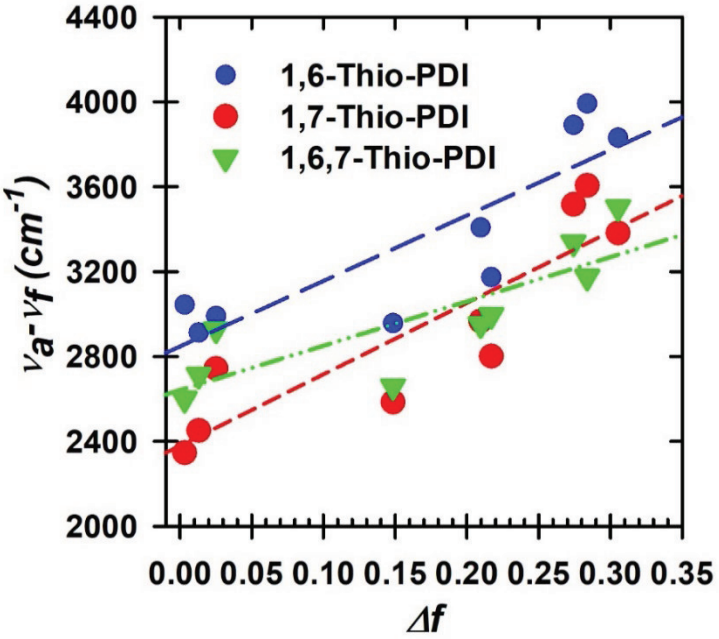

Figure 25. Comparison of the Stokes shift ($\bar{\upsilon}_a - \bar{\upsilon}_f$) derived from the absorption and emission properties, versus the solvent orientation polarizability (Δf) for the three isomers. The dashed lines represent the linear regression according to the Lippert–Mataga approximation utilizing equation 1. Data for 1,6-Thio-PDI is shown in blue, 1,7–Thio–PDI in red, and 1,6,7–Thio–PDI in green.

Table 2. Dipole moment changes derived by the Lippert–Mataga analysis.

Lippert–Mataga analysis	
PDI	**$\Delta\mu = \mu_e - \mu_g$ (Debye)**
1,6–Thio–PDI	8.3 ± 0.8
1,7–Thio–PDI	7.3 ± 0.7
1,6,7–Thio–PDI	7.1 ± 0.9

The change in dipole moments for these Thio–PDIs are comparable to others reported in the literature utilizing the Lippert-Mataga approximation where a comparison has been made between 1,6– and 1,7– regioisomers. A 1,6-difluorenyl-PDI, with swallowtail functionalities at the imide positions, exhibited a slightly larger dipole moment change of 9.64 D than the 1,7-regioisomer ($\Delta\mu$ = 8.65 D).[76] Similarly, a dialkylamino–substituted PDI, with cyclohexyl functionalities at the imide position, exhibited a larger change in dipole moment for the 1,6- (12.7 D) than the 1,7- PDI (7.9 D).[137] These trends were also observed for octyleamino–substituted PDIs.[138]

3.7 Density Functional Theory

Density functional theory (DFT) calculations were performed by Dr. Peter Dinolfo on the three Thio PDI derivatives to help understand any differences in excited state properties. The geometry of the derivativevs were optimized at the CAM-B3LYP/cc-pVTZ level using a polarized continuum model (PCM) with THF as the solvent. Finally, time dependent DFT (TDDFT) calculations were performed at the CAM-B3LYP/may-cc-pVTZ level, with a PCM solvation model for THF, to predict the electronic absorption spectra and change in dipole moments. CAM-B3LYP was chosen as the functional due to its ability to reasonably predict the charge transfer properties of electronic transitions and estimates for the dipole moments.[131]

The optimized structures for the three derivatives, and their frontier molecular orbitals, are shown in Figure 28. and the twist angles of the perylene cores are included in Table 1. The perylene core of **1,6-Thio–PDI** is twisted along the N,N' axis due to the presence of the bay thio groups, which extend to either side of the perylene plane. The slight asymmetry of substitution on one half of the perylene core results in a ground state dipole moment of 4.2 Debye oriented along the N,N' axis, from the thio–functionalized side towards the unfunctionalized end. The perylene core of **1,7-Thio–PDI** is also twisted, however the thioether groups now point towards one face of the perylene. This results in a dipole moment of 2.8 Debye oriented towards the thioether side, normal to the plane of the perylene core. The perylene core of **1,6,7-Thio–PDI** derivative shows the greatest degree of twist due to the proximity of the thioether groups at the 6 and 7 positions. This derivative has a 3.8 Debye dipole moment that nearly normal to the plane of the perylene, but tilted slight towards the 6,7– positions.

The frontier molecular orbital diagrams are shown in Figure 26. and are consistent with typical DFT calculations of PDIs, with π delocalization across the core and lack of orbital density at the imide nitrogens. Figure 27. shows a plot of the energetic levels of the frontier molecular

orbitals for the three Thio–PDIs. Figure 28. shows the predicted electronic absorption spectra of the three isomers from TDDFT calculations. The TDDFT results qualitatively reproduce the visible absorption spectra of each of the isomers and help understand the differences between them. All three spectra are dominated by a singlet π–π^* transition ($S_0 \rightarrow S_1$), in the 500 nm range, which are associate primarily with the HOMO and LUMO orbitals shown in Figure 26. and Table 3. The HOMO of both **1,6-Thio–PDI** and **1,7-Thio–PDI** contain significant contribution from the sulfur atoms, which is absent in the LUMOs. This suggests there is a small amount of charge transfer from the sulfur atoms of the thioether groups towards the perylene core and is consistent with the change in dipole moments estimated from the Lippert–Mataga approximation. The HOMO of **1,6,7-Thio–PDI** only has significant contribution from the sulfur thio group in the 1 position. The twisting of the thio groups in the 6– and 7– positions, due to steric constrains, likely diminishes their sulfur orbital contribution to the HOMO.

The TDDFT results predict the $S_0 \rightarrow S_2$ transition for **1,6–Thio–PDI** and **1,6,7–Thio–PDI** in the 420 nm range. These transitions overlap with the $S_0 \rightarrow S_1$ states and likely explain the broader absorption features seen in Figure 28. The $S_0 \rightarrow S_2$ transition for **1,7–Thio–PDI** is predicted to be at 360 nm for the 1,7– derivative and is consistent with the second higher energy absorption feature around 400 nm as seen in, as well as the narrower absorption band at 560 nm.

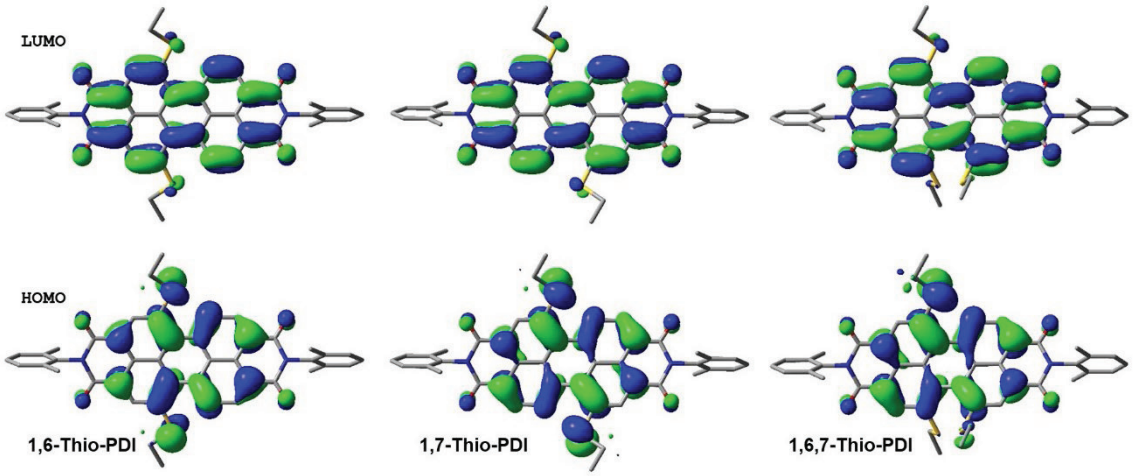

Figure 26. Optimized molecular structures and frontier molecular orbitals for the three isomers, 1,6-Thio-PDI (left), 1,7-Thio-PDI (center), and 1,6,7-Thio-PDI (right). The highest occupied (HOMO) and lowest unoccupied molecular orbitals (LUMO) are shown on the bottom and top respectively.

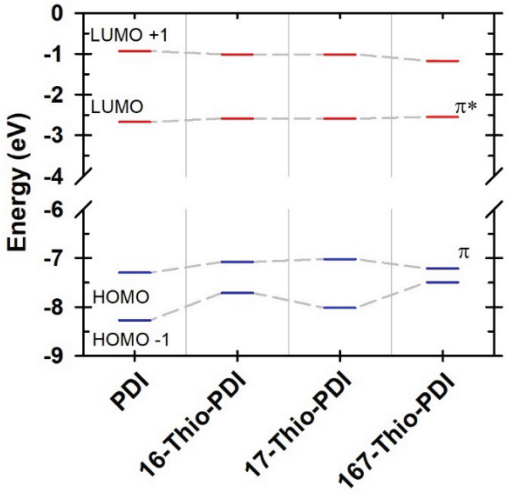

Figure 27. Comparison of the energetic levels of the frontier molecular orbitals of PDI, 1,6-Thio-PDI, 1,7–Thio–PDI, and 1,6,7–Thio–PDI calculated at the CAM–B3LYP/may-cc-pVTZ level, with PCM solvation for THF.

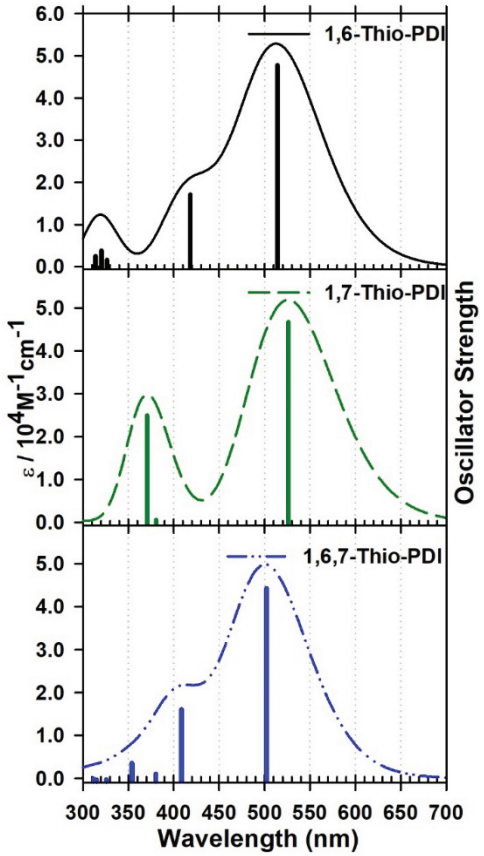

Figure 28. Predicted electronic absorption spectra of 1,6-Thio-PDI (top), 1,7-Thio-PDI (middle), and 1,6,7-Thio-PDI (bottom) from TDDFT calculations at the CAM–B3LYP/may–cc–pVTZ/PCM(THF) level of theory. The simulated absorption spectra were generated using a 2000 cm^{-1} bandwidth for all peaks. The solid vertical lines correspond to the oscillator strengths of the calculated singlet transitions.

Table 3. Lowest-lying singlet excited states calculated for 1,6-Thio-PDI, 1,7–Thio–PDI and 1,6,7–Thio–PDI at the CAM–B3LYP/may-cc-pVTZ level, with PCM solvation for THF. Vertical excitation energies (E), oscillator strengths (f), and dominant monoexcitations with contributions (weights) greater than 10% are indicated.

Lowest-lying singlet excited states calculated for Thio-PDI derivatives				
PDI	State	E eV (nm)	*f*	Description
	S_1	2.41 (514)	0.9603	HOMO → LUMO (97.7)
1,6-Thio–PDI	S_2	2.97 (418)	0.3569	HOMO (-1) → LUMO (92.5)
	S_1	2.36 (526)	0.9540	HOMO → LUMO (97.6)
1,7-Thio–PDI	S_2	3.26 (380)	0.0319	HOMO (-1) → LUMO (89.0)
	S_1	2.47 (502)	0.9067	HOMO →LUMO (97.5)
1,6,7-Thio-PDI	S_2	3.04 (408)	0.3430	HOMO (-1) → LUMO (92.4)

3.8 Electrochemical Measurements

The electrochemical properties of the different derivatives were determined by cyclic voltammetry (CV) in tetrahydrofuran. All three Thio-PDIs undergo two electrochemically reversible reductions in the range -1 to -1.4 V vs ferrocene/ferrocinium as shown in Table 4. and Figure 29. There are some subtle shifts in the potentials between derivatives, but the reductions follow trends reported for other PDI compounds.[33,51,139–141] All three Thio–PDIs show a separation of approximately 330 mV between the $E_{½}^{0/-1}$ and $E_{½}^{-1/-2}$ values.

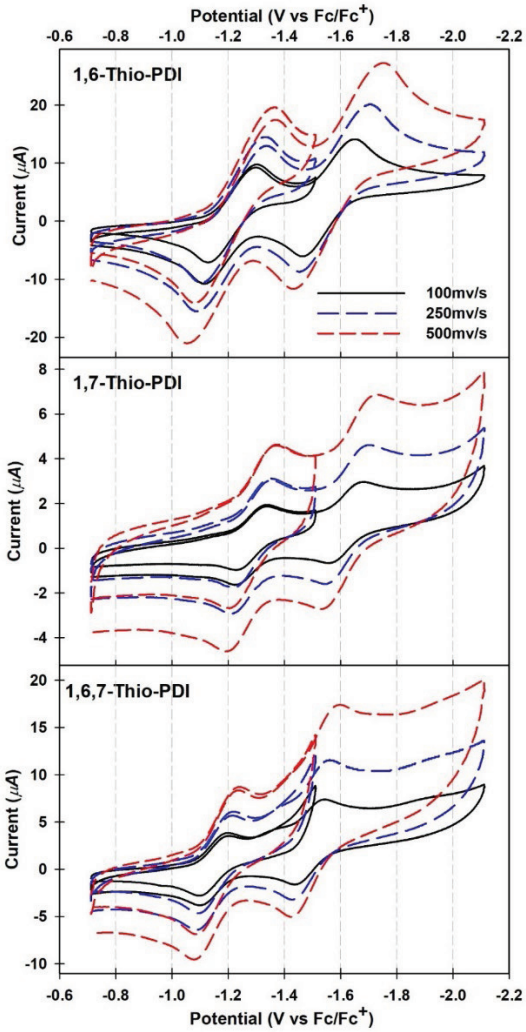

Figure 29. Cyclic Voltammetry (CV) scans for 1,6-Thio-PDI (top), 1,7-Thio-PDI (middle), and 1,6,7-Thio-PDI (bottom) at varying scan rates (0.10 V/s, 0.25 V/s, and 0.50V/s) to show the first and second reductions. CVs were obtained in 0.1 M of $TBAPF_6$ in anhydrous tetrahydrofuran as the electrolyte.

Table 4. Electrochemical parameters for 1,6-, 1,7-, and 1,6,7-Thio-PDI derivatives.

Electrochemical Parameters for Thio-PDI Derivatives[a]		
	$E_{½}^{0/-1}$	$E_{½}^{-1/-2}$
1,6-Thio-PDI	-1.21	-1.56
1,7-Thio-PDI	-1.28	-1.62
1,6,7-Thio-PDI	-1.15	-1.49
[a] V vs $Fc^{0/+}$		

3.9 Chemical Reductions and CIE

PDIs are known to produce anionic and dianonic redox states with vastly different electronic absorption spectra.[78,142,143] In order to determine the absorption spectra of the different Thio–PDI derivatives, in situ chemical reduction with Na(Hg), in the presence of 18–crown–6, was employed to produce the singly and doubly reduced states. These conditions allowed for the clean conversion between redox states of the Thio–PDIs. The absorption spectra of the Thio-PDIs in THF and the corresponding visual color changes are shown in Figure 30. The absorbance peaks of the neutral, singly reduced, and doubly reduced states follow a similar trend for all three Thio-PDIs and are consistent with previously reported 1,6– and 1,7–diadamantylthio–PDIs.[78]

The absorbance spectra for neutral complexes in THF are dominated by the broad peaks in the 500–600 nm range, resulting in an intense magenta to purple color. Reduction of the Thio–PDIs to the singly reduced state results in a significant red–shift of the main absorption bands to approximately 750 nm and increase in absorptivity. Additional lower intensity bands are also present from 800–1000 nm. Further reduction to the doubly reduced state results in a significant blue shift of the main absorption band back to the visible region, between 575–625 nm.

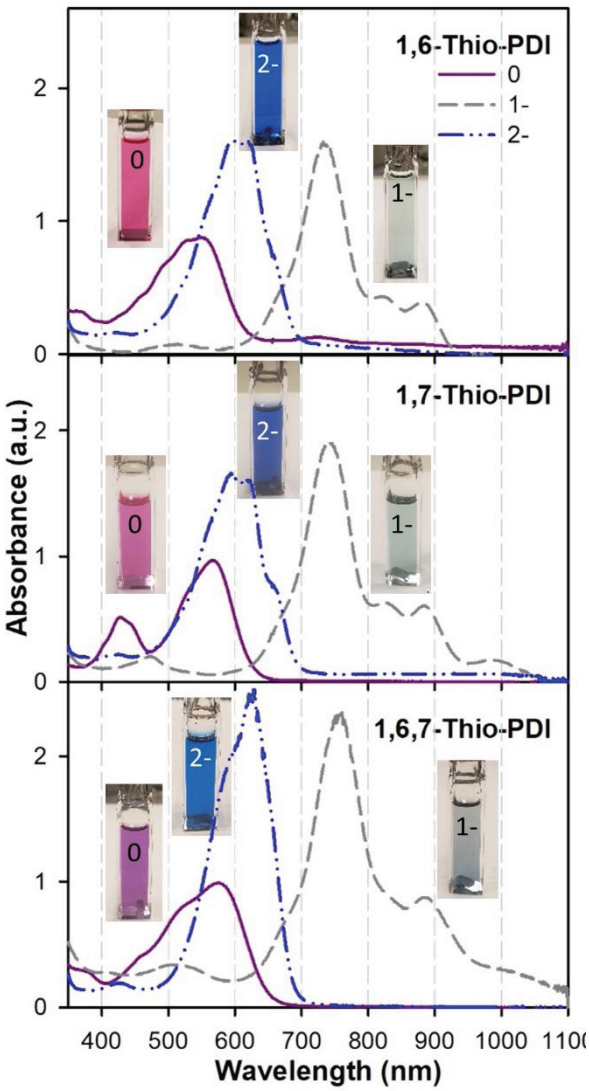

Figure 30. UV−Vis–NIR absorption spectra of 1,6-Thio-PDI (top), 1,7-Thio-PDI (middle) and 1,6,7-Thio-PDI (bottom) recorded in THF with 0.01 M 18-crown-6. The singly and doubly reduced states were generated by chemical reduction using Na(Hg). The spectra of neutral states are shown as solid purple line, the singly reduced states as dashed grey lines, and the doubly reduced states as a dashed–dotted blue line. Included with the spectra are images of the cuvettes corresponding to the sample spectra.

In addition to the absorption spectra, Figure 30. also includes photographs of the samples, taken during the reduction process, highlighting the perceptible color changes of the Thio-PDIs between the neutral, singly reduced, and doubly reduced states. While there were some slight variations in perceivable color across the different Thio-PDIs redox states, similar trends were observed. The neutral state for all isomers shows a pink to purple color, the singly reduced state is light green or blue, and the doubly reduced state is dark blue. These color changes for the **1,6-**,

1,7-, and **1,6,7-Thio-PDI** correspond to what has been previous cited in literature in for 1,6- and 1,7- bay substituted adamantylthio derivatives in which distinct visual color changes were observed for 1,6- and 1,7- with the doubly reduced state being a dark blue, which is similar to the doubly reduced Thio-PDIs.[78] Figure 31. shows the CIE (Commission Internationale de l'Eclairage) 1931 xy chromaticity diagram with the values calculated for each of the three Thio–PDI's in the neutral, singly, and doubly reduced states. As expected, based on the similarities of images shown in Figure 30, the xy chromaticity values for the specific redox states are grouped together. The large difference in color between redox states highlights their potential use in electrochromic materials.

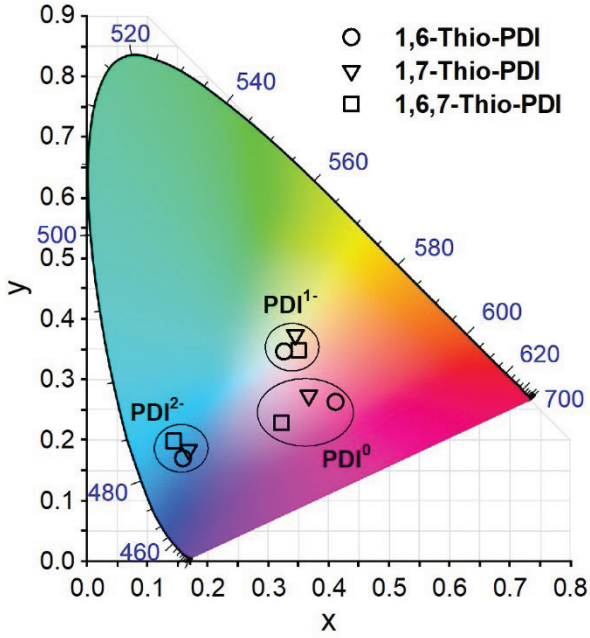

Figure 31. CIE 1931 xy chromaticity diagram with points calculated for the neutral, singly and doubly reduced forms of the Thio–PDIs.

3.10 Chapter Summary

There are significant differences in the absorption and emission spectra, the quantum yield, the excited state lifetimes, Lippert-Mataga and DFT excited state dipole moment between the derivatives of **1,6-**, **1,7-** and **1,6,7-Thio-PDI**. Thus, there are clear indications that a change in the location of a functional group within the bay position of the PDI moiety has some, if not, significant effect on the photophysical properties of the PDI. Additionally, there are differences between the oxidation and reduction waves between the Thio-PDIs which all exhibit a reversible wave. This ability to reduce each PDI is also observed with the chemical reductions in which the **1,6-**, **1,7-** and **1,6,7-Thio-PDI** all achieve distinct coloration and show distinct corresponding peaks which are similarly calculated with the CIE model. Thus, the **1,6-**, **1,7-** and **1,6,7-Thio-PDI** all exhibit different photophysical properties and simultaneously exhibit distinct coloration which may have potential to add additional specificity to organic photovoltaic devices as well as in electrochromic devices.

4. PERYLENE DIIMIDE MULTILAYER ASSEMBLIES IN ELECTROCHROMIC MATERIALS

Perylene diimides (PDIs) are promising materials for EC devices because they exhibit strong color, thermal stability, a high molar absorption coefficient, and they propensity to self-assemble. Additionally, PDIs have high electron affinity due to the carbonyl groups on the PDI moiety. This electron affinity allows for the PDI moiety to be easily reduced and form stable radical anions and dianions.[33,71,78,144–151] The reduction to produce radical anions and dianions can occur through chemical, electrochemical, and photochemical processes.[139,152]

However, as previously discussed, small organic redox dyes like PDIs can exhibit intense coloration but their small size and small corresponding weight can lead to stability issues in EC devices.[31] Keeping in mind the strengths and potential limitations of PDIs within EC devices, in this portion of the manuscript we will fabricate an EC device through the CuAAC click reactions linking together five layers of a phenoxy PDI (**PhO-Ph-PDI**) onto a conductive surface ITO surface to form a **PhO-Ph-PDI** thin-film. This **PhO-Ph-PDI** thin-film should act as an EC material given previous work in which PDIs are known for their high tinctorial strength,[34] their ability to exhibit different colors from the neutral to reduced states as shown in chemical reduction of the Thio-PDIs, and undergo two electrochemically reversible reductions.[126]

4.1 General Preparation and Synthesis of Layers and Linkers for Multilayer Assembly

Fabrication of the **PhO-Ph-PDI** thin-film EC device requires special consideration of the material which will be reduced and oxidized to form distinct colors. For simplicity, when referring to CuAAC click reactions, the **PhO-Ph-PDI** terminal alkyne linkages will be referred to as the layer within the thin film. Given that the CuAAC require both a terminal alkyne and azide to form the five membered triazole which clicks together both components, the azide used to covalently link together two different layers of **PhO-Ph-PDI** will be refer to as the linker.

4.1.1 Selection of Layer and Linker in Multilayer Assembly

The perylene diimide (PDI) p-(t-butyl)phenol with phenylacetylene imide functionality (**PhO-Ph-PDI**) was synthesized for the multilayer fabrication of the **PhO-Ph-PDI** thin-film EC material. **PhO-Ph-PDI** was previously synthesized by former graduate students in the Dinolfo group, Guangyu Hu and Dr. Peter Palomaki. [81,153] As previously discussed, the **PhO-Ph-PDI** layer is clicked to the **N_3Mest** linker through CuAAC click reactions. This CuAAC click reaction between the layer and linker was previously shown in Figure 10. with the multilayer assembly shown in Figure 11. However, unlike the propargyl imide functionality shown in Figure 11., the phenylacetylene imide functionality was selected for use in **PhO-Ph-PDI**, as Guangyu Hu, determined that the phenylacetylene imide functionality affects the multilayer growth through aggregation.[153] The rigid phenylacetylene imide functionality tends to promote the formation of H-type aggregates, whereas the less rigid propargyl imide functionality tends to promote J-type aggregates. H-type aggregates allow for a more upright structure within the multilayer assembly, and J-type aggregates lead to more of a tilting structure as shown in Figure 32. J-type aggregates

are preferred over H-type aggregates for use in electrochromic materials as a the less upright multilayer assembly can allow for better penetration of electrolyte through the thin-film assembly to conductive surface. Better penetration of electrolyte should aid for the entire thin-film to be reduced to different states, and ideally different colors, which is an essential feature of an electrochromic material.

The synthesis of **PhO-Ph-PDI** is shown in Figure 33. was carried out with no isolation of pure products between each synthetic step owing to the insolubility of PDIs in solution due to π-π stacking. As previously mentioned, increasing functionality around the PDI moiety, i.e. adding both bay and imide functionality, particularly imide functionality, to distort the PDI core, improves π-π stacking, and thus, solubility. The **PhO-Ph-PDI** product was isolated through a series of column chromatography with the purity of the **PhO-Ph-PDI** confirmed with ^{1}H NMR in d-$CDCl_3$ as shown in Figure 35.

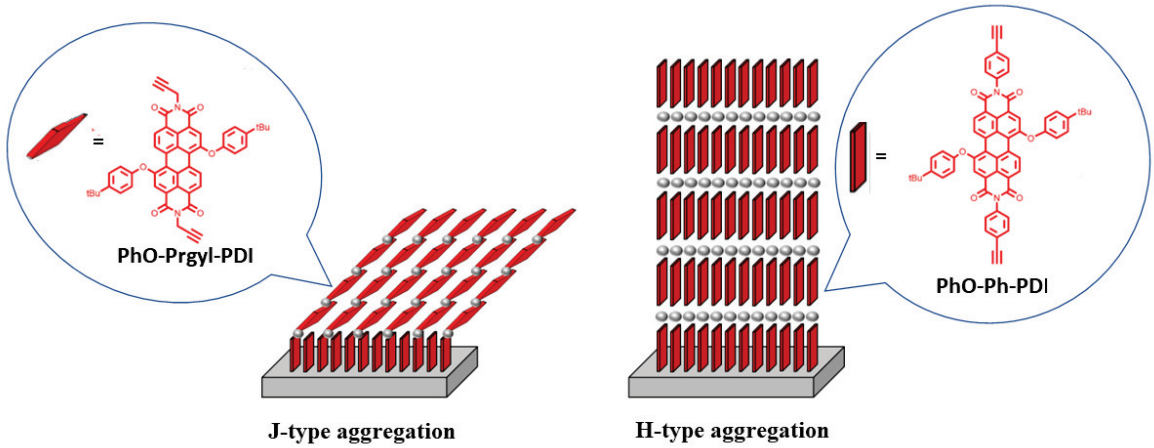

Figure 32. J-type aggregation of a propargyl imide functionalized phenoxy PDI (PhO-Prgyl-PDI) (left) and H-type aggregation of a phenylacetylene imide functionalized phenoxy PDI (PhO-Ph-PDI) (right). Multilayer assembly was grown on glass with an N_3Mest linker. Figure was adapted from.[153]

As **PhO-Ph-PDI** was utilized as the layer in the multilayer assembly, and **N_3Mest** was synthesized as the linker for the multilayer fabrication of the **PhO-Ph-PDI** thin-film EC material. The linker **N_3Mest** was selected as Guangyu Hu, determined that **N_3Mest** linker provided the best layer growth when compared to other azide functionalized linkers.[153] The **N_3Mest** linker has three azide locations for CuAAC click reactions with the terminal alkyne on the **PhO-Ph-PDI**. A common issue with other azide linkers involves their rotational flexibility with only two active azide sites. This flexibility may allow the linker to click with two different PDI layers within the multilayer assembly. This clicking of the linker to two different groups may render the linker unable to continue the multilayer growth. Comparatively, the **N_3Mest** has three active azide sites which may aid in increasing layer growth if two of the azide groups click with two different PDI layers, the third azide group could be used to rejuvenate some of the lost functionality. The dendritic nature of the **N_3Mest** may aid in reorienting the layer into a more upright position. The synthesis of **N_3Mest** is shown in Figure 34. and the ^{1}H NMR in d-$CDCl_3$ is similar to what has previously been reported.

4.1.2 Methods

General Methods and Materials. ^{1}H-NMR spectra were obtained on a Varian 500 MHz spectrometer and referenced to the solvent peak. LR and HR-ESI MS were obtained on a Thermo Electron Finnigan TSQ Quantum Ultra. Solvents, ACS grade or better, were purchased from Sigma Aldrich or Fischer Scientific and used as received unless specified otherwise.

Synthesis of PhO-PTCDA. A suspension of 1,7-brominated perylene tetracarboxylic dianhydride (Br-PTCDA) (0.905 g, 1.7 mmol) was previously synthesized by former graduate student Dr. Peter

Palomaki. The Br-PTCDA was reacted with 4-(tert-butyl)phenol (1.22 g, 8.145 mmol) in the presence of Cs_2CO_3 (1.661 g, 5.1 mmol) in dry degassed DMF (~ 70 mL). The reaction was refluxed under N_2 for 4 h. After 4 h, the reaction mixture was poured into water (50 mL) and neutralized with dilute HCl (~ 1 M, 10 % by volume) until a pH of approximately 7 was reached. The reaction mixture was stored for further workup.

Synthesis of TMS-PhO-Ph-PDI. A suspension of 5,12-bis(4-(tert-butyl)phenoxy)anthra[2,1,9-def:6,5,10-d'e'f']diisochromene-1,3,8,10-tetraone (PhO-PTCDA) (0.4281 g, ~6.22 mmol) was reacted with 4-((trimethylsilyl)ethynyl)aniline (0.697 g, 3.68 mmol) in the presence of zinc acetate (0.440 g, 2.40 mmol) in pyridine (32 mL) which was gently refluxed at 120˚C under nitrogen for 10 h. The reaction progress was measured via thin-layer chromatography (100 % methylene chloride). After the reaction, a silica plug in 100% methylene chloride was run to remove unreacted starting material. The remaining material was used without further purification.

Synthesis of PhO-Ph-PDI. TMS-PhO-Ph-PDI (0.311 mmol) was reacted with potassium floride (163.26 mg, 2.81 mmol) and 18-crown-6 ether (0.722 mL, 2.73 mmol) in THF (50 mL) and methanol (5 mL) which was stirred at rt under nitrogen for 48 h with the reaction progress being monitored by thin-layer chromatography (100% chloroform). After 48 h, the reaction mixture was run through a short column using methylene chloride to remove the 18-crown-6 and any unreacted starting material. The potential PhO-Ph-PDI products were removed from the column and thin-layer chromatography was used to observe purity (100 % methylene chloride). A preparatory thin-layer chromatography was run on the potential PhO-Ph-PDI products, using 100 % methylene chloride. The top band was collected and dried under a high vacuum overnight before being prepped for a ^{1}H NMR. **(PhO-Ph-PDI):** ^{1}H NMR (500 mHz, $CDCl_3$): 9.29 (d, J = 8.3 Hz, 2H),

8.46 (d, *J* = 8.3 Hz, 2H), 8.21 (s, 2H), 7.55 (d, *J* = 7.6 Hz, 4H), 7.39 (d, *J* = 7.7 Hz, 4H), 7.17 (d, J= 7.8 Hz, 4 H), 7.02 (d, J= 7.9 Hz, 4 H), 3.07 (s, 2H), 1.28 (s, 18 H). The synthesis of **PhO-Ph-PDI** is shown in Figure 33. and the ^{1}H NMR in d-$CDCl_3$ is shown in Figure 35 which is consistent with what has previously been reported.[81]

Synthesis of **1,3,5-Tris(azidomethyl)benzene (N_3Mest)**. **1,3,5-Tris(bromomethyl)benzene** (1.00 g, 2.80 mmol) was added was sodium azide (0.075 g, 1.15 mmol) in the presence of acetonitrile (40 mL) and the reaction mixture was refluxed under nitrogen for 12 h. The reaction progress was monitored by thin-layer chromatography (8:2, methylene chloride: hexanes). A column was run 8:2, methylene chloride: hexanes, and the first fraction was collected. After placing the products on the high vacuum overnight, a light-yellow oil was obtained for ^{1}H NMR. **1,3,5-Tris(azidomethyl)benzene (N_3Mest):** ^{1}H NMR (500 mHz, $(CD_3)_2CO$), 7.12 (s, 3H), 4.18 (s, 6 H).

Self-Assembled Monolayer (SAM) Preparation. Indium Tin Oxide (ITO) slide was selected, and the conductive side was tested with a multimeter. The ITO was sonicated in MeOH for ten minutes. After ten minutes the ITO was placed in a solution of K_2CO_3 in a 2:1 ratio of MeOH : water and sonicated for twenty minutes. After twenty minutes the ITO was rinsed with MeOH and placed in a 12-azidoundecylphosphonic acid solution in DMF (1.5 mM) with the conductive side face up. The ITO was allowed to sit for 24 hours. After 24 hours the ITO was rinsed with DMF and dried under an air stream before being placed in a vacuum oven at 75 ˚C to anneal for 1 hour.

Multilayer Fabrication. Layer additions of **PhO-Ph-PDI**: a solution of DMF containing ~12% water, 2.9 mM of PDI, 0.9 mM CuSO4, 1 mM Tris(benzyltriazolylmethyl)amine (THPTA), and

2.4 mM 2,5-di-tert-butyl-hydroquinone was placed in contact with one side of a SAM-functionalized ITO and placed in a covered Petri dish in a 30 ˚C oven. After twenty minutes, the ITO was washed with acetone, DCM, MeOH, 1 mM disodium ethylenediaminetetraacetate in 1:1 ethanol : DI water mixture, MeOH, and DI water.

Linker additions of **N3Mest**: a solution of DMSO containing ~14% water, 2.2 mM of N_3Mest, 4.4 mM CuSO4, 4.9 mM THPTA, and 8.9 mM sodium ascorbate was placed in contact with the dye side of the substrate and placed in a covered Petri dish in a 30 ˚C oven. After twenty minutes the slide was washed with the same solvents as above.

Chemical Reductions. Chemical reductions studies were carried out manner similar to a previous method,[53] using a quartz cuvette with the 1 cm optical path length. Solvents were anhydrous and deoxygenated. Samples were prepared in a N_2 purged glovebox in anhydrous THF. Chemical reduction was achieved by using small additions of Na(10%)–Hg with a slight excess of 18-crown-6 added to aid in the solubility of Na+ ions under air-free conditions. Clean conversion between the different redox states was confirmed by the appearance of isosbestic points.

Cyclic Voltammetry, Spectroelectrochemical Measurements, and Potential Step Spectroelectrochemistry Experiments. All electrochemical analysis measurements were completed with a three-electrode cell where the thin-film multilayer assembly was used as the working electrode, Ag wire was used as the reference electrode, and Pt was used as the counter electrode. Electrolyte use varied with the given experiment, but generally followed a 0.1 M concentration with the electrodes being referenced to the ferrocenium/ferrocene couple. All UV-Vis electronic absorption spectra for the spectroelectrochemical and potential step spectroelectrochemistry experiments were taken on a Perkin-Elmer Lambda 950 UV–vis

spectrometer or an Agilent 8453A spectrometer running Olisworks software. Samples were background subtracted using a quartz cuvette.

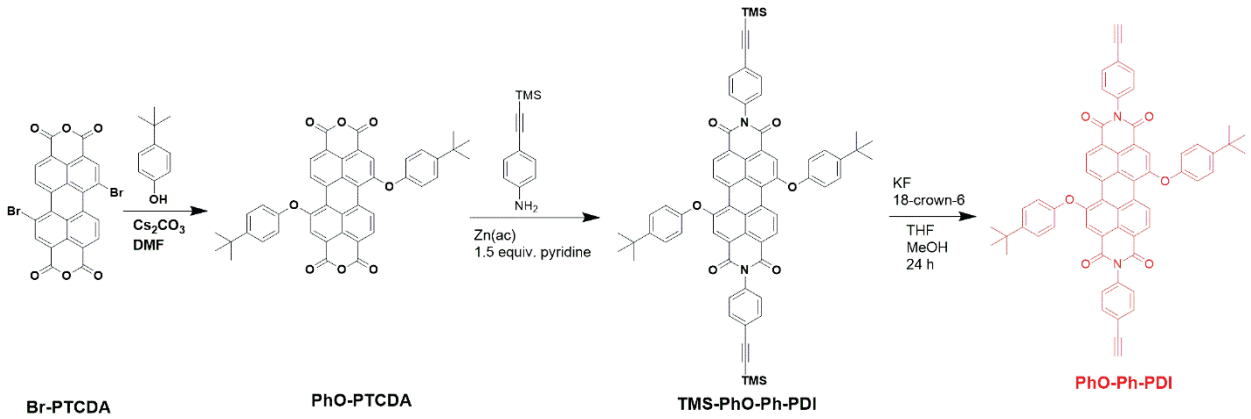

Figure 33. PhO-Ph-PDI synthesis for click chemistry with the Br-PTCDA starting material previously synthesized by Dr. Peter Palomaki.[81]

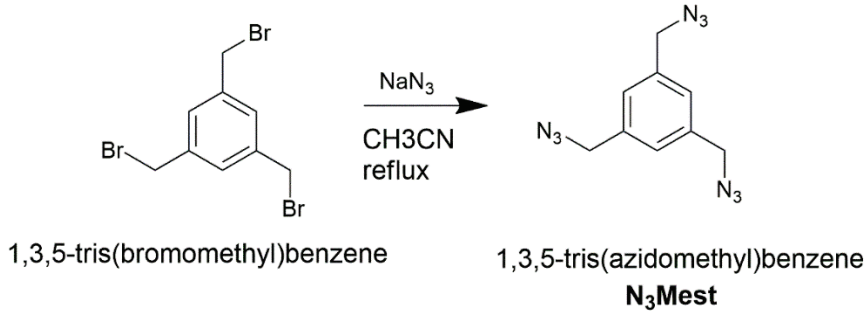

Figure 34. N_3Mest linker synthesis from 1,3,5-tris(bromomethyl)benzene.

4.1.3 NMR Analysis

The ^{1}H NMR of **PhO-Ph-PDI** as shown in Figure 35. and is similar to what has previously been reported in literature.[81] Beauvillier et al.[48] synthesized a bay functionalized p-(t-butyl)phenol PDI with propargyl imide functionality (PhO-PDI) instead of the phenylacetylene imide functionality shown in **PhO-Ph-PDI**. For the **PhO-Ph-PDI**, the bay protons exhibit a doublet-

doublet-singlet (d-d-s) splitting pattern observed from 9.49 to 8.21 ppm. Comparatively, the PhO-PDI bay protons exhibit a doublet-doublet-singlet (d-d-s) splitting pattern observed from 9.91 to 8.49 ppm. There are many other comparisons of bay protons with p-(t-butyl)phenol functionality in literature but with more than two bay functionalizations.

The **N_3Mest**, (1,3,5-tris(azidomethyl)benzene) has been previously reported in literature[48], but a ^{1}H NMR in $(CD_3)_2CO$ was completed for both the starting material 1,3,5-tris(bromomethyl)benzene and the **N_3Mest** linker for comparison of singlet peak shift between the protons nearest to the bromine substituent as compared to the azide substituent. The shift between the singlet pertaining to the protons nearest to the bromine substituent is 7.37 ppm, and for the azide is 7.12 ppm. The disappearance of the peak at 7.37 ppm was used to test for reaction completion.

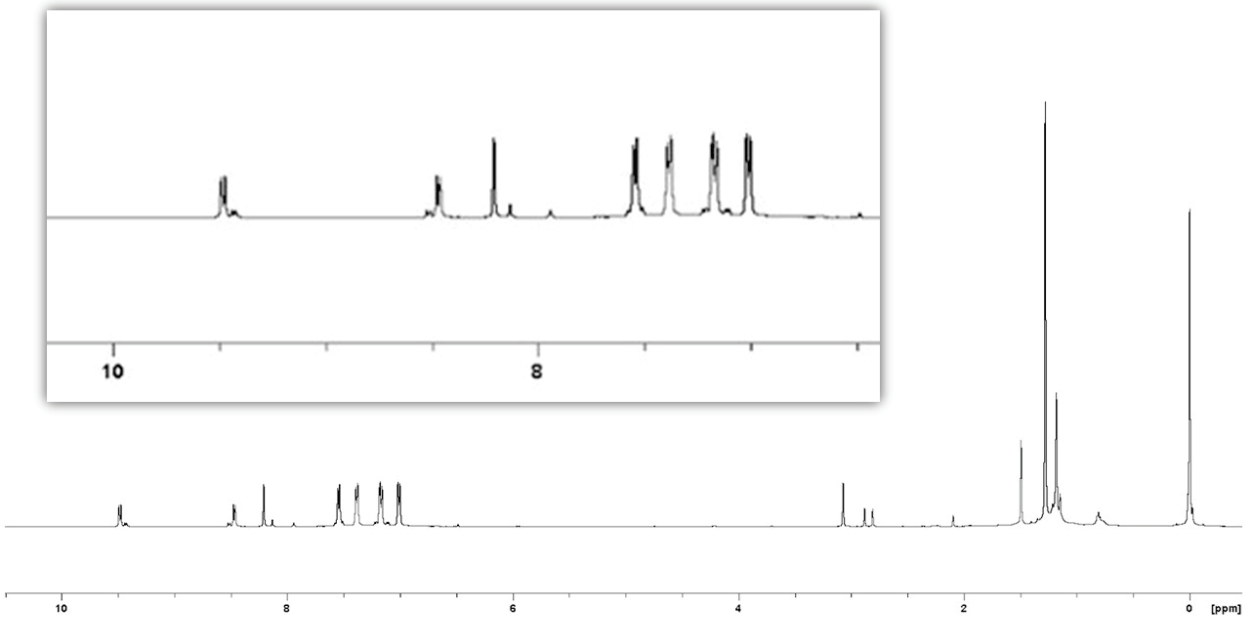

Figure 35. ^{1}H NMR of PhO-Ph-PDI PDI in $CDCl_3$ highlighting the aromatic proton splitting pattern which is located from around 7.0-10.5 ppm (spectra were referenced to the residual solvent peak $CHCl_3$ at 7.26 ppm.).

4.2 Self-Assembled Monolayer Preparation

Self-Assembled Monolayer (SAM) was prepared on conductive Indium Tin Oxide (ITO) using the phosphonic acid method from,[85] in which 12-azidododecylphosphonic acid was selected as the monolayer in which the perylene diimide (PDI) thin-film will be assembled. The 12-azidododecylphosphonic acid is comprised of an anchor group (phosphonic acid), the spacer (dodecyl chain), and tail (azide) as shown in Figure 36. The anchoring group of the phosphonic acid allows for multiple strong bonds between the metals and metal-oxide surfaces. The interaction usually results in the formation of a single monolayer in which any additional physiosorbed molecules can be easily rinsed off with solvent. For our purposes, the phosphonic acid head group forms a higher quality SAM on the ITO surface when compared to other SAM preparation involving silanes and thiols. In comparison to phosphonic acids, trialkyoxysilanes and trihalosilanes are prone to forming homocondensation products with Si-O-Si bonds,[154] as well as exhibit lower hydrolytic stability when compared to phosphonic acid.[155] Thiols, while they produce stable and ordered monolayers on gold, do not effectively functionalize with metal oxides.[156–158] An additional benefit of using phosphonic acid in SAM preparation involves the high stability of phosphonic acid in air. Phosphonic acid modification of metal oxides do not involve an air sensitive process and can be prepared without the use of a Schlenk line, whereas thiols and silanes are both susceptible to oxidation. The preparation of our phosphonic acid SAM with 12-azidododecylphosphonic acid is shown in Figure 36.

While the anchoring group of 12-azidododecylphosphonic acid is utilized for a stable and a uniform monolayer on the Indium Tin Oxide (ITO) surface, the spacer, or long chain alkyl, has been used to screen interactions of the interface between the added functionality to the SAM and the underlying substrate (ITO in this case).[159]Additionally, it is hypothesized that the spacer, or

alkyl chain, can influence surface reorganization as a function of monolayer viscosity. A more viscous monolayer made from a longer spacer may have a significant effect on the equilibrium structure of the SAM.

Finally, the azide tail of 12-azidododecylphosphonic acid is utilized within the Copper-Azide Alkyne Cycloaddition (CuAAC) click reaction between azide tail and terminal alkyne of the functionalized PDI. The first click reaction between the azide tail of phosphonic acid SAM and alkyne functionality of the PDI is shown in Figure 36.

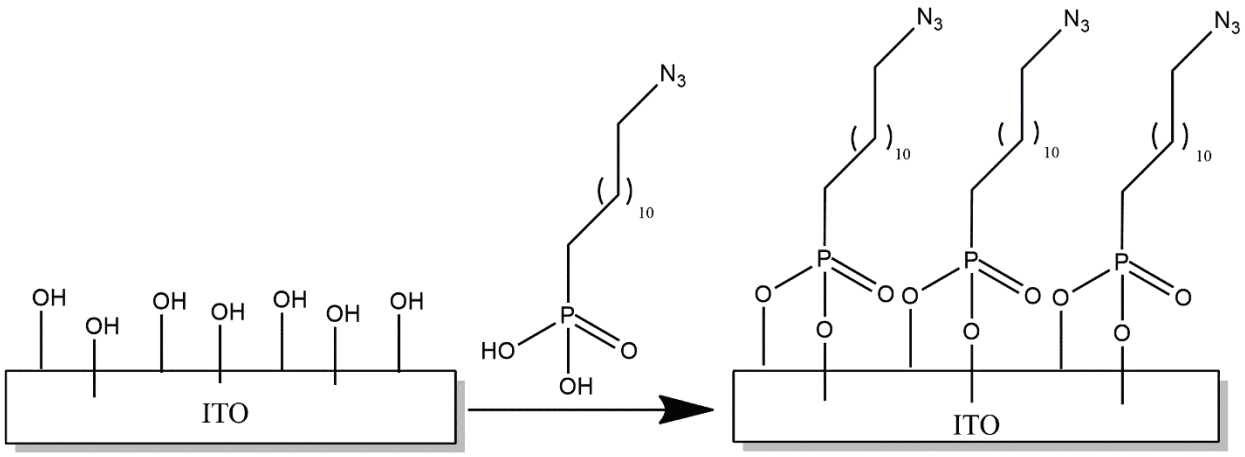

Figure 36. Self-Assembled Monolayer (SAM) preparation for Layer-by-Layer Assembly with 1.5 mM of 12-azidododecylphosphonic acid in THF.

4.3 Multilayer Assembly of Perylene Diimide Thin-Film

A multilayer thin-film of five layers of the **PhO-Ph-PDI** with **N_3Mest** linker were constructed using Copper-Azide Alkyne Cycloaddition (CuAAC) click reaction.[102] This thin-film was assembled via layer-by-layer (LbL) method, alternating between layers (**PhO-Ph-PDI**) and linkers (mestylene) in a bottom-up fabrication. This CuAAC LbL assembly of **PhO-Ph-PDI** and **N_3Mest** linker is shown in Figure 37. In this CuAAC LbL assembly, the azide tail on the

phosphonic acid SAM reacts with the terminal alkyne on the **PhO-Ph-PDI** to form a triazole linkage between the phosphonic SAM and **PhO-Ph-PDI** (Layer 1). The **PhO-Ph-PDI** Layer 1 possess a terminal alkyne which reacts with the azide on the N_3Mest to form a triazole linkage between Layer 1 and **N_3Mest** (Linker 1) forming a bi-layer. These steps are repeated by CuAAC LbL assembly until five layers of **PhO-Ph-PDI** are fabricated on the ITO surface. This LbL fabrication technique can be used to produce an *ordered*, *reproducible*, and *uniform* films which can be easy tuned via selection of the chromophore used in the layers. In this manuscript, **PhO-Ph-PDI** was used as the selected chromophore, but other chromophores can be used in LbL fabrication using the same methods. Figure 38. shows the absorbance used to follow growth of multilayers. The growth of the five layers of **PhO-Ph-PDI** linked through four triazole linkages, and four N_3Mest linkers shows a consistent increase in absorbance with each layer reaction. Figure 39. compares the reaction at each layer with the absorbance intensity at 523 nm showing a very linear plot. Both Figure 38. and Figure 39. show that each layer reaction is indicative of linear growth. The linear growth of the five layers of **PhO-Ph-PDI** is similar to what has previously been reported in literature with PhO-Prgyl-PDI[48] exhibiting the same absorbance profile.

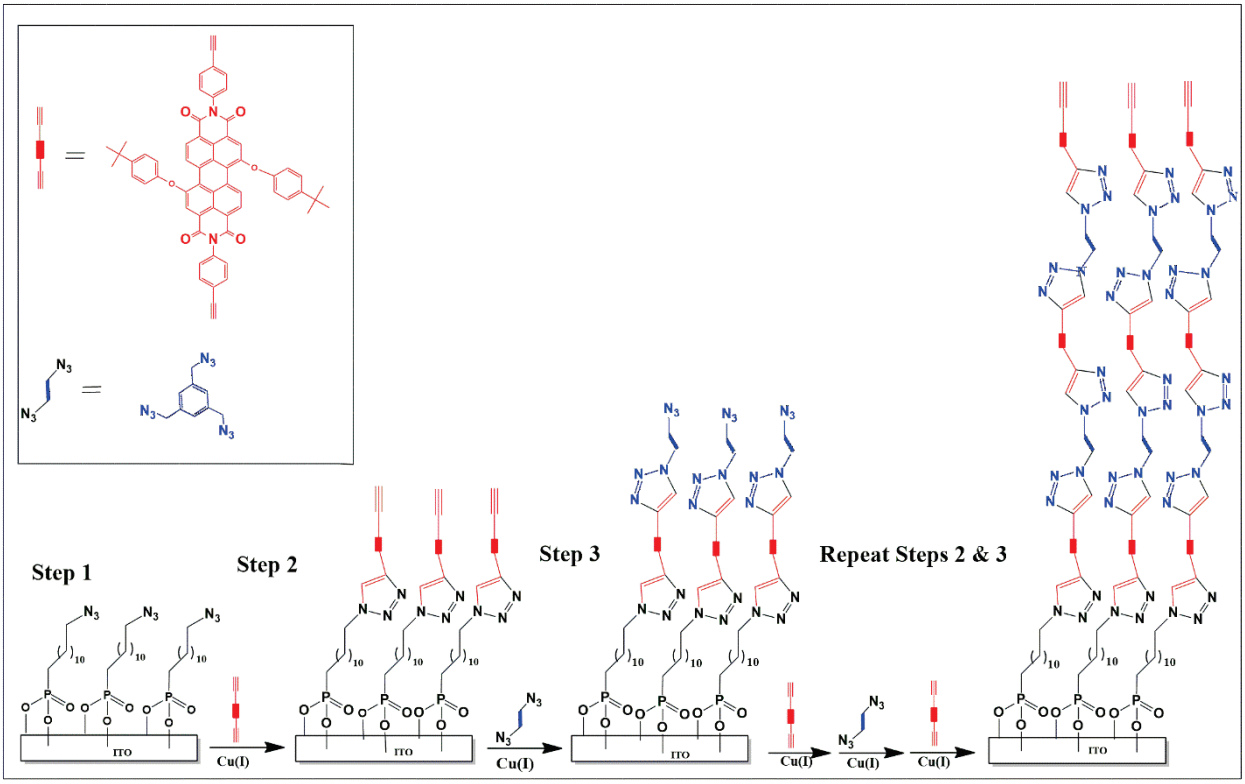

Figure 37. Layer-by-layer (LbL) assembly through Copper-Azide Alkyne Cycloaddition (CuAAC) "click" reactions of PhO-Ph-PDI with mestylene linker to achieve multilayer assembly.

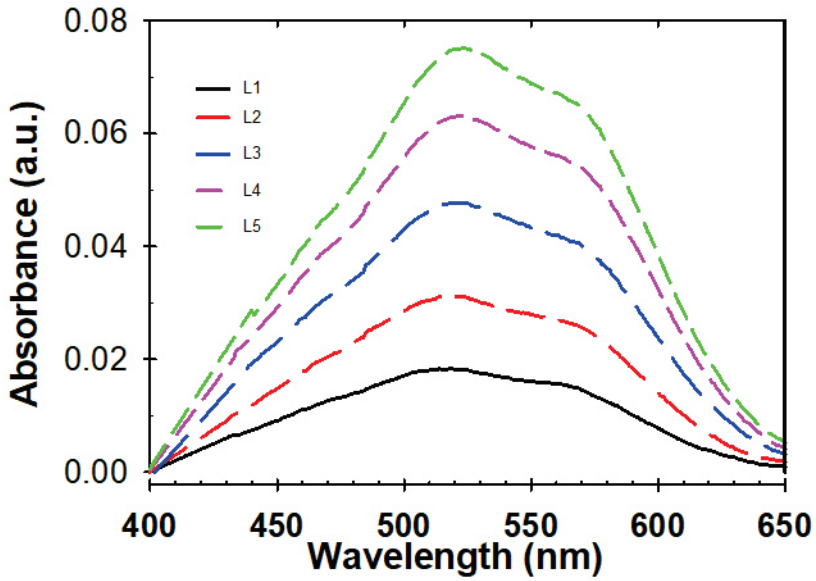

Figure 38. Visible absorption profiles obtained during the growth of five bilayers of PhO-Ph-PDI with N_3Mest linker.

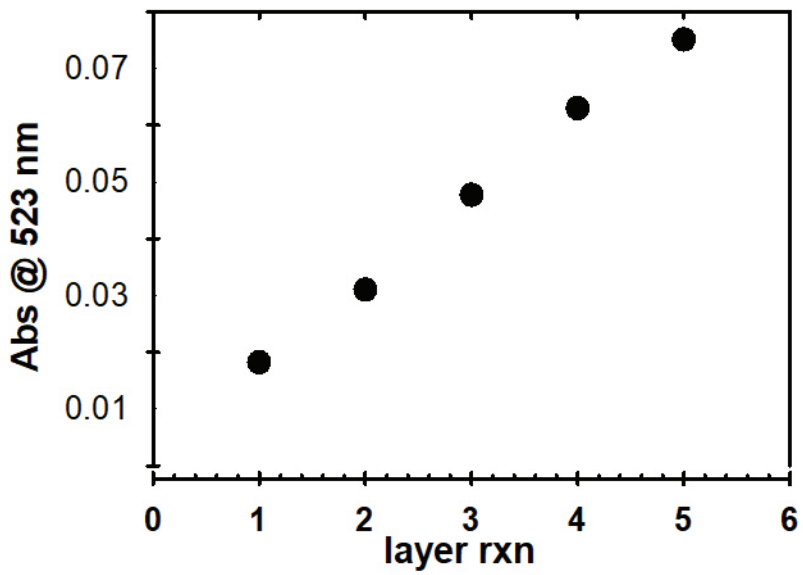

Figure 39. Comparison of layer rxn vs. the intensity of the absorbance peak at the maximum at 523 nm.

4.4 Electrochemical Analysis of the Perylene Thin-Film

The electrochemical properties of the **PhO-Ph-PDI** thin-film were determined by cyclic voltammetry (CV) in tetrabutylammonium hexafluorophosphate ($TBAPF_6$) in methylene chloride and acetonitrile, and tetramethylammonium hexafluorophosphate ($TMeAPF_6$) in acetonitrile. The $TMeAPF_6$ electrolyte was not studied in methylene chloride due to its solubility issues. In both electrolyte and solvents, the **PhO-Ph-PDI** thin-film undergoes two reductions in the range -0.8 to -1.3 V vs ferrocene/ferrocinium as shown in Figure 40 and Figure 41. The first reduction peak is observed at -0. 97 V, with the second reduction peak observed at -1.23 V. The $E_{½}^{0/-1}$ and $E_{½}^{-1/-2}$ values are -0.91 V and -1.15 V. The cyclic voltammetry data for the **PhO-Ph-PDI** thin-film in $TBAPF_6$ and $TMeAPF_6$ shows significant overlap between both reduction peaks. The first reduction between the neutral state and singly reduced state is far less prominent than the neutral state and the doubly reduced state.

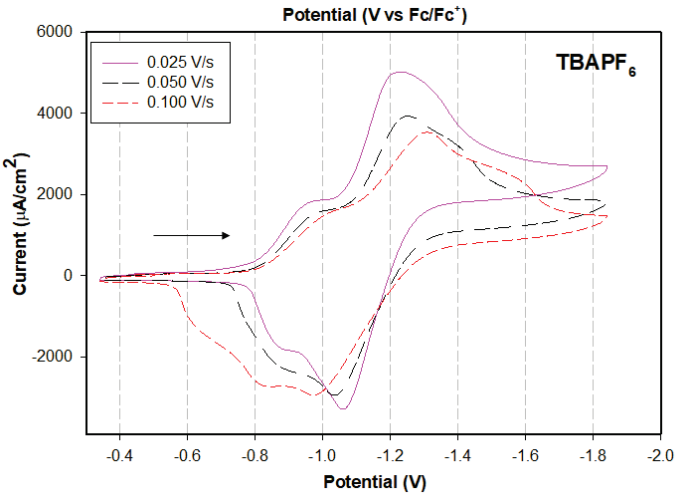

Figure 40. Normalized Cyclic Voltammetry (CV) scans for five layers of PhO-Ph-PDI with mestylene linker assembled on an ITO electrode. CVs were normalized by dividing the resultant current by the scan rate . CVs were obtained at varying scan rates (0.025 V/s, 0.05 V/s, and 0.10 V/s) with 0.1 M of $TBAPF_6$ in anhydrous methylene chloride as the electrolyte.

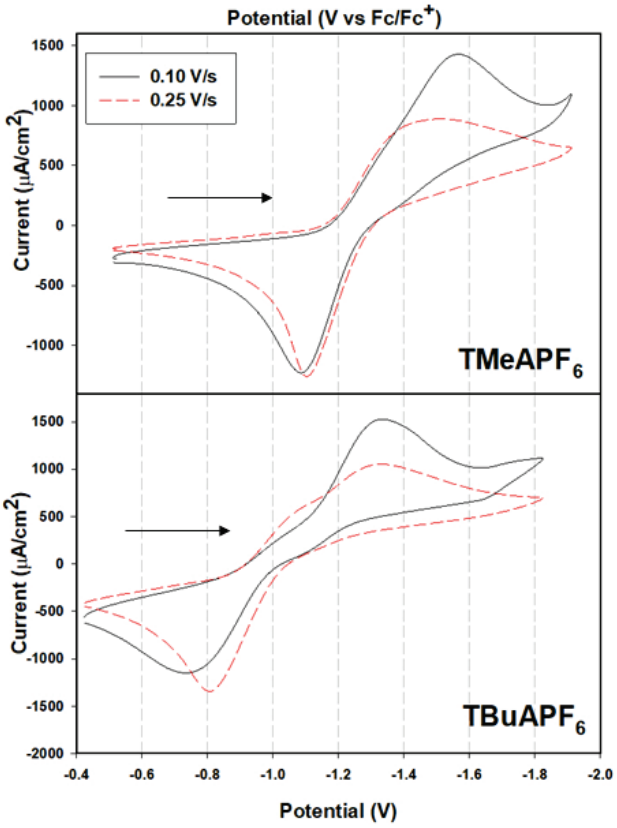

Figure 41. Normalized Cyclic Voltammetry (CV) scans for five layers of PhO-Ph-PDI with mestylene linker assembled on an ITO electrode. CVs were normalized by dividing the resultant current by the scan rate. CVs were obtained at varying scan rates (0.10 V/s, and 0.25 V/s) with 0.1 M of $TMeAPF_6$. and 0.1 M of $TBAPF_6$ in anhydrous acetonitrile as the electrolyte.

The significant overlap between the first and second reduction peaks in the **PhO-Ph-PDI** thin-film is similar to what has been reported in literature for other PDI films. Ma et al.[148] fabricated two PDI films in order to study their electrochemical properties. One film, poly-Cl-PBI, film contains a PDI unit with chlorine substituents on the 1,6,7,12 bay positions and two peripheral carbazoles at each imide position. The second film, poly-PO-PBI, film contains a PDI unit with phenoxy substituents on the 1,6,7,12 bay positions and two peripheral carbazoles at each imide position. Both the poly-Cl-PBI film and poly-PO-PBI film exhibited electrochemical behavior with two reversible peaks, the first reduction potential observed at -0.62 V for poly-Cl-PBI and -0.88 V for poly-PO-PBI, with the second reduction potential observed at -0.83 V for poly-Cl-PBI and -1.01 V for poly-PO-PBI. Both the poly-Cl-PBI and poly-PO-PBI were referenced to Ag/Ag^{+}. Comparatively, the poly-PO-PBI film exhibited a more negative applied potential relative to the poly-Cl-PBI potentially because the PO-PBI has a lower electron affinity within the core relative to the Cl-PBI. Büyükekşi et al.[151] synthesized a bay functionalized (4-methoxyphenoxy) tetra substituted PDI with two 5-amino-1,10-phenanthroline substituents at each imide position, electrochemical techniques of cyclic voltammetry (CV) ($TBAPF_6$ in methylene chloride) were carried out to yield a two reduction and two oxidation process. The $E_{½}^{0/-1}$ and $E_{½}^{-1/-2}$ values were observed at -0.54 V and -0.73 V, respectively, which occurs at a more positive reduction potential than the **PhO-Ph-PDI** thin-film in which $E_{½}^{0/-1}$ and $E_{½}^{-1/-2}$ values were observed at -0.91 V and -1.15 V, respectively.

While the **PhO-Ph-PDI** thin-film correlate with what has already been published in literature in terms of the location of the first and second reduction peaks[148,151] the significant overlap between the first and second reduction peaks show that clean conversion to reduced states was not achieved with $TBAPF_6$ or $TMeAPF_6$. Instead, **PhO-Ph-PDI** thin-films studied with $TBAPF_6$ and $TMeAPF_6$ showed a partial conversion to both the singly and doubly reduced state,

with the majority of the partial conversion favoring the doubly reduced state. Examination of these partial conversions were probed through calculations of surface coverages, charge, and percent conversions associated with the singly and doubly reduced state. These values are calculated from the cyclic voltammetry data in Figure 40 and Figure 41, and are summarized in Table 5.

Table 5. Determination of conversion to singly and doubly reduced states by comparison of cyclic voltammetry peaks in varying electrolytes and solvents.

Conversion to singly and doubly reduced states of PhO-Ph-PDI thin-film				
	Suspected Reduced State	$TMeAPF_6$	$TBAPF_6$	
		Acetonitrile	Methylene Chloride	Acetonitrile
Surface Coverage	-1	$3.70x10^{13}$ molec/cm^2	$1.94x10^{13}$ molec/cm^2	$2.52x10^{13}$ molec/cm^2
	-2	$1.95x10^{15}$ molec/cm^2	$3.07x10^{14}$ molec/cm^2	$9.27x10^{14}$ molec/cm^2
Charge	-1	$1.01x10^{-6}$C	$1.37x10^{-5}$C	$1.59x10^{-5}$C
	-2	$6.20x10^{-5}$C	$2.21x10^{-4}$C	$5.88x10^{-5}$C
% Conversion	-1	2.7	6.1	2.9
	-2	97.3	93.8	97.1

Table 5 compares surface coverage, charge, and % conversion between the smaller cation, $N(Me)_4,^+$ associated with $TMeAPF_6$ electrolyte in acetonitrile, to the larger $N(Bu)_4,^+$ cation in acetonitrile and methylene chloride. For both $TBAPF_6$ and $TMeAPF_6$ in acetonitrile, the singly reduced state percent conversion was ~3 %, with ~97 % being associated with the doubly reduced state. Despite $N(Me)_4,^+$ being a smaller cation relative to $N(Bu)_4,^+$ neither cation size may have effectively been able to penetrate the **PhO-Ph-PDI** thin-film. One possible cause may involve aggregation effects within the film fabrication in which the **PhO-Ph-PDI** thin-film is packed so tightly that either the $N(Me)_4^+$ cation or $N(Bu)_4^+$ cannot successfully penetrate the film until a potential of -1.4 V is achieved which is associated with the formation of the doubly reduced state. Interestingly, changing the solvent from acetonitrile to methylene chloride for $TBAPF_6$, increased

the singly reduced percent conversion from 3% to 6%. While $N(Bu)_4^+$ may be larger than $N(Me)_4^+$ using a less polar solvent like methylene chloride instead of a more polar solvent like acetonitrile may allow the cation to better penetrate and reduce the thin-film.

4.5 Chemical Reduction and CIE

To better probe the neutral, singly reduced, and doubly reduced species for the **PhO-Ph-PDI**, in situ chemical reduction with Na(Hg), in the presence of 18–crown–6, was employed to produce the singly and doubly reduced states. These conditions allowed for the clean conversion between redox states of the **PhO-Ph–PDI**. The absorption spectra of the neutral, singly reduced, and doubly reduced **PhO-Ph-PDI** in THF are shown in addition to the corresponding visual color changes are shown in Figure 43. The neutral species exhibits a peak at 537 nm with a shoulder at 501 nm. The singly reduced species exhibits a peak at 720 nm with a smaller peak at 892 nm. Finally, the doubly reduced species is blue-shifted relative to the singly reduced species, and red-shifted relative to the neutral species, but exhibits a peak at 607 nm with a small shoulder at 702 nm.

In comparison to the chemical reduction of **PhO-Ph-PDI**, the chemical reduction of the Thio-PDI derivatives in Figure 42. show similar trends. The **1,6-Thio-PDI**, the neutral state exhibits a peak at 553 nm, the singly reduced state exhibits a dominant peak at 733 nm, and the doubly reduced state exhibits two peaks of equal height at 619 nm and 595 nm. The chemical reduction of **1,7-Thio-PDI**, the neutral state exhibits a peak at 568 nm, the singly reduced state exhibits a dominant peak at 743 nm, and the doubly reduced state exhibits two peaks of nearly equal height at 595 nm and 620 nm. The chemical reduction of **1,6,7-Thio-PDI**, the neutral state exhibits a peak at 575 nm, the singly reduced state exhibits a dominant peak at 757 nm with an

additional shoulder at 885 nm, and the doubly reduced state at 624 nm. Similar to **PhO-Ph-PDI**, the Thio-PDI derivatives all exhibit a red shift between the neutral and singly reduced species, and a blue shift between the singly reduced and doubly reduced species with the doubly reduced species slightly red shifted relative to the neutral species.

Comparatively, Figure 43. shows the CIE (Commission Internationale de l'Eclairage) 1931 xy chromaticity diagram with the values calculated for **PhO-Ph-PDI** in the neutral, singly and doubly reduced states mirror the chemical reduction data in Figure 43. These results are also mirrored in the CIE calculations for the Thio-PDI derivatives in Figure 31.

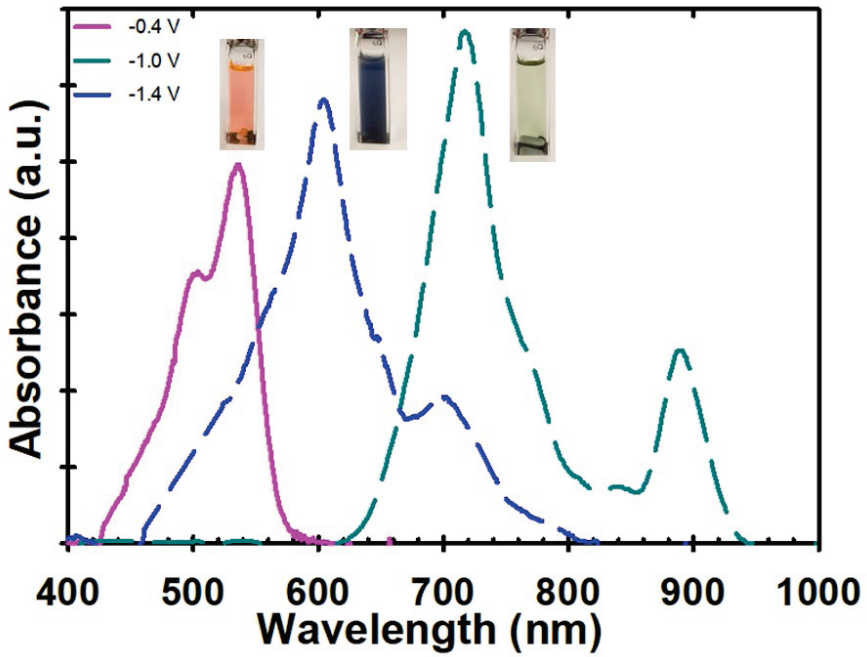

Figure 42. UV−Vis–NIR absorption spectra of PhO-Ph-PDI recorded in THF with 0.01 M 18-crown-6. The singly and doubly reduced state were generated by chemical reduction using Na(Hg). The spectra of neutral stat are shown as solid pink line, the singly reduced state as dashed turquoise lines, and the doubly reduced state as a dashed blue line. Included with the spectra are images of the cuvettes corresponding to the sample spectra.

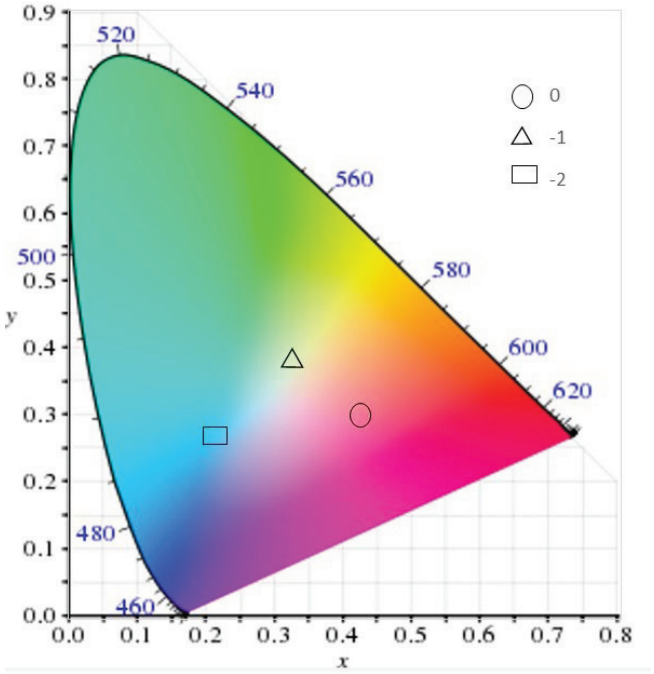

Figure 43. CIE 1931 xy chromaticity diagram with points calculated for the neutral, singly, and doubly reduced forms of PhO-Ph-PDI.

4.6 Spectroelectrochemical Analysis of the PhO-Ph-PDI Multilayers

Spectroelectrochemistry is a chemical technique which combines spectroscopy with electrochemistry. While, electrochemistry is used in a variety of disciplines including chemistry, biology, physics, materials study, information transfer,[160] and can provide information on redox potentials, concentrations of analyte species, and elucidation of reaction mechanisms through kinetic analysis,[161] is not suitable to identify unknown intermediates or products formed in redox reactions. Individually, both spectroscopy and electrochemistry have their utility, but together spectroelectrochemistry combines both reaction-oriented electrochemistry and species focused spectroscopy to provide a more qualitative and quantitative analysis of what is occurring on the electrode surface.

For bay-functionalized perylene diimides which can undergo a two-electron reduction process, spectroelectrochemical analysis reveals a few emerging trends from the neutral, to the singly reduced, to the doubly reduced state. For a PDI synthesized by Büyükekşi et al.,[151] the neutral species of the PDI exhibits a large peak at 599 nm. A reduction of the PDI to the singly reduced species shows a new peak at 800 nm. A second reduction of the PDI exhibits a peak at 677 nm. Comparatively, for a PDI synthesized by Würthner et al.,[149] the neutral species appears at 585 nm. A reduction of the PDI to the singly reduced species shows a peak 792 nm, 977 nm, and 1085 nm. A second reduction of the PDI exhibits a peak at 678 nm. Generally, the peak associated with the neutral species undergoes a red-shift to the singly reduced form and a final blue-shift to the doubly reduced form. Both Büyükekşi et al.,[151] and Würthner et al.,[149] observed peaks mimicking the general trends observed for chemical reduction data, i.e. the aforementioned red-shift between the neutral and single reduced peak, and blue-shift between the singly reduced and doubly reduced peak. Additionally, both Büyükekşi et al.,[151] and Würthner et al.,[149] observed full conversion to the reduced states as evident by only observing peaks associated with each reduction.

Spectroelectrochemical analysis was conducted on the **PhO-Ph-PDI** thin-film containing five bilayers as shown in Figure 44. In Figure 44 the spectroelectrochemical data was measured in $TBAPF_6$ to study the penetration of the $N(Bu)_4^+$ cation in the thin-film. In Figure 44, the spectroelectrochemical data was measured in $TMeAPF_6$ to study the penetration of the $N(Me)_4^+$ For the spectroelectrochemical data, both films had applied potentials of -0.4V, -1.0 V and -1.4 V, when referenced to the ferrocenium/ferrocene couple. These applied potentials of -0.4V, -1.0 V and -1.4 V are used to probe the neutral, singly reduced and doubly reduced species observed in the cyclic voltammetry data in Figure 40 and Figure 41. Both **PhO-Ph-PDI** thin-films studied with $TBuAPF_6$ and $TMeAPF_6$ exhibited a similar peak pattern to what was previously observed by

Büyükekşi et al.[151] and Würthner et al.[149] The reduction of the **PhO-Ph-PDI** neutral thin-film to the singly reduced species resulted in red-shift, and the reduction form singly reduced to doubly reduced species resulted in a blue-shift. However, even though the location of the neutral, singly reduced, and doubly reduced species were similar to what was observed in literature,[149,151] and were consistent with the locations of peaks observed in the chemical reduction data in Figure 42., the intensity of the peaks was not consistent. The **PhO-Ph-PDI** thin-films should fully mimic the location and intensity of the peaks associated with the singly and doubly reduced states if the films are being reduced fully. However, neither the $N(Bu)_4^+$ cation nor the $N(Me)_4^+$ cation fully mimicked the chemical reduction data.

The **PhO-Ph-PDI** thin-film studied with the $N(Bu)_4^+$ cation is shown in Figure 44. The potential of -0.4V volts shows a steep peak at 557 nm which is analogous to the chemical reduction data in Figure 42. with the neutral species exhibiting a peak at 537 nm. When a potential of -1.0 V was applied to access the singly reduced species as shown in Figure 44., the same peak at 557 nm is observed with the emergence of two new peaks 735 nm, and 950 nm. These two new emerging peaks are similar to the chemical reduction data and are indicative of the singly reduced species. However, the presence of the peak at 557 nm, which is indicative of the neutral species, indicates only a partial conversion to the singly reduced species. Comparatively, a potential of -1.4 V was applied to access the doubly reduced species. At -1.4 V a large peak at 557 nm and a smaller peak at 615 nm is observed. The smaller peak at 615 is analogous to the doubly reduced species as the chemical reduction data in Figure 42. shows a peak at 607 nm. However, the presence of the peak at 557 nm also indicates the presence of neutral species. Thus, like the singly reduced species probed at -1.0 V, the doubly reduced species at -1.4 V does not achieve full conversion to the doubly reduced species, but instead involves a mixed state between the desired reduced state and the neutral state.

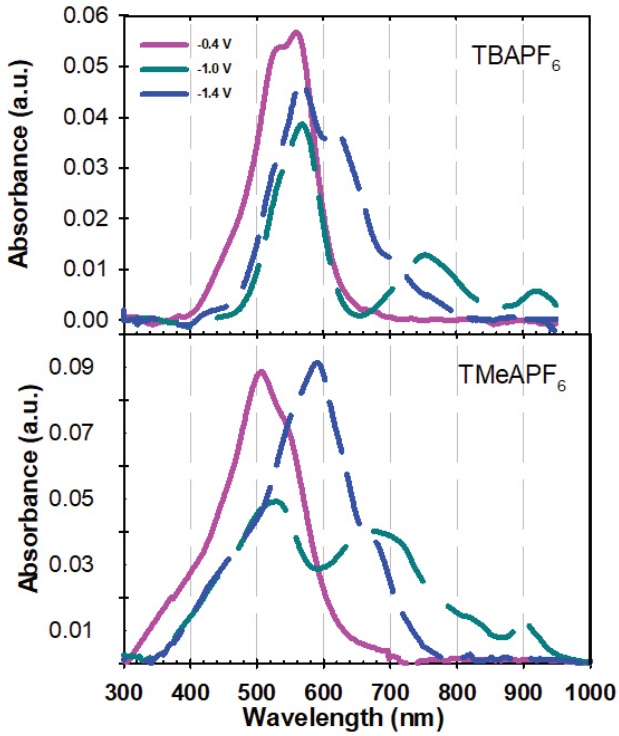

Figure 44. UV-Vis absorption spectra of $TBAPF_6$ (0.1 M) in methylene chloride (top) and $TMeAPF_6$ (0.1 M) in acetonitrile referenced to ferrocene/ferrocenium using spectroelectrochemical methods at 273 K.

The **PhO-Ph-PDI** thin-film studied with the $N(Me)_4^+$ cation is shown in Figure 44. The potential of -0.4V volts shows a steep peak at 513 nm with a large shoulder. This peak is analogous to the chemical reduction data in Figure 42. with the neutral species exhibiting a peak at 537 nm. When a potential of -1.0 V was applied to access the singly reduced species as shown in Figure 44, a peak is observed at 530 nm, 680 nm, and 902 nm. The peaks at 680 nm and 902 nm are indicative of the singly reduced species and are consistent with the chemical reduction data in Figure 42., but the peak at 530 nm is indicative of the still present neutral species. Comparatively, a potential of -1.4 V was applied to access the doubly reduced species. At -1.4 V a large peak is observed at 592 nm. This peak at 592 nm is similar to the doubly reduced peak in the chemical reduction data in Figure 42 and indicates a full reduction to the doubly reduced species.

As previously mentioned, spectroelectrochemical reduction with the $N(Bu)_4^+$ cation only achieved partial reduction for the singly and doubly reduced states, and reduction with the $N(Me_4)^+$ only achieved partial reduction for the singly reduced state. To probe the partial conversion of singly and reduced states for the $N(Bu)_4^+$ and $N(Me)_4^+$ cation, Table 6. calculates what relative percentage is achieved for the reduced states when compared to the expected peak heights from the chemical reduction data in Figure 42. For the $N(Bu)_4^+$ cation, approximately 16-17% conversion is achieved for the singly reduced state and 56 % was achieved for the doubly reduced state. Comparatively, for the $N(Me)_4^+$ cation, 32-34 % conversion is achieved for the singly reduced state and 88 % was achieved for the doubly reduced state. Given that the spectroelectrochemical data for the $N(Me)_4^+$ cation shows no peaks associated with the neutral species, it can assumed that this 88 % does involve full conversion to the doubly reduced state. The 88 % conversion may be related to other factors such as aggregation effects within the **PhO-Ph-PDI** thin-film or the comparison of the chemical reduction data which was measured in solution, and the spectroelectrochemical data which involves the **PhO-Ph-PDI** thin-film. What is most interesting is a much higher conversion to the singly and doubly reduced state is observed with the smaller $N(Me)_4^+$ cation, 32-34 % and 88 %, as compared to the larger $N(Bu)_4^+$ cation, 16-17% and 56 %. Thus, the use of the smaller $N(Me)_4^+$ cation may penetrate the thin-film more effectively than the larger $N(Bu)_4^+$ cation, leading to better conversion to the desired reduced state.

Table 6. Conversion to singly and doubly reduced states by comparison of spectroelectrochemical (SEC) peaks to chemical reduction (CR) peaks.

Comparison of conversion to singly and doubly reduced states						
Potential (V)	$TBAPF_6$			$TMeAPF_6$		
	Peak (nm)	$\frac{\text{SEC Peak}}{\text{CR Peak}}$	% Conversion relative to CR	Peak (nm)	$\frac{\text{SEC Peak}}{\text{CR Peak}}$	% Conversion relative to CR
-0.4 V	560	1	100 %	508	1	100
-1.0 V	753 920	0.16 0.17	16 % 17 %	672 899	0.34 0.32	34% 32%
-1.4 V	618	0.56	56%	590	0.88	88%
[a] V vs $Fc^{0/+}$						

4.7 Potential Step Experiments

To probe the nature of the singly and doubly reduced states observed in the spectroelectrochemical measurements, a series of potential step experiments were carried out. These potential step experiments measure current as measured as a function of time.[162] In these experiments, a square-wave potential is applied to the working electrode with the assumption that the measured current changes in relation to the diffusion of a bulk analyte to the sensor surface.[163] By measuring the change in current over time, the diffusion of a species within the **PhO-Ph-PDI** thin-films can be probed. As previously discussed, the cyclic voltammetry data in shows that only a partial conversion of ~3% was achieved for both the $N(Me)_4^+$ cation and $N(Bu)_4^+$ cation in the **PhO-Ph-PDI** thin-film as shown in Table 5. The 3 % conversion to the singly reduced state may have been due to aggregation effects or the charging of the charged at a faster rate than the charge can diffuse through the thin-film, resulting in a mixed reduced state. Additionally, the spectroelectrochemcial analysis, which occurs on a much slower timescale than the cyclic voltammetry studies were able to determine that $N(Me)_4^+$ cation achieved a 88 % conversion to the singly reduced state as compared to the 56 % observed with the $N(Bu)_4^+$ cation as shown in

Table 6. Potential step experiments should better elucidate the relationship between the size of the electrolyte in penetration of the **PhO-Ph-PDI** thin-film, the stability, and potential utility of the **PhO-Ph-PDI** thin-film as electrochromic devices.

Potential step experiments were used to monitor the stability of the **PhO-Ph-PDI** thin-film in $TBAPF_6$ and $TMeAPF_6$ by examining how fast these films can be switched from different potentials. The applied potential was switched between -0.4 V to -1.0 V to switch between the neutral and the singly reduced state as shown in Figure 45 for $TBAPF_6$, and Figure 48 for $TMeAPF_6$. The potential was switched between -0.4 V to -1.4 V to switch between the neutral and the doubly reduced state as shown in Figure 46 for $TBAPF_6$, and Figure 49 for $TMeAPF_6$. The potential was switched between -1.0 V and -1.4 V to switch between the singly reduced and doubly reduced state as shown in Figure 47 for $TBAPF_6$, and Figure 50 for $TMeAPF_6$. All potentials were referenced to the ferrocene/ferrocenium couple. The selected wavelengths in Figure 45-Figure 50 correspond to the peaks associated with the neutral, singly, and doubly reduced states within the spectroelectrochemical data in Figure 44. The onset of a potential associated with a specific state should result in an increase in the corresponding absorbance peak associated with that state. For example, the chemical reduction of **PhO-Ph-PDI** in Figure 42 predicts a peak associated with the singly reduced state near 735 nm. Thus, when this wavelength of 735 nm is set and a potential of -1.0 V is applied, a corresponding increase in absorbance should mirror the intensity of the absorbance observed within the chemical reduction data in Figure 42 and the spectroelectrochemical data in Figure 44. This mirroring indicates full conversion to the singly reduced state. If the intensity of the absorbance profile is less intense than expected, or if the shape of the absorbance does not follow the applied potential square wave, or if the charging current shows a delay in discharging, these factors may indicate the resistance, a limitation in the charge pushed through the **PhO-Ph-PDI** thin-film, or a lack of faradic response due to other factors.

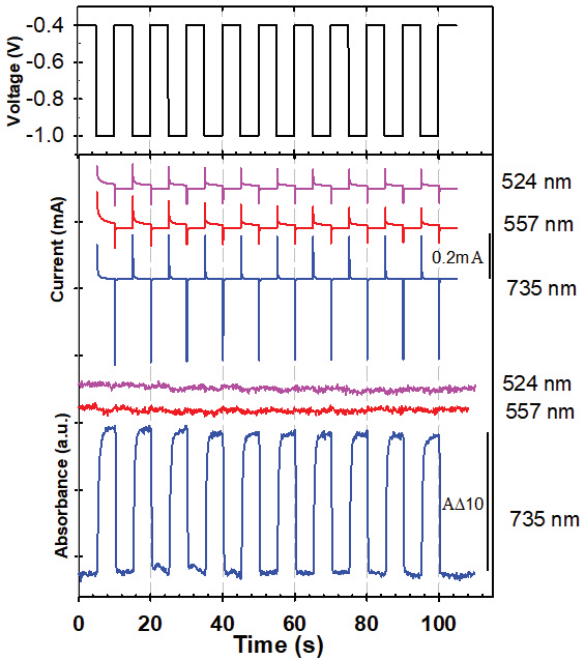

Figure 45. Potential Step Spectroelectrochemistry experiment -0.4 to -1.0 volts with $TBAPF_6$ referenced to the ferrocenium/ferrocene couple where the (top) square-wave applied potential, (middle) resultant change in current, and (bottom) is the resultant change in absorbance.

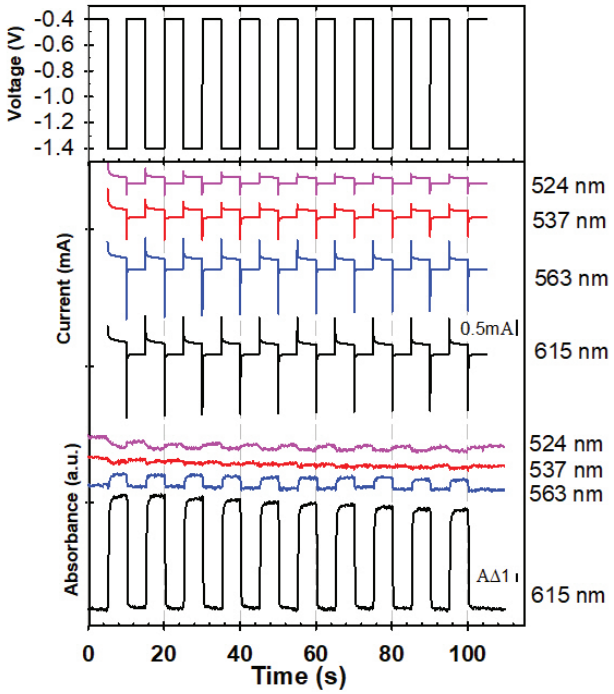

Figure 46. Potential Step Spectroelectrochemistry experiment -0.4 to -1.4 volts with $TBAPF_6$ referenced to the ferrocenium/ferrocene couple where the (top) square-wave applied potential, (middle) resultant change in current, and (bottom) is the resultant change in absorbance.

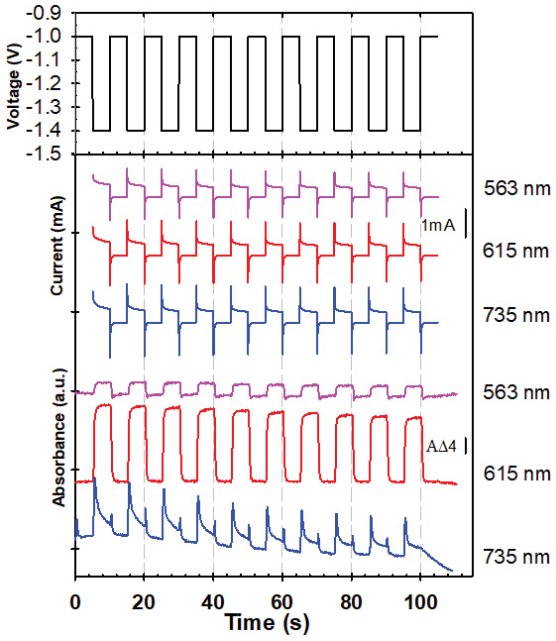

Figure 47. Potential Step Spectroelectrochemistry experiment -1.0 to -1.4 volts with $TBAPF_6$ referenced to the ferrocenium/ferrocene couple where the (top) square-wave applied potential, (middle) resultant change in current, and (bottom) is the resultant change in absorbance.

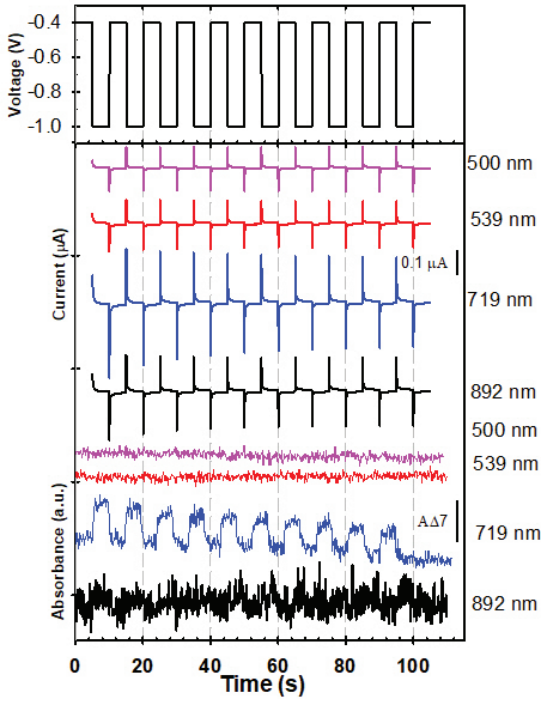

Figure 48. Potential Step Spectroelectrochemistry experiment -0.4 to -1.0 volts with $TMeAPF_6$ referenced to the ferrocenium/ferrocene couple where the (top) square-wave applied potential, (middle) resultant change in current, and (bottom) is the resultant change in absorbance.

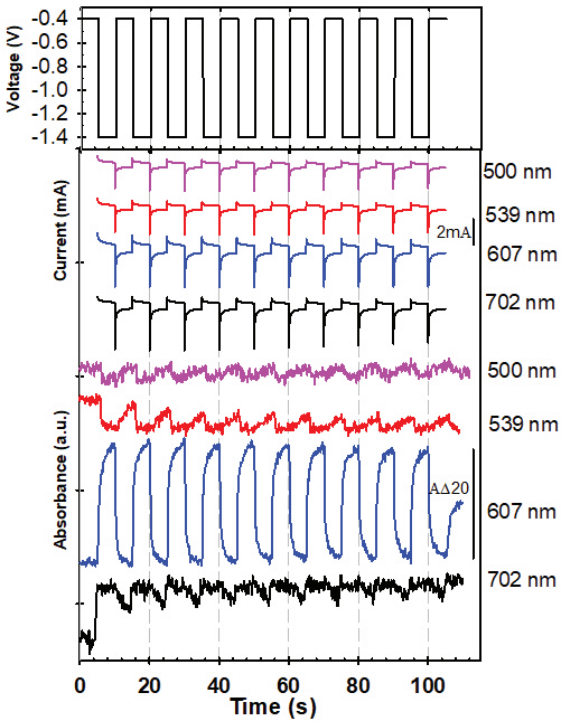

Figure 49. Potential Step Spectroelectrochemistry experiment -0.4 to -1.4 volts with $TMeAPF_6$ referenced to the ferrocenium/ferrocene couple where the (top) square-wave applied potential, (middle) resultant change in current, and (bottom) is the resultant change in absorbance.

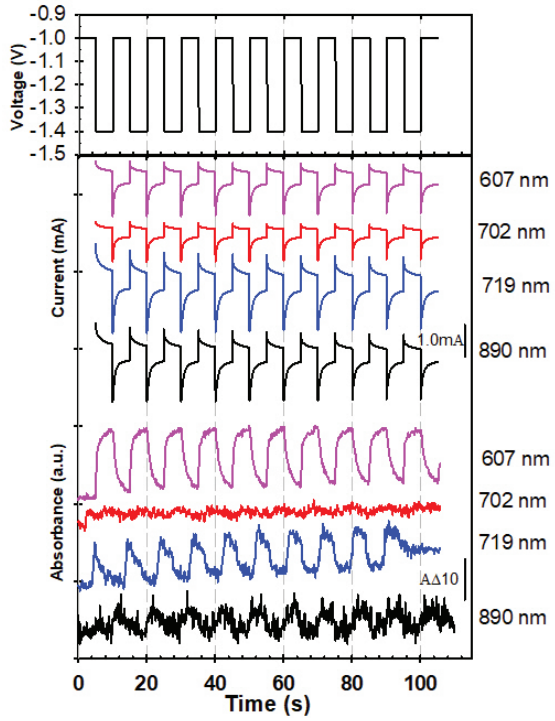

Figure 50. Potential Step Spectroelectrochemistry experiment -1.0 to -1.4 volts with $TMeAPF_6$ referenced to the ferrocenium/ferrocene couple where the (top) square-wave applied potential, (middle) resultant change in current, and (bottom) is the resultant change in absorbance.

Switching from the neutral state at -0.4 V to the doubly reduced state at -1.4 V, a positive increase in absorbance is observed for the corresponding wavelengths associated with the doubly reduced state at approximately 615 nm for the $TBAPF_6$ electrolyte as shown in Figure 46 and 607 nm with the $TMeAPF_6$ in Figure 49. Interestingly, the shape of the absorbance profile associated with 615 nm and 607 nm indicates a delay in the full charging of the thin-film even after the applied potential has made a full switch. This is most pronounced with the absorbance peaks 607 nm with the $TMeAPF_6$ which show an obvious curvature to the absorbance peak indicating slower kinetics than observed for the absorbance profile associated with 615 nm for $TBAPF_6$. Examination of the resultant current at 615 nm for $TBAPF_6$ and 607 nm with the $TMeAPF_6$ shows a gradual decay which is consistent with the absorbance profile for both.

Switching from the neutral state at -0.4 V to the singly reduced state at -1.0 V, a positive increase in absorbance is observed for the corresponding wavelengths associated with the doubly reduced state at approximately 735 nm for the $TBAPF_6$ electrolyte as shown in Figure 45, and 719 nm with the $TMeAPF_6$ in Figure 48. Interestingly, for the $TMeAPF_6$ in Figure 48, the relative intensity is far less than for the $TBAPF_6$. However, this decrease in intensity could be due to the general degradation of the **PhO-Ph-PDI** thin-film over all of the switching experiments as the $TMeAPF_6$ in Figure 48 underwent more several more experiments than the $TMeAPF_6$ in Figure 48. General degradation of the thin-film is a general consideration for electrochromic materials. Examination of the absorbance peaks for both the $TBAPF_6$ and $TMeAPF_6$ show little curvature relative to the doubly reduced state in Figure 46. This is consistent with the current as the discharge seems also relatively immediate. This reduced curvature in the absorbance peak, and thus, sluggish kinetics, may be due to the lower percentage of singly reduced species formed relative to the doubly reduced species as seen in the cyclic voltammetry data in Table 5 and the spectroelectrochemical data in Table 6. The cyclic voltammetry data in Figure 41 almost indicates

that the singly reduced species occurs in such minute amounts that it can almost be considered an intermediate between the neutral and doubly reduced species, thus reduction to this intermediate singly reduced species would occur on a much faster timescale relative to the doubly reduced species.

The relationship between the fraction of singly reduced species and fraction of doubly reduced species is further explored in switching from the singly reduced state at -1.0 V to the doubly reduced state at -1.4 V at approximately 615 nm and 735 nm for the $TBuAPF_6$ electrolyte, and 607 nm and 719 nm for the $TMeAPF_6$ electrolyte as shown in Figure 50. Perhaps, as expected, the absorbance peaks associated with the doubly reduced state are more intense than the absorbance peaks associated with the singly reduced state for both the $TBuAPF_6$ and the $TMeAPF_6$ electrolyte. For both electrolytes there is also a curvature to the absorbance peaks associated with the singly and doubly reduced profiles indicating slower kinetics that do not fully follow the switching potentials. This is particularly pronounced with the switching from -1.0 V to -1.4 V for $TBuAPF_6$ in Figure 47. which shows an increase in absorbance at -1.0 V and then an immediate decay even at the wavelength of 735 nm which is associated with the singly reduced state in the chemical reduction data in Figure 42. This immediate decay from the singly reduced to the doubly reduced state is consistent with the lower surface coverages and percent conversion to the singly reduced state for the $TBuAPF_6$ relative to the $TMeAPF_6$ in Table 6.

4.8 Concluding Remarks

In this chapter, a **PhO-Ph-PDI** thin-film was fabricated to observe the possible use of the **PhO-Ph-PDI** thin-film in an EC device. The **PhO-Ph-PDI** and **N_3Mest** linker were synthesized and characterized with ^{1}H NMR. The thin-film multilayer assembly was fabricated on an Indium Tin Oxide (ITO) surface as ITO is conductive and transparent which makes it an ideal material for

use in EC devices. CuAAC click chemistry was used to fabricate a five layered **PhO-Ph-PDI** thin-film using a layer-by-layer (LbL) assembly technique. The layers of **PhO-Ph-PDI** thin-film showed a linear and reproducible growth as observed by UV-Vis absorbance measurements.

The study of the **PhO-Ph-PDI** thin-film in an EC device required initial study of the electrochemical properties of the **PhO-Ph-PDI** thin film. The first study utilized cyclic voltammetry measurements with $TBAPF_6$ and $TMeAPF_6$ to study if a smaller cation size led to better penetration of the thin films. The cyclic voltammetry (CV) studies of the **PhO-Ph-PDI** thin-film showed reduction potentials associated with the neutral state (-0.4 V), a singly reduced state (-1.0 V), and a doubly reduced state (-1.4 V) when referenced to ferrocene/ferrocenium redox couple. CV studies indicated that there was no clean conversion to the singly or doubly reduced states regardless of electrolyte size, as both $TBAPF_6$ and $TMeAPF_6$ exhibited ~ 3 % conversion to the singly reduced state in acetonitrile. However, $TBAPF_6$ in methylene chloride increased the rate of conversion from 3 % in acetonitrile to 6 % in methylene chloride, implying that clean conversion requires not only a small electrolyte to penetrate the thin-film, but a less polar solvent like methylene chloride to allow for higher % conversion to the singly reduced state.

Chemical Reductions were used to better probe the neutral, singly reduced, and doubly reduced state for the **PhO-Ph-PDI** thin-film. The chemical reduction of **PhO-Ph-PDI** showed full reduction from the neutral to the singly and doubly reduced species as well as the corresponding absorption peaks associated with each state. The full reduction of **PhO-Ph-PDI** showed a variety of color change between the neutral and reduced states which corresponded to the CIE calculation. Applying the CIE calculation and peak information from the chemical reduction data, in theory, the **PhO-Ph-PDI** should be able to be achieve neutral, singly reduced, and doubly reduced states.

With the chemical reduction peaks for the neutral, singly reduced, and doubly reduced species, spectroelectrochemical measurements were conducted in the hopes of mimicking the

chemical reduction data. Similar to the CV studies, the spectroelectrochemical measurements were carried out both in $TBAPF_6$ and $TMeAPF_6$ to further study if a smaller cation size led to better penetration of the thin-films, and if full conversion can be achieved like the chemical reduction data. While neither the butyl or methyl cation led to full conversion of the suspected singly reduced state for the **PhO-Ph-PDI** thin-film, the methyl cation was able to promote full conversion between the neutral and doubly reduced species. This full conversion to the doubly reduced state with the smaller methyl cation indicates that a smaller size cation may better penetrate the **PhO-Ph-PDI** thin-film than the larger butyl cation.

Further study of the effects of cation size were applied to potential step spectroelectrochemical studies in which an applied potential cycled rapidly between two suspected states. These states could be neutral to the singly reduced state, neutral to the doubly reduced state, and singly reduced to the doubly reduced state. Potential-step spectroelectrochemistry data revealed that neither the butyl nor the methyl cation was able to fully achieve the singly reduced species, as similarly observed in the spectroelectrochemical data, but there was full conversion observed from the neutral to the doubly reduced state. Thus, from the spectroelectrochemical data and potential step spectroelectrochemical data, the smaller methyl cation size allowed for better penetration of the thin-film relative to the larger butyl cation. Therefore, like the use of a less polar solvent to promote a higher % conversion to the reduced state as observed in the CV studies, the use of a smaller cation size to better penetrate the thin-film seems to also be an important determinant for development of EC materials.

The lack of full conversion to the singly reduced species for either the $N(Bu)_4^+$ or $N(Me)_4^+$ cation was not a desired outcome for the **PhO-Ph-PDI** thin-film as an EC device. Ideally, an EC device should switch rapidly from different colored states and retain stability through the switching process. As previously discussed, the **PhO-Ph-PDI** thin-film is likely not being fully reduced

throughout the entire multilayer assembly. With the use of less polar solvents and smaller sized electrolytes, the singly and doubly reduced states may achieve a higher percent conversion, and maybe even a full conversion to the doubly reduced state, but overall the **PhO-Ph-PDI** thin-film currently is not well suited as an EC device. One possibility that full conversion was not reached for either electrolyte may be that the structure of the **PhO-Ph-PDI** thin-film in which the molecular assemblies packed too closely together to allow effective cation penetration. A synthetic approach to combat this tight packing will be discussed in the future directions of this manuscript.

5. CONCLUSION

In conclusion, to combat climate change and provide for future energy security as non-renewable energy sources are depleted, more energy efficient technologies need to be developed. One energy efficient technology is electrochromic (EC) devices which can undergo an intense color change as the result of an electron-transfer process.[6] Current EC devices are already cited at reducing energy use in heating and cooling buildings[7] which account for 30 % of global energy consumption. Additionally, EC devices can utilize a lower energy consumption relative to current displays due to their ability to maintain an optical state without a continuous input of electrical power.[10] Aside from their reduction in energy consumption, EC devices have the added benefit of utility in improving consumer daily life as in visualized energy storage and wearable electronics.

There are several types of EC devices, but small organic molecule based EC devices are perhaps some of the most promising emerging technologies as small organic molecules can exhibit intense coloration, and chemical functionalization can allow for more photophysical specificity, if the stability[31] issues associated with small organic molecules can be overcome. The small organic molecule that was selected for study within an EC device was a perylene diimide (PDI). PDIs have exceptional chemical, photo, thermal stability,[33] high tinctorial strength,[34] and functionalization of the bay position fine tunes the photophysical properties of the PDI. [39,60] It is the functionalization of the PDI to achieve specific photophysical properties which makes PDIs so attractive for EC devices and other technologies, as the individual photophysical properties of the PDI should be imparted onto the photophysical properties of the technology which they make up.

To add to the body of knowledge on PDIs and potential PDI based EC devices and other technologies, we have completed two different studies involving functionalized PDIs. In the first study, we synthesized three derivatives of a Thio-PDI, **1,6-**, **1,7-**, and **1,6,7-Thio-PDI**. The **1,6-**,

1,7-, and **1,6,7-Thio-PDI**s were synthesized and isolated to observe if different derivatives displayed different photophysical properties similar to what had already been reported in literature between different 1,6- and 1,7- PDI regioisomers. We concluded that the **1,6-**, **1,7-**, and **1,6,7-Thio-PDI**s exhibited varying photophysical properties such as Stokes shift, quantum yield, excited state lifetimes, differing reversible reduction potentials, different colors observed with reduced states, differing ground to excited state dipole moments, and different excited state properties as determined by density functional theory (DFT). These conclusions are important as there currently exists only a handful of publications which describe the different photophysical properties of 1,6- and 1,7- regioisomers and derivatives. With the **1,6-**, **1,7-**, and **1,6,7-Thio-PDI**s we are contributing to a body of work on derivatives, isomers, and regioisomers of varying PDIs. This body of work is important because the unique photophysical properties of PDI regioisomers and derivatives allows for more flexibility in the design of technologies which utilize these PDI materials. Differing reversible reduction potentials and different colors observed with reduced states make PDIs attractive in EC devices which require both intense color at different reduced or oxidized states, and reversibility. Aside from EC devices, PDIs have also been cited in photovoltaic, chemical switching devices, optoelectronic devices, photovoltaic cells, gas sensing devices, display devices, smart-windows, and EC mirrors.[145,164–167]

The second study involved the synthesis of a p-(t-butyl)phenol with phenylacetylene imide functionality (**PhO-Ph-PDI**) and **mestylene linker** were synthesized for the multilayer fabrication of the **PhO-Ph-PDI** thin-film EC material. **PhO-Ph-PDI** thin-film was grown with **mestylene linker** to form five uniform and ordered bilayers using Copper-Azide Alkyne Cycloaddition (CuAAC) click reaction[102] to assemble via layer-by-layer (LbL) alternating layers on an ITO. The thin-film exhibited H-type aggregation with closely packed molecular assemblies on the ITO.

The electrochemical properties of the **PhO-Ph-PDI** thin-film were observed through several methods including chemical reduction, and cyclic voltammetry (CV), spectroelectrochemistry, and potential step spectroelectrochemistry. The chemical reduction of the **PhO-Ph-PDI** in solution indicated a clean conversion between a neutral, singly reduced, and doubly reduced states can be achieved with three distinct corresponding color changes for each state. In comparison, CVs of the **PhO-Ph-PDI** thin-film in two different sized electrolytes, $TBAPF_6$ or the $TMeAPF_6$, showed that clean conversion to the singly or doubly reduced state was not achieved for either electrolyte. Instead, percent conversions were calculated from the CV data and it was determined that only 3 % conversion was achieved for both mixed states in which ~ 97 % in acetonitrile. However, this percent conversion went up to 6 % for $TBAPF_6$ in a less polar methylene chloride. CV studies of the **PhO-Ph-PDI** thin-films determined that clean conversions to reduced states may increase for less polar solvents like methylene chloride. In comparison to CVs, spectroelectrochemistry and potential step spectroelectrochemistry allowed for full conversion to the doubly reduced state for the $TMeAPF_6$ electrolyte, unlike the partial conversion for the larger $TBuAPF_6$. Additionally potential step spectroelectrochemistry showed that the thin-films were relatively stable throughout the potential jumps as no degradation was observed in the corresponding absorbance or current data. However, like the spectroelectrochemical data, the potential step spectroelectrochemistry showed that there is not a clean conversion to the singly reduced state for either the smaller $TMeAPF_6$ electrolyte, or the larger $TBuAPF_6$. For both electrolytes, when switching from potentials associated with the neutral and doubly reduced to the singly reduced potential, there is an observed gradual decay in the current or gradual increase in the absorbance. These results indicate a mixed reduced state or the possible brief formation of the singly reduced state while between the neutral and more stable doubly reduced state.

As a whole, **PhO-Ph-PDI** thin-film as an EC device requires the meeting a few criteria. As an EC device, the **PhO-Ph-PDI** thin-film should exhibit intense colors when switching between neutral and reduced states. The EC thin-film should rapidly switch between the different neutral and reduced states and exhibit an immediate color change. The EC thin-film should also maintain stability over time without any degradation in color or consumer utility. The **PhO-Ph-PDI** can achieve three distinct colors associated with the neutral, singly reduced, and doubly reduced state in solution which underlies its potential use in EC devices. However, the inability to fully reduce the **PhO-Ph-PDI** film to the singly reduced state really reduces the real-world utility of this device if only two out of the three switching states can be achieved. One potential possibility is that the structure of the **PhO-Ph-PDI** thin-film may have the molecular assemblies packed too closely together to allow effective cation penetration. In conclusion, the use of PDIs in EC technologies for reducing energy consumption and improving global energy security, is far from immediate, but given the functionalization of the bay position to tailor the photophysics, and the intense corresponding colors which they exhibit relative to other chromophores, PDIs are still a fascinating potential avenue to research. If solubility and the structures of the PDI based thin-films can be optimized to allow electrolyte penetration, then PDIs have a wide variety of potential applications in EC devices and other emerging technologies.

6. FUTURE STUDIES

PDIs have exceptional chemical, photo, thermal stability,[33]high tinctorial strength,[34] and functionalization of the bay position fine tunes the photophysical properties of the PDI. [39,60] However PDIs, and other small organic redox molecules are known to have stability issues within devices due to their small size.[31] Additionally, it was determined that the **PhO-Ph-PDI** thin-film was potentially too tightly packed as a molecular assembly for even the smallest electrolyte, $TMeAPF_6$, to effectively penetrate and reduce the thin-film fully. This lack of penetration of the thin-film led to partial reduction of the thin-film instead of clean reductions from the neutral, to singly reduced, to double reduced state. Immediate improvements to this project would first involve a more ordered and less tightly packed molecular assembly which can allow electrolyte penetration more readily.

One potential method to improve ordering and allow for better electrolyte penetration would be through fabricating PDIs within larger structures such as polymers or metal organic complexes instead of small organic redox molecules. As previously discussed, every EC technology has its advantages and disadvantages whether the EC device is fabricated from inorganic, polymer, metal organic complexes, or small organic complexes. Recall that inorganic materials exhibit excellent photostability but lack intense coloration and exhibit a slow response speed when switching.[28] Comparatively, polymers are easy to fabricate through solution processing techniques but it is difficult to achieve spectral purity, which limits their intense coloration within devices. [29,30]

An example of combining PDIs with a larger structure involves the fabrication of robust polyimide film onto a conductive ITO surface from a solution of bis(triphenylamine) perylene diimide by electrochemical polymerization by Hsaio et. al.[168] This

thin-film was able to undergo reversible oxidation and reduction processes and achieve excellent coloration and good cycling stability over many oxidation and reduction cycles. The triphenylamine (TPA) was selected in this thin-film as TPA is an electron rich, hole majority carrier in optoelectronics,[169] which can easily be oxidized to form stable radical cations if the para position on the phenyl ring is protected with an electron withdrawing group[170] such as a PDI. Thus, Hsaio et. al. were able to protect TPA from undergoing the formation of unstable radicals with the use of PDI attachment, while the electrochemical polymerization provided a facile method to directly synthesize and fabricate the polymer thin-film on the electrochemically active surface. The use of the PDI to stabilize the reduction and oxidation process of the EC thin-film, and the polymerization technique to form facile and stable thin-films are one example of fabricating PDIs within larger structures to overcome some of the thin-film assembly disorder of the PDI while imbuing the device with the desirable characteristics of the PDI such as color and functionalization to achieve specific photophysical properties.

REFERENCES

1. Brown, M. A.; Sovacool, B. K. *Climate Change and Global Energy Security: Technology and Policy Options*; The MIT Press, 2011.
2. UN/DESA. *World Population Prospects 2017 – Data Booklet*; 2017.
3. Moriarty, P.; Honnery, D. What Is the Global Potential for Renewable Energy ? *Renew. Sustain. Energy Rev.* **2012**, *16* (1), 244–252. DOI: 10.1016/j.rser.2011.07.151.
4. U.S. Energy Information Administration. *How Much of U.S. Energy Consumption and Electricity Generation Comes From Renewable Energy Sources?* USEIA. https://www.eia.gov/tools/faqs/faq.php?id=92&t=4#:~:text=How much of U.S. energy,total utility-scale electricity generation. (accessed 2023-05-05)
5. DeSilver, D. *Renewable Energy Is Growing Fast in the U.S., but Fossil Fuels Still Dominate*. Pew Research Center. https://www.pewresearch.org/fact-tank/2020/01/15/renewable-energy-is-growing-fast-in-the-u-s-but-fossil-fuels-still-dominate/.(accessed 2023-05-05)
6. Mortimer, R. J.; Rosseinsky, D. R.; Monk, P. M. S. *Electrochromic Materials and Devices*; John Wiley & Sons, Ltd, 2015.
7. Casini, M. Smart Windows for Energy Efficiency of Buildings. *Int. J. Civ. Struct. Eng.* **2015**, *2* (1), 230–238. DOI:10.15224/ 978-1-63248-030-9-56.
8. Delmastro, C.; Bienassis, T. De; Goodson, T.; Lane, K.; Marois, J.-B. Le; Martinez-Gordon, R.; Husek, M. *Buildings: Sectorial Overview*; IEA. (accessed 2022-05-01).
9. Gu, C.; Jia, A. B.; Zhang, Y. M.; Zhang, S. X. A. Emerging Electrochromic Materials and Devices for Future Displays. *Chem. Rev.* **2022**, *122* (18), 14679–14721. DOI:10.1021/acs.chemrev.1c01055.
10. Wu, W.; Wu, L.; Ma, H.; Wu, L.; Wang, H.; Fang, H. Electrochromic Devices Constructed with Water-in-Salt Electrolyte Enabling Energy-Saving and Prolonged Optical Memory Effect. *Chem. Eng. J.* **2022**, *446*, 137122. DOI:10.1016/j.cej.2022.137122.
11. Yuk, S. B.; Lee, W.; Kim, S. H.; Namgoong, J. W.; Lee, J. M.; Kim, J. P. Application of Perylene Dyes for Low Dielectric Hybrid-Type Black Matrices. *J. Ind. Eng. Chem.* **2018**, *64*, 237–244. DOI:10.1016/j.jiec.2018.03.021.
12. Han, M. J.; Khang, D.-Y. Glass and Plastics Platforms for Foldable Electronics and Displays. *Adv. Mater.* **2015**, *27* (34), 4969–4974.
13. Huang, Y.; Liao, S.; Ren, J.; Khalid, B.; Peng, H.; Wu, H. A Transparent, Conducting Tape for Flexible Electronics. *Nano Res.* **2016**, *9* (4), 917–924. DOI:10.1007/s12274-015-0974-9.
14. Kwon, S.; Hwang, Y. H.; Nam, M.; Chae, H.; Lee, H. S.; Jeon, Y.; Lee, S.; Kim, C. Y.; Choi, S.; Jeong, E. G.; Choi, K. C. Recent Progress of Fiber Shaped Lighting Devices for Smart Display Applications—A Fibertronic Perspective. *Adv. Mater.* **2020**, *32* (5), 1–25. DOI:10.1002/adma.201903488.
15. Wang, C.; Jiang, X.; Cui, P.; Sheng, M.; Gong, X.; Zhang, L.; Fu, S. Multicolor and Multistage Response Electrochromic Color-Memory Wearable Smart Textile and Flexible Display. *ACS Appl. Mater. Interfaces* **2021**, *13* (10), 12313–12321. DOI:10.1021/acsami.1c01333.
16. Bange, K. Colouration of Tungsten Oxide Films: A Model for Optically Active Coatings. *Sol. Energy Mater. Sol. Cells* **1999**, *58* (1), 1–131.

17. Li, R.; Ma, X.; Li, J.; Cao, J.; Gao, H.; Li, T.; Zhang, X.; Wang, L.; Zhang, Q.; Wang, G.; Hou, C.; Li, Y.; Palacios, T.; Lin, Y.; Wang, H.; Ling, X. Flexible and High-Performance Electrochromic Devices Enabled by Self-Assembled 2D TiO2/MXene Heterostructures. *Nat. Commun.* **2021**, *12* (1), 1–11. DOI:10.1038/s41467-021-21852-7.
18. Cai, G.; Wang, X.; Cui, M.; Darmawan, P.; Wang, J.; Eh, A. L.; Lee, P. S. Electrochromo-Supercapacitor Based on Direct Growth of NiO Nanoparticles. *Nano Energy* **2015**, *12*, 258–267. DOI:10.1016/j.nanoen.2014.12.031.
19. Kirchmeyer, S.; Reuter, K. Scientific Importance , Properties and Growing Applications of Poly(3,4-Ethylenedioxythiophene). *J. Mater. Chem.* **2005**, *15* (21), 2077–2088. DOI:10.1039/b417803n.
20. Thompson, B. C.; Kim, Y.; Mccarley, T. D.; Reynolds, J. R. Soluble Narrow Band Gap and Blue Propylenedioxythiophene-Cyanovinylene Polymers as Multifunctional Materials for Photovoltaic and Electrochromic Applications. *J. Am. Chem. Soc.* **2006**, *128*, 12714–12725.
21. Gunbas, G.; Toppare, L. Electrochromic Conjugated Polyheterocycles and Derivatives — Highlights from the Last Decade towards Realization of Long Lived Aspirations. *Chem. Commun.* **2012**, *48*, 1083–1101. DOI:10.1039/c1cc14992j.
22. Argazzi, R.; Yukie, N.; Iha, M.; Zabri, H.; Odobel, F.; Bignozzi, C. A. Design of Molecular Dyes for Application in Photoelectrochemical and Electrochromic Devices Based on Nanocrystalline Metal Oxide Semiconductors. *Coord. Chem. Rev.* **2004**, *248*, 1299–1316. DOI:10.1016/j.ccr.2004.03.026.
23. Takada, K.; Sakamoto, R.; Yi, S.; Katagiri, S.; Kambe, T.; Nishihara, H. An Electrochromic Bis (Terpyridine) Metal Complex Nanosheet. *J. Am. Chem. Soc.* **2015**, *137* (14), 4681–4689.
24. Kanagaraj, M.; Velayutham, D.; Suryanarayanan, V.; Kathiresan, M.; Ho, K.-C. Viologen Based Electrochromic Materials and Devices M. *J. Mater. Chem. C* **2019**, *7* (16), 4622–4637. DOI:10.1039/C9TC00416E.
25. Kanazawa, K.; Nakamura, K.; Kobayashi, N. Electroswitchable Optical Device Enabling Both Luminescence and Coloration Control Consisted of Fluoran Dye and 1,4-Benzoquinone. *Sol. Energy Mater. Sol. Cells* **2016**, *145*, 42–53. DOI:10.1016/j.solmat.2015.06.061.
26. Li, J.; Li, J.; Li, H.; Wang, C.; Sheng, M.; Zhang, L.; Fu, S. Bistable Elastic Electrochromic Ionic Gels for Energy-Saving Displays. *Appl. Mater. Interfaces* **2021**, *13*, 27200–27208. DOI:10.1021/acsami.1c05768.
27. Zhang, E.; Liu, L.; Lv, F.; Wang, S. Design and Synthesis of Reactive Perylene Tetracarboxylic Diimide Derivatives for Rapid Cell Imaging. *ACS Omega* **2018**, *3* (8), 8691–8696. DOI:10.1021/acsomega.8b01275.
28. Wu, W.; Wang, M.; Ma, J.; Cao, Y.; Deng, Y. Electrochromic Metal Oxides: Recent Progress and Prospect. *Adv. Electron. Mater.* **2018**, *4* (8), 1800185. DOI:10.1002/aelm.201800185.
29. Amb, C. M.; Dyer, A. L.; Reynolds, J. R. Navigating the Color Palette of Solution-Processable Electrochromic Polymers. *Chem. Mater.* **2011**, *23*, 397–415. DOI:10.1021/cm1021245.
30. Yen, H.-J.; Liou, G. Recent Advances in Triphenylamine-Based Electrochromic Derivatives and Polymers. *Polym. Chem.* **2018**, *9* (22), 3001–3018.
31. Shah, K. W.; Wang, S.-X.; Soo, D. X. Y.; Xu, J. Viologen-Based Electrochromic

Materials : From Small Molecules , Polymers and Composites to Their Applications. *Polymers (Basel)*. **2019**, *11* (11). 1839.
32. Huang, C.; Barlow, S.; Marder, S. R. Perylene-3,4,9,10-Tetracarboxylic Acid Diimides: Synthesis, Physical Properties, and Use in Organic Electronics. *J. Org. Chem.* **2011**, *76* (8), 2386–2407. DOI:10.1021/jo2001963.
33. Würthner, F. Perylene Bisimide Dyes as Versatile Building Blocks for Functional Supramolecular Architectures. *Chem. Commun.* **2004**, *4* (14), 1564–1579. DOI:10.1039/b401630k.
34. Herbst, W.; Ed, K. H. *Industrial Organic Pigments: Production, Properties, Applications*, 2nd ed.; WILEY-VCH: Weinheim, 1997.
35. Margineanu, A.; Hofkens, J.; Cotlet, M.; Habuchi, S.; Stefan, A.; Qu, J.; Kohl, C.; Mu, K.; Vercammen, J.; Engelborghs, Y.; Gensch, T.; Schryver, F. C. De. Photophysics of a Water - Soluble Rylene Dye : Comparison with Other Fluorescent Molecules for Biological Applications. *J. Phys. Chem. B* **2004**, *108* (32), 12242–12251. DOI:10.1021/jp048051w.
36. Jung, M.; Smoother, T.; Martin, A. A.; Mcdonagh, A. M.; Maynard, P. J.; Lennard, C.; Roux, C. Fluorescent TiO 2 Powders Prepared Using a New Perylene Diimide Dye : Applications in Latent Fingermark Detection. *Forensic Sci. Int.* **2007**, *173* (2–3), 154–160. DOI:10.1016/j.forsciint.2006.09.014.
37. Rappold, M.; Warttinger, U.; Krämer, R. A Fluorescent Probe for Glycosaminoglycans Applied to the Detection of Dermatan Sulfate by a Mix-and-Read Assay. *Mol.* **2017***, 22* (5), 768. DOI:10.3390/MOLECULES22050768.
38. (38) Yukruk, F.; Dogan, A. L.; Canpinar, H.; Guc, D.; Akkaya, E. U. Water-Soluble Green Perylenediimide (PDI) Dyes as Potential Sensitizers for Photodynamic Therapy. *Org. Lett.* **2005**, *7* (14), 2885–2887. DOI:10.1021/ol050841g.
39. Würthner, F.; Nowak-Król, A. Progress in the Synthesis of Perylene Bisimide Dyes. *Org. Chem. Front.* **2019**, *6*, 1272–1318. DOI:10.1039/c8qo01368c.
40. Lee, S. K.; Zu, Y.; Herrmann, A.; Geerts, Y.; Bard, A. J.; December, R. V; Müllen, K.; Bard, A. J. Electrochemistry, Spectroscopy and Electrogenerated Chemiluminescence of Perylene, Terrylene, and Quaterrylene Diimides in Aprotic Solution. *J. Am. Chem. Soc.* **1999**, *121* (14), 3513–3520. DOI:10.1021/ja984188m.
41. Tintori, F.; Laventure, A.; Welch, G. C. Perylene Diimide Based Organic Photovoltaics with Slot-Die Coated Active Layers from Halogen-Free Solvents in Air at Room Temperature. *ACS Appl. Mater. Interfaces* **2019**, *11* (42), 39010–39017. DOI:10.1021/acsami.9b14251.
42. Qin, R.; Guo, D.; Li, M.; Li, G.; Bo, Z.; Wu, J. Perylene Monoimide Dimers Enhance Ternary Organic Solar Cells Efficiency by Induced D-A Crystallinity. *ACS Appl. Energy Mater.* **2019**, *2* (1), 305–311. DOI:10.1021/acsaem.8b01320.
43. Kozma, E.; Catellani, M. Perylene Diimides Based Materials for Organic Solar Cells. *Dye. Pigment.* **2013**, *98* (1), 160–179. DOI:10.1016/j.dyepig.2013.01.020.
44. Keum, C.; Becker, D.; Archer, E.; Bock, H.; Kitzerow, H.; Gather, M. C.; Murawski, C. Organic Light-Emitting Diodes Based on a Columnar Liquid-Crystalline Perylene Emitter. *Adv. Opt. Mater.* **2020**, *8* (17), 2000414. DOI:10.1002/adom.202000414.
45. Li, G.; Zhao, Y.; Li, J.; Cao, J.; Zhu, J.; Sun, X. W.; Zhang, Q. Synthesis, Characterization, Physical Properties, and OLED Application of Single BN-Fused Perylene Diimide. *J. Org. Chem.* **2015**, *80* (1), 196–203. DOI:10.1021/jo502296z.

46. Ahrens, M. J.; Sinks, L. E.; Rybtchinski, B.; Liu, W.; Jones, B. A.; Giaimo, J. M.; Gusev, A. V.; Goshe, A. J.; Tiede, D. M.; Wasielewski, M. R. Self-Assembly of Supramolecular Light-Harvesting Arrays from Covalent Multi-Chromophore Perylene-3,4:9,10-Bis(Dicarboximide) Building Blocks. *J. Am. Chem. Soc.* **2004**, *126* (26), 8284–8294. DOI:10.1021/ja039820c.
47. Inan, D.; Dubey, R. K.; Jager, W. F.; Grozema, F. C. Tailoring Photophysical Processes of Perylene-Based Light Harvesting Antenna Systems with Molecular Structure and Solvent Polarity. *J. Phys. Chem. C* **2019**, *123* (1), 36–47. DOI:10.1021/acs.jpcc.8b08503.
48. Beauvilliers, E. E.; Topka, M. R.; Dinolfo, P. H. Synthesis and Characterization of Perylene Diimide Based Molecular Multilayers Using CuAAC: Towards Panchromatic Assemblies. *RSC Adv.* **2014**, *4* (62), 32866. DOI:10.1039/C4RA04512B.
49. Zhang, B.; Soleimaninejad, H.; Jones, D. J.; White, J. M.; Ghiggino, K. P.; Smith, T. A.; Wong, W. W. H. Highly Fluorescent Molecularly Insulated Perylene Diimides: Effect of Concentration on Photophysical Properties. *Chem. Mater.* **2017**, *29* (19), 8395–8403. DOI:10.1021/acs.chemmater.7b02968.
50. Zhang, B.; Zhao, P.; Wilson, L. J.; Subbiah, J.; Yang, H.; Mulvaney, P.; Jones, D. J.; Ghiggino, K. P.; Wong, W. W. H. High-Performance Large-Area Luminescence Solar Concentrator Incorporating a Donor-Emitter Fluorophore System. *ACS Energy Lett.* **2019**, *4* (8), 1839–1844. DOI:10.1021/acsenergylett.9b01224.
51. Ahrens, M. J.; Fuller, M. J.; Wasielewski, M. R. Cyanated Perylene-3,4-Dicarboximides and Perylene-3,4:9,10-Bis(Dicarboximide): Facile Chromophoric Oxidants for Organic Photonics and Electronics. *Chem. Mater.* **2003**, *15* (14), 2684–2686. DOI:10.1021/cm034140u.
52. Zhan, X.; Tan, Z.; Domercq, B.; An, Z.; Zhang, X.; Barlow, S.; Li, Y.; Zhu, D.; Kippelen, B.; Marder, S. R. A High-Mobility Electron-Transport Polymer with Broad Absorption and Its Use in Field-Effect Transistors and All-Polymer Solar Cells. *J. Am. Chem. Soc.* **2007**, *129* (23), 7246–7247. DOI:10.1021/ja071760d.
53. Zafer, C.; Kus, M.; Turkmen, G.; Dincalp, H.; Demic, S.; Kuban, B.; Teoman, Y.; Icli, S. New Perylene Derivative Dyes for Dye-Sensitized Solar Cells. *Sol. Energy Mater. Sol. Cells* **2007**, *91* (5), 427–431. DOI:10.1016/j.solmat.2006.10.004.
54. Erten-Ela, S.; Turkmen, G. Perylene Imide Dyes for Solid-State Dye-Sensitized Solar Cells: Spectroscopy, Energy Levels and Photovoltaic Performance. *Renew. Energy* **2011**, *36* (6), 1821–1825. DOI:10.1016/j.renene.2010.11.025.
55. Shibano, Y.; Umeyama, T.; Matano, Y.; Imahori, H. Electron-Donating Perylene Tetracarboxylic Acids for Dye-Sensitized Solar Cells. *Org. Lett.* **2007**, *9* (10), 1971–1974. DOI:10.1021/ol070556s.
56. Yao, J.; Qiu, B.; Zhang, Z.; Xue, L.; Wang, R.; Zhang, C.; Chen, S.; Zhou, Q.; Sun, C.; Yang, C.; Xiao, M.; Meng, L.; Li, Y. Cathode Engineering with Perylene-Diimide Interlayer Enabling over 17% Efficiency Single-Junction Organic Solar Cells. *Nat. Commun.* **2020**, *11* (1), 1–10. DOI:10.1038/s41467-020-16509-w.
57. Herbst, W.; Hunger, K.; Gerhard, W.; Ohlier, H.; Winter, R. *Indutrial Organic Pigments Production, Properties, Applications*, 3rd. ed; WILEY-VCH Verlag GmbH & Co. KGaA, Weinheim, 2004.
58. Herbst, W.; Hunger, K. *Industrial Organic Pigments*; WILEY-VCH Verlag GmbH & Co. KGaA: Weinheim, 2004.
59. Vura-Weis, J.; Ratner, M. A.; Wasielewski, M. R. Geometry and Electronic Coupling in

Perylenediimide Stacks: Mapping Structure - Charge Transport Relationships. *J. Am. Chem. Soc.* **2010**, *132* (6), 1738–1739. DOI:10.1021/ja907761e.
60. Huang, C.; Barlow, S.; Marder, S. R. Perylene-3,4,9,10-Tetracarboxylic Acid Diimides: Synthesis, Physical Properties, and Use in Organic Electronics. *J. Org. Chem.* **2011**, *76* (8), 2386–2407. DOI:10.1021/jo2001963.
61. McMurry, J. *Organic Chemistry*, 9th ed.; Cengage Learning, 2015.
62. Seybold, G.; Wagenblast, G. New Perylene and Violanthrone Dyestuffs for Fluorescent Collectors. *Dye. Pigment.* **1989**, *11* (4), 303–317.
63. Sadrai, M.; Hadel, L.; Sauers, R. R.; Husain, S.; Krogh-Jespersen, K.; Westbrook, J. D.; Bird, G. R. Lasing Action in a Family of Peryiene Derivatives: Singlet Absorption and Emission Spectra, Triplet Absorption and Oxygen Quenching Constants, and Molecular Mechanlcs and Semiempirical Molecular Orbital Calculations. *J. Phys. Chem.* **1992**, *96* (20), 7988–7996. DOI:/10.1021/j100199a032.
64. Böhm, A.; Arms, H.; Henning, G.; Blaschka, P. 1,7-Diaroxy-or -Arylthio-Substituted Perylene-3,4,9,10-Tetracarboxylic Acids, Their Dianhydrides and Diimides. DE19547209A1, 1997.
65. Nowak-Król, A.; Würthner, F. Progress in the Synthesis of Perylene Bisimide Dyes. *Org. Chem. Front.* **2019**, *6* (8), 1272–1318. DOI:10.1039/c8qo01368c.
66. Osswald, P.; Würthner, F. Effects of Bay Substituents on the Racemization Barriers of Perylene Bisimides: Resolution of Atropo-Enantiomers. *J. Am. Chem. Soc.* **2007**, *129* (46), 14319–14326.
67. Schnurpfeil, G.; Stark, J.; Whrle, D. Syntheses of Uncharged , Positively and Negatively Charged 3,4,9,10-Perylene-Bis(Dicarboximides). *Dye. Pigment.* **1995**, *27* (4), 339–350.
68. Langhals, H. Control of the Interactions in Multichromophores: Novel Concepts. Perylene Bis-Imides as Components for Larger Functional Units. *Helv. Chim. Acta* **2005**, *88* (6), 1309–1343. DOI:10.1002/hlca.200590107.
69. Demming, S.; Langhals, H. Leichtlösliche, lichtechte Perylen-Fluoreszenzfarbstoffe. *Chem. Ber* **1988**, *121*. 225-230.
70. (70) Wu, X.; Yin, C.; Shi, Z.; Xu, M.; Zhang, J.; Sun, J. A Novel Substitution Reaction of Perylene Bisimides with Ph2PLi at the α-Position. *New J. Chem.* **2010**, *34*, 61–64. DOI:10.1039/b9nj00364a.
71. Schmidt, D.; Bialas, D.; Würthner, F. Ambient Stable Zwitterionic Perylene Bisimide-Centered Radical Angewandte. *Angew. Chemie - Int. Ed.* **2015**, *54* (12), 3611–3614. DOI:10.1002/anie.201408067.
72. Würthner, F.; Stepanenko, V.; Chen, Z.; Saha-Möller, C. R.; Kocher, N.; Stalke, D. Preparation and Characterization of Regioisomerically Pure 1,7-Disubstituted Perylene Bisimide Dyes. *J. Org. Chem.* **2004**, *69* (23), 7933–7939. DOI:10.1021/jo048880d.
73. Dubey, R. K.; Efimov, A.; Lemmetyinen, H. 1,7-And 1,6-Regioisomers of Diphenoxy and Dipyrrolidinyl Substituted Perylene Diimides: Synthesis, Separation, Characterization, and Comparison of Electrochemical and Optical Properties. *Chem. Mater.* **2011**, *23* (3), 778–788. DOI:10.1021/cm1018647.
74. Fan, L.; Xu, Y.; Tian, H. 1,6-Disubstituted Perylene Bisimides: Concise Synthesis and Characterization as near-Infrared Fluorescent Dyes. *Tetrahedron Lett.* **2005**, *46* (26), 4443–4447. DOI:10.1016/j.tetlet.2005.04.137.
75. Dey, S.; Efimov, A.; Lemmetyinen, H. Diaryl-Substituted Perylene Bis(Imides): Synthesis, Separation, Characterization and Comparison of Electrochemical and Optical

Properties of 1,7-and 1,6-Regioisomer. *European J. Org. Chem.* **2012**, *2012* (12), 2367–2374. DOI:10.1002/ejoc.201101825.
76. Kozma, E.; Mróz, W.; Andicsová Eckstein, A.; Lukeš, V.; Galeotti, F.; Šišková, A.; Danko, M.; Catellani, M. A Joint Experimental and Theoretical Study on the Electro-Optical Properties of 1,6- and 1,7-Fluorenyl Disubstituted Perylene Diimide Isomers. *New J. Chem.* **2018**, *42* (2), 1061–1066. DOI:10.1039/c7nj03860g.
77. Handa, N. V; Mendoza, K. D.; Shirtcliff, L. D. Syntheses and Properties of 1,6 and 1,7 Perylene Diimides and Tetracarboxylic Dianhydrides. *Org. Lett.* **2011**, *13* (17), 4724–4727. DOI:10.1021/ol2019407.
78. Slater, A. G.; Stephen Davies, E.; Argent, S. P.; Lewis, W.; Blake, A. J.; Mcmaster, J.; Champness, N. R. Bis-Thioether-Substituted Perylene Diimides: Structural, Electrochemical, and Spectroelectrochemical Properties. *J. Org. Chem.* **2013**, *78* (7), 2853−2862. DOI:10.1021/jo400026r.
79. Kosugi, M.; Shimizu, T.; Migita, T. Reactions Of Aryl Halides With Thiolate Anions In The Presence Of Catalytic Amounts Of Tetrakis(Triphenylphosphine)Palladium Preparation Of Aryl Sulfides. *Chem. Lett.* **1978**, *7* (1), 13–14.
80. Dey, S.; Efimov, A.; Lemmetyinen, H. Diaryl-Substituted Perylene Bis (Imides): Synthesis, Separation, Characterization and Comparison of Electrochemical and Optical Properties of 1 , 7- and 1 , 6-Regioisomer. *Euroopean J. Org. Chem.* **2012**, *2012* (12), 2367–2374. DOI:10.1002/ejoc.201101825.
81. Palomaki, P. K. B.; Dinolfo, P. H. A Versatile Molecular Layer-by-Layer Thin Film Fabrication Technique Utilizing Copper(I)-Catalyzed Azide-Alkyne Cycloaddition. *Langmuir* **2010**, *26* (12), 9677–9685. DOI:10.1021/la100308j.
82. Creager, S. Self-Assembled Monolayer Films: Electrochemical Properties. *Encycl. Mater. Sci. Technol.* **2001**, 8299–8304. DOI:10.1016/b0-08-043152-6/01485-6.
83. Aswal, D. K.; Lenfant, S.; Guerin, D.; Yakhmi, J. V.; Vuillaume, D. Self Assembled Monolayers on Silicon for Molecular Electronics. *Anal. Chim. Acta* **2006**, *568* (1–2), 84–108. DOI:10.1016/j.aca.2005.10.027.
84. Chaki, N. K.; Vijayamohanan, K. Self-Assembled Monolayers as a Tunable Platform for Biosensor Applications. *Biosens. Bioelectron.* **2002**, *17* (1–2), 1–12. DOI:10.1016/S0956-5663(01)00277-9.
85. Paniagua, S. A.; Giordano, A. J.; Smith, O. L.; Barlow, S.; Li, H.; Armstrong, N. R.; Pemberton, J. E.; Brédas, J. L.; Ginger, D.; Marder, S. R. Phosphonic Acids for Interfacial Engineering of Transparent Conductive Oxides. *Chem. Rev.* **2016**, *116* (12), 7117–7158. DOI:10.1021/acs.chemrev.6b00061.
86. Haensch, C.; Hoeppener, S.; Schubert, U. S. Chemical Modification of Self-Assembled Silane Based Monolayers by Surface Reactions. *Chem. Soc. Rev.* **2010**, *39* (6), 2323–2334. DOI:10.1039/b920491a.
87. Gardner, T. J.; Frisbie, C. D.; Wrighton, M. S. Systems for Orthogonal Self-Assembly of Electroactive Monolayers on Au and ITO: An Approach to Molecular Electronics. *J. Am. Chem. Soc.* **1995**, *117* (26), 6927–6933.
88. Vercelli, B.; Zotti, G.; Schiavon, G.; Zecchin, S. Adsorption of Hexylferrocene Phosphonic Acid on Indium-Tin Oxide Electrodes. Evidence of StrongInterchain Interactions in Ferrocene Self-Assembled Monolayers. *Langmui* **2003**, *19* (22), 9351–9356.
89. Palomaki, P. K. B.; Civic, M. R.; Dinolfo, P. H. Photocurrent Enhancement by

Multilayered Porphyrin Sensitizers in a Photoelectrochemical Cell. *ACS Appl. Mater. Interfaces* **2013**, *5* (15), 7604–7612. DOI:10.1021/am401923f.
90. Civic, M. R.; Dinolfo, P. H. Electrochemical Rectification of Redox Mediators Using Porphyrin-Based Molecular Multilayered Films on ITO Electrodes. *ACS Appl. Mater. Interfaces* **2016**, *8* (31), 20465–20473. DOI:10.1021/acsami.6b05643.
91. Betz, U.; Kharrazi Olsson, M.; Marthy, J.; Escolá, M. F.; Atamny, F. Thin Films Engineering of Indium Tin Oxide: Large Area Flat Panel Displays Application. *Surf. Coatings Technol.* **2006**, *200* (20–21), 5751–5759. DOI:10.1016/j.surfcoat.2005.08.144.
92. Georgieva, V.; Ristov, M. Electrodeposited Cuprous Oxide on Indium Tin Oxide for Solar Applications. *Sol. Energy Mater. Sol. Cells* **2002**, *73* (1), 67–73. DOI:10.1016/S0927-0248(01)00112-X.
93. Yu, S. Y.; Chang, J. H.; Wang, P. S.; Wu, C. I.; Tao, Y. T. Effect of ITO Surface Modification on the Oled Device Lifetime. *Langmuir* **2014**, *30* (25), 7369–7376. DOI:10.1021/la4049659.
94. Meldal, M.; Tornøe, C. W. Cu-Catalyzed Azide - Alkyne Cycloaddition. *Chem. Rev.* **2008**, *108* (8), 2952–3015. DOI:10.1021/cr0783479.
95. Wang, Z.; Qin, H. Regioselective Synthesis of 1,2,3-Triazole Derivatives via 1,3-Dipolar Cycloaddition Reactions in Water†. *Chem. Commun.* **2003**, *2* (19), 2450–2451.
96. Harju, K.; Vesterinen, J.; Yli-Kauhaluoma, J. Solid-Phase Synthesis of Amino Acid Derived N-Unsubstituted Pyrazoles via Sydnones. *Org. Lett.* **2009**, *11* (10), 2219–2221. DOI:10.1021/ol900704b.
97. Molteni, G.; Ponti, A. Arylazide Cycloaddition to Methyl Propiolate: DFT-Based Quantitative Prediction of Regioselectivity. *Chem. - A Eur. J.* **2003**, *9* (12), 2770–2774. DOI:10.1002/chem.200204681.
98. Meldal, M.; Tomøe, C. W. Cu-Catalyzed Azide - Alkyne Cycloaddition. *Chem. Rev.* **2008**, *108* (8), 2952–3015. DOI:10.1021/cr0783479.
99. Meldal, M.; Tomøe, C. W. Peptidotriazoles: Copper (I)-Catalyzed 1,3-Dipolar Cycloadditions on Solid-Phase. In *American Peptide Symposium*; American Peptide Society and Kluwer Academic Publishers: San Diego, 2001; pp 263–264.
100. Chan, T. R.; Hilgraf, R.; Sharpless, K. B.; Fokin, V. V. Polytriazoles as Copper(I)-Stabilizing Ligands in Catalysis. *Org. Lett.* **2004**, *6* (17), 2853–2855. DOI:10.1021/ol0493094.
101. Wu, P.; Fokin, V. V. No Title. *Catalytic azide-alkyne cycloaddition: Reactivity and applications*. **2007**, *40* (7).7-17.
102. Kolb, H. C.; Sharpless, K. B. The Growing Impact of Click Chemistry on Drug Discovery. *Drug Discov. Today* **2003**, *8* (24), 1128–1137. DOI:10.1016/s1936-7961(08)00219-4.
103. Binder, W. H.; Sachsenhofer, R. "Click" Chemistry in Polymer and Materials Science. *Macromol. Rapid Commun.* **2007**, *28* (1), 15–54. DOI:10.1002/marc.200600625.
104. Lutz, J. F. 1,3-Dipolar Cycloadditions of Azides and Alkynes: A Universal Ligation Tool in Polymer and Materials Science. *Angew. Chemie - Int. Ed.* **2007**, *46* (7), 1018–1025. DOI:10.1002/anie.200604050.
105. Dirks, A. J.; Van Berkel, S. S.; Hatzakis, N. S.; Opsteen, J. A.; Van Delft, F. L.; Cornelissen, J. J. L. M.; Rowan, A. E.; Van Hest, J. C. M.; Rutjes, F. P. J. T.; Nolte, R. J. M. Preparation of Biohybrid Amphiphiles via the Copper Catalysed Huisgen [3 + 2] Dipolar Cycloaddition Reaction. *Chem. Commun.* **2005**, 33, 4172–4174.

DOI:10.1039/b508428h.
106. Collman, J. P.; Devaraj, N. K.; Chidsey, C. E. D. "Clicking" Functionality onto Electrode Surfaces. *Langmuir* **2004**, *20* (4), 1051–1053.
107. Devaraj, N. K.; Miller, G. P.; Ebina, W.; Kakaradov, B.; Collman, J. P.; Kool, E. T.; Chidsey, C. E. D. Chemoselective Covalent Coupling of Oligonucleotide Probes to Self-Assembled Monolayers. *J. Am. Chem. Soc.* **2005**, *127* (24), 8600–8601. DOI:10.1021/ja051462l.
108. Sun, X. L.; Stabler, C. L.; Cazalis, C. S.; Chaikof, E. L. Carbohydrate and Protein Immobilization onto Solid Surfaces by Sequential Diels-Alder and Azide-Alkyne Cycloadditions. *Bioconjug. Chem.* **2006**, *17* (1), 52–57. DOI:10.1021/bc0502311.
109. Luo, L.; Frisbie, C. D. Length-Dependent Conductance of Conjugated Molecular Wires Synthesized by Stepwise "Click" Chemistry. *J. Am. Chem. Soc.* **2010**, *132* (26), 8854–8855. DOI:10.1021/ja103239b.
110. Ku, S. Y.; Wong, K. T.; Bard, A. J. Surface Patterning with Fluorescent Molecules Using Click Chemistry Directed by Scanning Electrochemical Microscopy. *J. Am. Chem. Soc.* **2008**, *130* (8), 2392–2393. DOI:10.1021/ja078183d.
111. Golas, P. L.; Tsarevsky, N. V.; Sumerlin, B. S.; Matyjaszewski, K. Catalyst Performance in "Click" Coupling Reactions of Polymers Prepared by ATRP: Ligand and Metal Effects. *Macromolecules* **2006**, *39* (19), 6451–6457. DOI:10.1021/ma061592u.
112. Malkoch, M.; Thibault, R. J.; Drockenmuller, E.; Messerschmidt, M.; Voit, B.; Russell, T. P.; Hawker, C. J. Orthogonal Approaches to the Simultaneous and Cascade Functionalization of Macromolecules Using Click Chemistry. *J. Am. Chem. Soc.* **2005**, *127* (42), 14942–14949. DOI:10.1021/ja0549751.
113. Gil, M. V.; Arévalo, M. J.; López, Ó. Click Chemistry - What's in a Name? Triazole Synthesis and Beyond. *Synthesis (Stuttg).* **2007**, 11, 1589–1620. DOI:10.1055/s-2007-966071.
114. Helms, B.; Mynar, J. L.; Hawker, C. J.; Fréchet, J. M. J. Dendronized Linear Polymers via "Click Chemistry." *J. Am. Chem. Soc.* **2004**, *126* (46), 15020–15021. DOI:10.1021/ja044744e.
115. Moses, J. E.; Moorhouse, A. D. The Growing Applications of Click Chemistry. *Chem. Soc. Rev.* **2007**, *36* (8), 1249–1262. DOI:10.1039/b613014n.
116. Deiters, A.; Schultz, P. G. In Vivo Incorporation of an Alkyne into Proteins in Escherichia Coli. *Bioorganic Med. Chem. Lett.* **2005**, *15* (5), 1521–1524. DOI:10.1016/j.bmcl.2004.12.065.
117. Beatty, K. E.; Xie, F.; Wang, Q.; Tirrell, D. A. Selective Dye-Labeling of Newly Synthesized Proteins in Bacterial Cells. *J. Am. Chem. Soc.* **2005**, *127* (41), 14150–14151. DOI:10.1021/ja054643w.
118. Speers, A. E.; Adam, G. C.; Cravatt, B. F. Activity-Based Protein Profiling in Vivo Using a Copper(I)-Catalyzed Azide-Alkyne [3 + 2] Cycloaddition. *J. Am. Chem. Soc.* **2003**, *125* (16), 4686–4687. DOI:10.1021/ja034490h.
119. Jagasia, R.; Holub, J. M.; Bollinger, M.; Kirshenbaum, K.; Finn, M. G. Peptide Cyclization and Cyclodimerization by Cu I-Mediated Azide-Alkyne Cycloaddition. *J. Org. Chem.* **2009**, *74* (8), 2964–2974. DOI:10.1021/jo802097m.
120. Li, H.; Cheng, F.; Duft, A. M.; Adronov, A. Functionalization of Single-Walled Carbon Nanotubes with Well-Defined Polystyrene by "Click" Coupling. *J. Am. Chem. Soc.* **2005**, *127* (41), 14518–14524. DOI:10.1021/ja054958b.

121. Bard, A. J.; Faulkner, L. R. *Electrochemical Methods: Fundamentals and Applications*, 2nd ed.; Wiley, 2001.
122. Dubey, R. K.; Efimov, A.; Lemmetyinen, H. 1,7-And 1,6-Regioisomers of Diphenoxy and Dipyrrolidinyl Substituted Perylene Diimides: Synthesis, Separation, Characterization, and Comparison of Electrochemical and Optical Properties. *Chem. Mater.* **2011**, *23* (3), 778–788. DOI:10.1021/cm1018647.
123. Ma, J.; Yin, L.; Zou, G.; Zhang, Q. Regioisomerically Pure 1 , 7-Dibromo-Substituted Perylene Bisimide Dyes : Efficient Synthesis , Separation , and Characterization. *European J. Org. Chem.* **2015**, *2015* (15), 3296–3302. DOI:10.1002/ejoc.201500206.
124. Feng, J.; Wang, D.; Wang, H.; Zhang, D.; Zhang, L.; Li, X. Structural and Property Comparison between the Di-Piperidinyl- and Di-Pyrrolidinyl-Substituted Perylene Tetracarboxylic Diimides. *J. Phys. Org. Chem.* **2011**, *24* (8), 621–629. DOI:10.1002/poc.1799.
125. Handa, N. V; Mendoza, K. D.; Shirtcliff, L. D. Syntheses and Properties of 1,6 and 1,7 Perylene Diimides and Tetracarboxylic Dianhydrides. *Org. Lett.* **2011**, *13* (17), 4724–4727. DOI:10.1021/ol2019407.
126. Riives, A. J.; Huang, Z.; Anderson, N. T.; Dinolfo, P. H. 1,7-, 1,6-, and 1,6,7- Derivatives of Dodecylthio Perylene Diimides: Synthesis, Characterization, and Comparison of Electrochemical and Optical Properties. *J. Photochem. Photobiol. A Chem.* **2023**, *437*, 114441. DOI:10.1016/J.JPHOTOCHEM.2022.114441.
127. Würthner, F.; Stepanenko, V.; Chen, Z.; Saha-Möller, C. R.; Kocher, N.; Stalke, D. Preparation and Characterization of Regioisomerically Pure 1,7-Disubstituted Perylene Bisimide Dyes. *J. Org. Chem.* **2004**, *69* (23), 7933–7939. DOI:10.1021/jo048880d.
128. Dubey, R. K.; Niemi, M.; Kaunisto, K.; Efimov, A.; Tkachenko, N. V.; Lemmetyinen, H. Direct Evidence of Significantly Different Chemical Behavior and Excited-State Dynamics of 1,7- and 1,6-Regioisomers of Pyrrolidinyl-Substituted Perylene Diimide. *Chem. - A Eur. J.* **2013**, *19* (21), 6791–6806. DOI:10.1002/chem.201203387.
129. Liu, Y.; Li, Y.; Jiang, L.; Gan, H.; Liu, H.; Li, Y.; Zhuang, J.; Lu, F.; Zhu, D. Assembly and Characterization of Novel Hydrogen-Bond-Induced Nanoscale Rods. *J. Org. Chem.* **2004**, *69* (26), 9049–9054. DOI:10.1021/jo0486037.
130. Frisch, M. J.; Trucks, G. W.; Schlegel, H. B.; Scuseria, G. E.; Robb, M. A.; Cheeseman, J. R.; Scalmani, G.; Barone, V.; Petersson, G. A.; Nakatsuji, H.; Li, X.; Caricato, M.; Gaussian 09, Revision D.01. 2009.
131. Yanai, T.; Tew, D. P.; Handy, N. C. A New Hybrid Exchange-Correlation Functional Using the Coulomb-Attenuating Method (CAM-B3LYP). *Chem. Phys. Lett.* **2004**, *393* (1–3), 51–57. DOI:10.1016/j.cplett.2004.06.011.
132. Tomasi, J.; Mennucci, B.; Cammi, R. Quantum Mechanical Continuum Solvation Models. *Chem. Rev.* **2005**, *105* (8), 2999–3093. DOI:10.1021/CR9904009.
133. Gagne, R. R.; Koval, C. A.; Lisensky, G. C. Ferrocene as an Internal Standard for Electrochemical Measurements. *Inorg. Chem.* **1980**, *19* (9), 2854–2855.
134. Sens, R.; Drexhage, K. H. Fluorescence Quantum Yield of Oxazine and Carbazine Laser Dyes. *J. Lumin.* **1981**, *24–25* (Part 2), 709–712. DOI:10.1016/0022-2313(81)90075-2.
135. Zhang, X. F.; Zhang, Y.; Liu, L. Fluorescence Lifetimes and Quantum Yields of Ten Rhodamine Derivatives: Structural Effect on Emission Mechanism in Different Solvents. *J. Lumin.* **2014**, *145*, 448–453. DOI:10.1016/j.jlumin.2013.07.066.
136. Lakowicz, J. R. (University of M. S. of M. *Principles of Fluorescence Spectroscopy*, 3rd

ed.; Springer, 2006. DOI:10.1007/978-0-387-46312-4.
137. Chen, K. Y.; Chang, C. W.; Tsai, H. Y. 1,6-and 1,7-Regioisomers of Highly Soluble Amino-Substituted Perylene Tetracarboxylic Dianhydrides: Synthesis, Optical and Electrochemical Properties. *Materials (Basel)*. **2015**, *8* (8), 4943–4960. DOI:10.3390/ma8084943.
138. Ahrens, M. J.; Tauber, M. J.; Wasielewski, M. R. Bis(n-Octylamino)Perylene-3,4:9,10-Bis(Dicarboximide)s and Their Radical Cations: Synthesis, Electrochemistry, and ENDOR Spectroscopy. *J. Org. Chem.* **2006**, *71* (5), 2107–2114. DOI:10.1021/jo052394o.
139. Gosztola, D.; Niemczyk, M. P.; Svec, W.; Lukas, A. S.; Wasielewski, M. R. Excited Doublet States of Electrochemically Generated Aromatic Imide and Diimide Radical Anions. *J. Phys. Chem. A* **2000**, *104* (28), 6545–6551. DOI:10.1021/jp000706f.
140. Zhao, Y.; Wasielewski, M. R. 3,4:9,10-Perylenebis(Dicarboximide) Chromophores That Function as Both Electron Donors and Acceptors. *Tetrahedron Lett.* **1999**, *40* (39), 7047–7050.
141. Lukas, A. S.; Zhao, Y.; Miller, S. E.; Wasielewski, M. R. Biomimetic Electron Transfer Using Low Energy Excited States : A Green Perylene-Based Analogue of Chlorophyll A. *J. Phys. Chem. B*. **2002**, 106 (*6*).1299–1306.
142. Gosztola, D.; Niemczyk, M. P.; Svec, W.; Lukas, A. S.; Wasielewski, M. R. Excited Doublet States of Electrochemically Generated Aromatic Imide and Diimide Radical Anions. *J. Phys. Chem. A*. **2000**. 104 (*28*), 6545–6551.
143. Ford, W. E.; Hiratsuka, H.; Kamat, P. V. Photochemistry of 3,4,9,10-Perylenetetracarboxylic Dianhydride Dyes. 4. Spectroscopic and Redox Properties of Oxidized and Reduced Forms of the Bis(2,5-Di-Tert-Butylphenyl)Imide Derivative. *J. Phys. Chem.* **2002**, *93* (18), 6692–6696. DOI:10.1021/J100355A025.
144. Schlosser, F.; Moos, M.; Lambert, C.; Würthner, F. Redox-Switchable Intramolecular π − π-Stacking of Perylene Bisimide Dyes in a Cyclophane. *Adv. Mater.* **2013**, *25* (3), 410–414. DOI:10.1002/adma.201201266.
145. Zhao, Y. Z.; Li, K. X.; Ding, S. Y.; Zhu, M.; Ren, H. P.; Ma, Q.; Guo, Z.; Tian, S. P.; Zhang, H. Q.; Miao, Z. C. The Effect of Reduction Potential on the Generation of the Perylene Diimide Radical Anions. *Russ. J. Phys. Chem. A* **2018**, *92* (7), 1261–1265. DOI:10.1134/S003602441807035X.
146. Shirman, E.; Ustinov, A.; Ben-shitrit, N.; Weissman, H.; Iron, M. A.; Cohen, R.; Rybtchinski, B. Stable Aromatic Dianion in Water. *J. Phys. Chem. B Lett.* **2008**, *112* (30), 8855–8858. DOI:10.1021/jp8029743.
147. Seifert, S.; Schmidt, D.; Frank, W. An Ambient Stable Core-Substituted Perylene Bisimide Dianion: Isolation and Single Crystal Structure Analysis. *R. Soc. Chem.* **2015**, *6* (3), 1663–1667. DOI:10.1039/c4sc03671a.
148. Ma, W.; Qin, L.; Gao, Y.; Zhang, W.; Xie, Z.; Yang, B.; Liu, L.; Ma, Y. A Perylene Bisimide Network for High-Performance n-Type Electrochromism. *Chem. Commun.* **2016**, *52* (93), 13600–13603. DOI:10.1039/C6CC07962H.
149. Wurthner, F.; Sautter, A.; Schmid, D.; Weber, P. J. A. Fluorescent and Electroactive Cyclic Assemblies from Perylene Tetracarboxylic Acid Bisimide Ligands and Metal Phosphane Triflates. *Chem. - A Eur. J.* **2001**, *7* (4), 894–902.
150. You, C.-C.; Wurthner, F. Self-Assembly of Ferrocene-Functionalized Perylene Bisimide Bridging Ligands with Pt (II) Corner to Electrochemically Active Molecular Squares.

J. Am. Chem. Soc. **2003**, *125* (32), 9716–9725.
151. Büyükekşi, S. I.; Şengül, A.; Erdönmez, S.; Altındal, A.; Orman, E. B.; Özkaya, A. R. Spectroscopic, Electrochemical and Photovoltaic Properties of Pt (II) and Pd (II) Complexes of Chelating 1,10-Phenanthroline Appended Perylene Diimide. *Dalt. Trans.* **2018**, *47* (8), 2549–2560. DOI:10.1039/C7DT04713D.
152. Shin, I.-S.; Hirsch, T.; Ehrl, B.; Jang, D.-H.; Wolfbeis, O. S.; Hong, J.-I. Efficient Fluorescence "Turn-On" Sensing of Dissolved Oxygen by Electrochemical Switching. *Anal. Chem.* **2012**, *84* (21), 9163–9168.
153. Hu, G. Molecular Structure Induced Aggregation Effects on The Photophysical Properties of Perylene Diimide Based Multilayer Thin Films, Rensselaer Polytechnic Institute, Troy, NY, 2019.
154. Mutin, P. H.; Guerrero, G.; Vioux, A. Hybrid Materials from Organophosphorus Coupling Molecules. *J. Mater. Chem.* **2005**, *15* (35–36), 3761–3768. DOI:10.1039/b505422b.
155. Silverman, B. M.; Wieghaus, K. A.; Schwartz, J. Comparative Properties of Siloxane vs Phosphonate Monolayers on A Key Titanium Alloy. *Langmuir* **2005**, *21* (1), 225–228.
156. J., L. C.; Estroff, L. A.; Kriebel, J. K.; Nuzzo, R. G.; Whitesides, G. M. Self-Assembled Monolayers of Thiolates on Metals as a Form of Nanotechnology. *Chem. Rev.* **2005**, *105* (4), 1103–1169.
157. Folkers, J. P.; Laibinis, P. E.; Whitesides, G. M. Self-Assembled Monolayers of Alkanethiols on Gold: Comparisons of Monolayers Containing Mixtures of Short- and Long-Chain Constituents with CH3 and CH2OH Terminal Groups. *Langmuir* **1995**, *8* (5), 1330–1341.
158. Evans, S. D.; Urankar, E.; Ulman, A.; Ferris, N. Self-Assembled Monolayers of Alkanethiols Containing a Polar Aromatic Group: Effects of the Dipole Position on Molecular Packing, Orientation, and Surface Wetting Properties. *J. Am. Chem. Soc.* **1991**, *131* (11), 4121–4131.
159. Ulman, A. Formation and Structure of Self-Assembled Monolayers. *Chem. Rev.* **1996**, *96* (4), 1533−1554.
160. Kaim, W.; Fiedler, J. Spectroelectrochemistry: The Best of Two Worlds. *Chem. Soc. Rev.* **2009**, *38* (12), 3373–3382. DOI:10.1039/b504286k.
161. Lozeman, J. J. A.; Führer, P.; Olthuis, W.; Odijk, M. Spectroelectrochemistry, the Future of Visualizing Electrode Processes by Hyphenating Electrochemistry with Spectroscopic Techniques. *Analyst* **2020**, *145* (7), 2482–2509. DOI:10.1039/c9an02105a.
162. Girault, H. H. *Analytical and Physical Electrochemistry*, 1st ed.; CRC Press LLC, 2021.
163. Guy, O. J.; Walker, K. D. Graphene Functionalization for Biosensor Applications. In *Silicon Carbide Biotechnology*; Elsevier Inc; 2016. DOI:10.1016/B978-0-12-802993-0/00004-6.
164. Beaujuge, P. M.; Reynolds, J. R. Color Control in π-Conjugated Organic Polymers for Use in Electrochromic Devices. *Chem. Rev.* **2010**, *110* (1), 268–320. DOI:10.1021/cr900129a.
165. Seidel, J.; Luo, W.; Suresha, S. J.; Nguyen, P.; Lee, A. S.; Kim, S.; Yang, C.; Pennycook, S. J.; Pantelides, S. T.; Scott, J. F.; Ramesh, R. Prominent Electrochromism through Vacancy-Order Melting in a Complex Oxide. *Nat. Commun.* **2012**, *3* (799). DOI:10.1038/ncomms1799.
166. Oh, J. H.; Sun, Y.; Deppisch, M.; Krause, A.-M.; Radacki, K.; Braunschweig, H.;

Konemann, M.; Erk, P.; Bao, Z.; Wurthner, F. High-Performance Air-Stable n-Channel Organic Thin Film Transistors Based on Halogenated Perylene Bisimide Semiconductors. *J. Am. Chem. Soc.* **2009**, *131* (17), 6215–6228.

167. Li, G.; Zhao, Y.; Li, J.; Cao, J.; Zhu, J.; Sun, X.; Zhang, Q. Synthesis , Characterization , Physical Properties , and OLED Application of Single BN-Fused Perylene Diimide. *J. Org. Chem.* **2014**, *1*, 196–203. DOI:10.1021/jo502296z.
168. Hsiao, S.; Chen, Y. Electrochemical Synthesis of Stable Ambipolar Electrochromic Polyimide Film from a Bis (Triphenylamine) Perylene Diimide. *J. Electroanal. Chem.* **2017**, *799*, 417–423. DOI:10.1016/j.jelechem.2017.06.028.
169. Thelakkat, M. Star-Shaped , Dendrimeric and Polymeric Triarylamines as Photoconductors and Hole Transport Materials for Electro-Optical Applications. *Macromol. Mater. Eng.* **2002**, *287* (7), 442–461.
170. Chiang, C. C.; Chen, H.-C.; Lee, C.; Leung, M.; Lin, K.-R.; Hsieh, K.-H. Electrochemical Deposition of Bis(N,N′-Diphenylaminoaryl) Substituted Ferrocenes, and Their Application as a Hole-Injection Layer on Polymeric Light-Emitting Diodes. *Chem. Mater.* **2008**, *20* (2), 540–552.